Science Innovation
INTERNATIONAL SCIENTIFIC JOURNAL

ISSN: 2181-3337

SCIENCE & INNOVATION

INTERNATIONAL SCIENTIFIC JOURNAL

VOLUME 5 | ISSUE 9 | 2026
Series A: Technical Sciences

Science Innovation
INTERNATIONAL SCIENTIFIC JOURNAL

International Scientific Journal
SCIENCE AND INNOVATION
Series A
Volume 5 Issue 9
September 2026

Tashkent 2026

INTERNATIONAL SCIENTIFIC JOURNAL

SCIENCE & INNOVATION

Series A: Technical Sciences

VOLUME	ISSUE	PUBLICATION DATE	PLACE
5	9	31 SEPTEMBER 2026	TASHKENT

ISSUE IDENTIFICATION

RECOMMENDED ISSUE CITATION

Science and Innovation. Series A: Technical Sciences. Volume 5, Issue 9, September 2026. Tashkent: Science and Innovation LLC.
ISSN 2181-3337.

Individual article DOIs are registered through Crossref under prefix 10.67620.

JOURNAL INFORMATION

Volume / issue	Volume 5 · Issue 9	**Publication date**	31 September 2026
ISSN	2181-3337	**Publisher**	Science and Innovation LLC
Established	2022	**Publication language**	English
Frequency	Monthly	**Publication format**	Electronic · Open Access
Peer review	Double-blind peer review	**License**	Creative Commons Attribution 4.0
DOI registration	Crossref · Prefix 10.67620	**Official website**	https://scientists.uz

AIMS AND SCOPE

Series A publishes original research and reviews in engineering, technology, computer and information sciences, energy, architecture and construction, materials science, applied physics and mathematics, industrial systems, automation, environmental engineering, and related interdisciplinary innovations.

EDITORIAL AND PUBLICATION STANDARDS

PEER REVIEW

Editorial screening, integrity checks, independent double-blind review, and a documented editorial decision.

ETHICS & CORRECTIONS

Conflicts of interest, authorship, misconduct, corrections, retractions, complaints, and appeals are handled under published journal policies.

AI TRANSPARENCY

Authors must disclose substantive use of generative AI. AI tools cannot be credited as authors; responsibility remains with the human authors.

EDITORIAL OFFICE

Bakhtiyor Rustamov	CEO Science and innovation LLC	**Kozim Ergashov**	Academic Editor
Gulira'no Rakhmatullayeva	Responsible Secretary	**Feruzabonu Mannonova**	Language Editor
Feruza Ollomurodova	Manuscript Coordinator	**Jahongir Bekmuradov**	Language Editor
Farangiz Sagdullaeva	Technical Editor	**Anvar Ergashev**	Digital Media Designer
Dilnoza Narzullayeva	Editorial Manager	**Asila Khaydaralieva**	Academic Editor
Sevara O'rinboyeva	Editorial Manager	**Bakhrom Qurbonov**	Digital Media Designer

PUBLISHER AND CONTACT

Science and Innovation LLC · Mass Media License No. 1597 (27 April 2022) · Publishing License No. 455168 (21 November 2024)
150 Shota Rustaveli Street, Vega Business Center, 6th floor, Room 2, Tashkent 100121, Uzbekistan
info@scientists.uz · +998 90 125 96 54 · https://scientists.uz · https://science-innovation.org

© 2026 Authors. Published by Science and Innovation LLC under CC BY 4.0.

SCIENTIFIC EDITORIAL BOARD

Series A: Technical Sciences

EDITOR-IN-CHIEF: ABDURAKHMONOVA NILUFAR ZAYNOBIDDIN QIZI - DOCTOR OF PHILOLOGICAL SCIENCES, PROFESSOR

33 BOARD MEMBERS	**INTERNATIONAL REPRESENTATION** Uzbekistan · South Korea · Cameroon · Russian Federation · Kyrgyzstan · Malaysia · India · United States · Iran · France

Members are listed by academic standing and editorial responsibility. Current institutional profiles and contact details are maintained on the journal website.

Yusupbekov Nodirbek Rustambekovich DSc, Technical Sciences, Academician, Academy of Sciences of Uzbekistan, Honored Scientist *Tashkent State Technical University named after Islam Karimov · Uzbekistan*	**Mirsaidov Mirziyod Mirsaidovich** DSc, Technical Sciences, Professor, Academician, Academy of Sciences of Uzbekistan *TIIAME" National Research University · Uzbekistan*	**Allayev Qahramon Rahimovich** DSc, Technical Sciences, Professor, Academician, Academy of Sciences of Uzbekistan, Honored Youth Mentor of Uzbekistan *Academy of Sciences of the Republic of Uzbekistan · Uzbekistan*
Mirzaev Bahodir Suyunovich DSc, Technical Sciences, Professor, Rector *"Tashkent Institute of Irrigation and Agricultural Mechanization Engineers" National Research University · Uzbekistan*	**Gorbachyov Oleg Anatolyevich** DSc, Technical Sciences, Professor, Director of the Irkutsk Branch *Moscow State Technical University of Civil Aviation, Irkutsk Branch · Russia*	**Erokhin Vyacheslav Vladimirovich** DSc, Technical Sciences, Associate Professor, Dean of the Faculty of Aviation Systems and Complexes *Moscow State Technical University of Civil Aviation, Irkutsk Branch · Russia*
Yo'ldoshev Shukurullo Ubaydullayevich DSc, Technical Sciences, Professor, Academician, Academy of Sciences of Uzbekistan *TIIAME" National Research University · Uzbekistan*	**Bakiyev Masharif Ro'zmetovich** DSc, Technical Sciences, Professor *TIIAME" National Research University · Uzbekistan*	**Uon Don Yon** DSc, Technical Sciences, Professor *South Korea National Council for Future Education · South Korea*
Jimbo H. Claver PhD in Applied Mathematics and Statistics, Professor *Samarkand International University of Technology (SIUT) · Cameroon / Uzbekistan*	**Borisyuk Petr Viktorovich** DSc, Physical and Mathematical Sciences *National Research Nuclear University MEPhI (Russian Federation) · Russian Federation*	**Nishonov Mirkozimjon** Candidate of Technical Sciences, Professor *Fergana State University · Uzbekistan*
Sanayev Ermat Shermatovich PhD in Technical Sciences, Assoc. Professor *Tashkent Institute of Chemical Technology · Uzbekistan*	**Eshmuradov Dilshod Elmuradovich** Candidate of Technical Sciences, Assoc. Professor *Tashkent University of Information Technologies named after Muhammad al-Khwarizmi · Uzbekistan*	**Musayeva Shoira** Candidate of Economic Sciences, Professor *Samarkand Institute of Economics and Service · Uzbekistan*
Usmonov Ilkhom Achilovich Candidate of Technical Sciences, Professor *Samarkand State Institute of Architecture and Construction · Uzbekistan*	**Kamolov Ikhtiyor Ramazonovich** Candidate of Technical Sciences, Professor *Navoi State University · Uzbekistan*	**Abdazimov Anvar Daniyarovich** DSc, Technical Sciences, Professor *Tashkent State Technical University · Uzbekistan*
Akhatov Jasurjon Saidovich DSc, Technical Sciences, Professor *S.A. Azimov Institute of Physics and Technology of the Academy of Sciences of the Republic of Uzbekistan · Uzbekistan*	**Bazarov Dilshod Rayimovich** DSc, Technical Sciences, Professor *TIIAME" National Research University · Uzbekistan*	**Dodakho'jayev Abdulla Tursunovich** DSc, Technical Sciences, Professor *Tashkent State Technical University named after Islam Karimov · Uzbekistan*
Fayzullayev Normurot Ibodullayevich DSc, Technical Sciences, Professor *Samarkand State University · Uzbekistan*	**Ibadullayev Akhmadjon Sobirovich** DSc, Technical Sciences, Professor *Tashkent State Transport University · Uzbekistan*	**Attokurov Urmat Tologonovich** Candidate of Technical Sciences, Assoc. Professor, Professor *M.M. Adyshev Osh Technological University · Kyrgyzstan*
Che Zalina binti Zulkifli PhD in Electrical and Electronic Engineering, Professor *Universiti Pendidikan Sultan Idris (UPSI) · Malaysia*	**Sreekumara Ganapathy** PhD in Civil Engineering, Professor *Ajou University in Tashkent · India / Uzbekistan*	**Hwang Myeon-Eun** Professor of Electrical and Computer Engineering *Ajou University in Tashkent · South Korea / Uzbekistan*
Dr. Danish Ather PhD in Information Technology, Professor *Amity University · India*	**Seungjik Lee** PhD in Information Technology, Professor *Tashkent University of Information Technologies named after Muhammad al-Khwarizmi · South Korea / Uzbekistan*	**Olimov Bakhshillo Amrillayevich** Candidate of Physical and Mathematical Sciences, Assoc. Professor, Professor *Editor of the journal "Physics · Uzbekistan*
Bradley Fitzgerald Jacob Professor of Electrical and Computer Engineering *Samarkand International University of Technology (SIUT) · USA / Uzbekistan*	**Mohammad Reza Bahrami** PhD in Mechanical Engineering, Professor *Samarkand International University of Technology (SIUT) · Iran / Uzbekistan*	**Florence Dujjarik Sandrine** PhD, Professor *Samarkand International University of Technology (SIUT) · France / Uzbekistan*
Kamalova Dilnavoz Ikhtiyorovna DSc, Technical Sciences, Professor *Navoi State University · Uzbekistan*	**Yunusov Mirdjalil Yusupovich** DSc, Technical Sciences, Professor *Tashkent Institute of Chemical Technology · Uzbekistan*	**Safarov Toyir Tursunovich** DSc, Technical Sciences, Professor *Tashkent Institute of Chemical Technology · Uzbekistan*

ISSN: 2181-3337 | SCIENTISTS.UZ

ISSN: 2181-3337 | SCIENTISTS.UZ VOLUME 5 ISSUE 9 | SEPTEMBER 2026

INTEGRATION OF RENEWABLE ENERGY SOURCES INTO AGRICULTURE IN UZBEKISTAN

Begmatov Shavkat
Candidate of Technical Sciences, Professor, Tashkent Branch of the National Research University "Moscow Power Engineering Institute," Tashkent, Uzbekistan.
Email: shavkatbegmatov60@gmail.com

DOI: 10.67620/sai.59a0001

ABSTRACT
The electrification of agriculture is increasing demand for electricity. One way to meet this demand is through agrivoltaics (AV), an innovative technology in which photovoltaic panels are installed above or alongside crops so that electricity generation and agricultural production can occur on the same land. Because AV is only beginning to be introduced in Uzbekistan, this study examines its prospects for the country's agricultural sector. Uzbekistan's high solar radiation and high air temperatures in many regions create favorable conditions for AV, which can generate electricity while moderating crop and soil heat loads. This paper presents a methodology for estimating the technical, economic, and environmental indicators of an AV system per hectare of land and provides recommendations for implementing modern solar systems under regional climatic conditions. The results indicate that AV may help reduce farmers' dependence on external power grids and fossil fuels while improving the efficiency of land, water, and energy use in Uzbekistan.

ACCEPTED

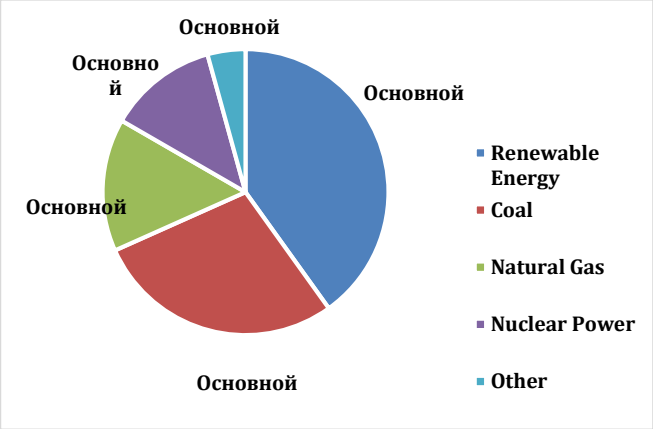
28.09.26

Keywords: *agrivoltaics, agriculture, electricity, photovoltaic panels, renewable energy, shading, soil moisture, solar energy, crop yield.*

CC BY

Introduction

Systematic electrification of agricultural production requires substantial electrical capacity. At present, centralized power-supply systems may not fully meet the growing electricity demand of the agricultural sector (Ministry of Energy of the Republic of Uzbekistan, 2024; World Bank, 2023; Allaev, 2021). Therefore, energy-efficient technologies for decentralized or autonomous electricity generation are increasingly important. One promising option is agrivoltaics (AV), which combines electricity generation with agricultural production on the same land (Kostyuchenko, 2016; Kostik & Bobyl, 2021; Fraunhofer Institute for Solar Energy Systems ISE, 2020; Lytle et al., 2021). AV systems generate electricity from solar energy while providing partial shading to crops. As a renewable-energy technology, AV can reduce dependence on external power grids and fossil fuels and, under suitable crop and climatic conditions, may improve crop performance. The technology is based on photovoltaic conversion of solar radiation into electrical energy while modifying the light and thermal environment beneath the panels (Fraunhofer Institute for Solar Energy Systems ISE, 2022; Liu et al., 2020; Bellos, 2025). Comparative data indicate that renewable energy sources (RES) accounted for about 40% of Germany's electricity generation by 2019 (Figure 1), whereas RES accounted for less than 1% of Uzbekistan's energy balance at the beginning of 2019 (Figure 2) (World Bank & Solargis, n.d.; Korzhovov, 2024).



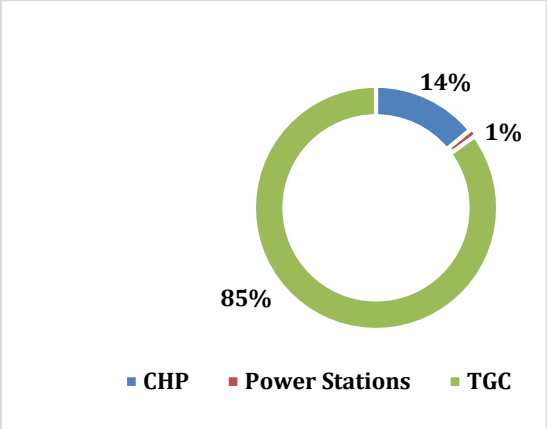


Figure 1. Renewable-energy generation in Germany by 2019. Figure 2. Renewable-energy generation in Uzbekistan by 2019.

Examples of AV implementation reported in different countries include the following:

• In India, AV systems have been deployed in vineyard areas, illustrating the potential for combining agricultural production with large-scale solar generation.

• In the United States, studies in arid environments such as Arizona have reported that partial shading from AV systems can reduce crop water use under certain conditions.

• Large AV power plants have also been developed in China, where the technology is presented as a means of reducing fossil-fuel use and associated emissions (Fraunhofer Institute for Solar Energy Systems ISE, 2022; Bellos, 2025; World Bank & Solargis, n.d.; Republic of Uzbekistan, 2024b).

Practical examples from companies and organizations active in the AV market include projects associated with policy and market initiatives described in Uzbekistan's electricity-supply planning documents (Republic of Uzbekistan, 2019; Cabinet of Ministers of the Republic of Uzbekistan, 2024):

• VALOREM Group is an independent operator in the field of "green" energy and AV projects in France, generating 12.4 GWh of electricity per year.

• Next2Sun has launched an AV solar park called "Agri" with an area of 11 hectares, which generates 4,800 MWh of electricity per year and supplies electricity to about 1,400 households.

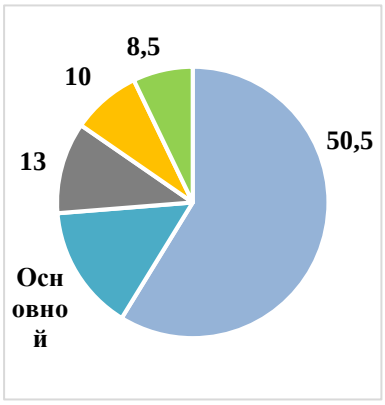
• Cero Generation Limited commissioned the 70 MW solar AV power plant "Pontinia," which supplies electricity to more than 47,000 homes.

The global AV market has expanded rapidly, although published market-size and growth estimates vary by source and methodology. Therefore, market forecasts should be interpreted cautiously and should be tied to a specific market-research source when used quantitatively (World Bank, 2023; Kostyuchenko, 2016; Kostik & Bobyl, 2021).

Data and Methods

In recent decades, shortages of water and land resources, soil degradation, rising energy consumption, and dependence on fossil fuels have created environmental and economic challenges for Uzbekistan (Ministry of Energy of the Republic of Uzbekistan, 2024; World Bank, 2023; Allaev, 2021; Republic of Uzbekistan, 2024a). To address these challenges, Uzbekistan adopted the Concept for Providing the Republic of Uzbekistan with Electricity for 2020–2030 and legislation on energy saving, rational energy use, and energy efficiency. According to the national electricity-supply concept, electricity generation from RES is planned to reach 18.5 billion kWh per year by 2030, including 10 billion kWh from solar power plants (Figure 3). Total installed generation capacity is projected to reach 29.3 GW by 2030, including 8 GW of RES capacity and 5 GW of solar capacity (Figure 4) (Republic of Uzbekistan, 2019; Cabinet of Ministers of the Republic of Uzbekistan, 2024; Begmatov & Aleksandrov, 2025).

ISSN: 2181-3337 | SCIENTISTS.UZ



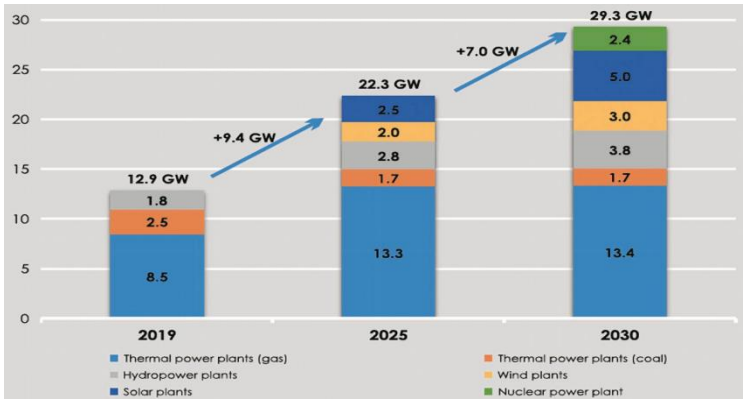


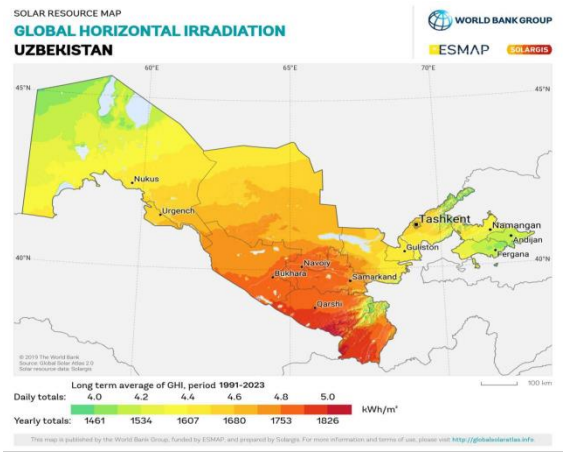
Figure 3. Electricity generation in Uzbekistan by 2030 (billion kWh/year).

Figure 4. Installed power-generation capacity in Uzbekistan by 2030 (GW).

The aim of this study is to examine Uzbekistan's solar-energy potential and the feasibility of implementing AV systems in agriculture. According to the solar-resource map of Uzbekistan, which summarizes long-term average daily and annual solar irradiation, daily global horizontal irradiation (GHI) in different regions ranges from approximately 4.0 to 5.0 kWh/m²/day, while annual GHI ranges from approximately 1,461 to 1,826 kWh/m²/year (Figure 5).

The air-temperature and precipitation data shown in Figure 6 indicate that Uzbekistan has approximately 270–300 sunny days per year and 2,800–3,000 sunshine hours. Monthly or seasonal temperature and precipitation values vary substantially by region; therefore, the plotted values should be interpreted in the context of the specific locations and periods represented in Figure 6.

According to the calculations used in this study, this solar potential could support electricity generation of more than 50 billion kWh per year, making solar energy an important area for renewable-energy development in Uzbekistan (Ministry of Energy of the Republic of Uzbekistan, 2024; World Bank, 2023; Allaev, 2021).



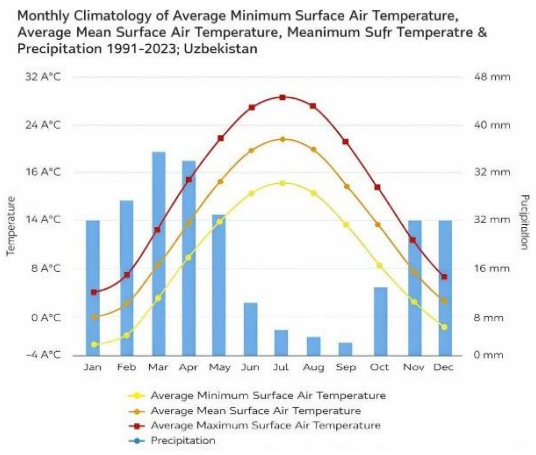


Figure 5. Solar-energy resources of Uzbekistan.

Figure 6. Air temperature and precipitation in Uzbekistan.

Results and Analysis

Across many regions of Uzbekistan, the period of strong solar irradiation and warm temperatures extends for much of the growing season. Based on the solar-resource map, potentially suitable regions for AV implementation include Khorezm, Bukhara, Kashkadarya, Surxondarya, Samarkand, Sirdarya, Fergana, Jizzakh, and the Republic of Karakalpakstan (Figure 7). Implementing AV systems in these regions could provide electricity for farms and, where grid rules permit, allow surplus electricity to be exported to the centralized grid. Panel shading may also reduce soil and crop overheating and help moderate the field microclimate.

Table 1

Modeled GHI Values for Selected Agricultural Crops in Uzbekistan

Crop type	Crop	Average GHI over 1 hour (W/m²)
Fiber crop	Cotton	327
Fiber crop	Wheat	304
Cereal crop	Barley	326
Cereal crop	Rice	176
Tuber crop	Potato	98
Tuber crop	Tomato	64

Note. GHI = global horizontal irradiance. Values are simulation-model results reported in the manuscript and should not be interpreted as universal crop thresholds.

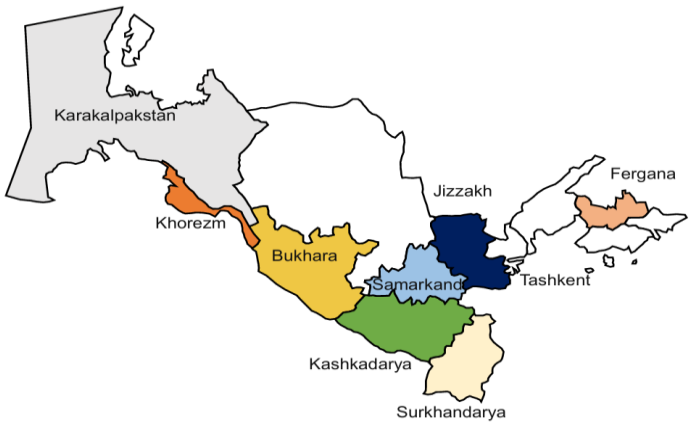


Figure 7. Promising regions of Uzbekistan for implementing AV systems in agriculture.

Table 1 presents the modeled average GHI values used in this study for selected agricultural crops. In AV design, the amount and timing of solar radiation reaching a crop under the panels should be matched to crop-specific light requirements. For example, the modeled value for cotton is 327 W/m². This value should be interpreted as a simulation input or target condition rather than as a universal agronomic threshold, because optimal irradiance depends on cultivar, growth stage, temperature, water availability, and other environmental factors (Cabinet of Ministers of the Republic of Uzbekistan, 2024; Begmatov & Aleksandrov, 2025).

Table 2

Reported Effects of Moderate Agrivoltaic Shading on Selected Crop and Soil Parameters

Parameter	Effect under moderate shading (20–30%)
Soil temperature	Decrease by approximately 3–6 °C
Water consumption	Decrease by approximately 15–20%

ISSN: 2181-3337 | SCIENTISTS.UZ

Photosynthesis	Increase by approximately 10–20%
Yield	Increase by approximately 10–30%, depending on crop type

Note. Reported ranges are indicative and may vary by crop, climate, soil, irrigation regime, and AV-system configuration.



Figure 8. Cotton damage associated with a change in the GHI level.

Crop yield can depend strongly on the degree and timing of shading of both the soil surface and the crop canopy. Table 2 summarizes the reported effects of moderate shading (20–30%) on selected parameters associated with crop performance. These ranges should be treated as indicative because the magnitude and direction of the response depend on crop species, climate, soil, irrigation, panel configuration, and management.

To assess the potential for AV implementation in the regions of Uzbekistan shown in Figure 7, a methodology is proposed for estimating electrical, economic, and environmental indicators for a 1-ha plot of land.

I. Calculation of Electrical Indicators

1. Calculation of the daily electrical energy output of a single translucent PV panel:

$$P = G \cdot A \cdot \eta \quad (1)$$

where G is the daily global horizontal irradiation (approximately 5 kWh/m²/day), A is the active surface area of the PV panel (approximately 1.6 m²), and η is the panel efficiency (approximately 20%). Substituting these parameters into Equation (1) gives the daily electrical energy output.

$$P = G \cdot A \cdot \eta = 5 \cdot 1{,}6 \cdot 0{,}20 = 1{,}6\ kW/day$$

For an annual GHI of 1,700 kWh/m²/year and a panel-covered area of 8,000 m², the gross annual electrical energy before system losses is calculated before applying the average loss coefficient (C_i = 0.8).

$$P = G \cdot A \cdot \eta = 1700 \cdot 8000 \cdot 0{,}20 = 2\,720000\ kW/year$$

2. Calculation of annual electricity generation:

$$E = G \cdot A \cdot \eta \cdot C_I \quad (2)$$

where G is the average annual global horizontal irradiation (1,700 kWh/m²/year), A is the area covered by PV panels (8,000 m²), η is the PV-panel efficiency (approximately 20%), and C_i is the average system-loss coefficient (0.8). The estimated annual electricity generation is therefore 2,176,000 kWh/year.

$$E = 1700 \cdot 8000 \cdot 0{,}20 \cdot 0{,}8 = 2\,176000\ kWh/year$$

3. Surface energy-balance equation:

ISSN: 2181-3337 | SCIENTISTS.UZ

$$Q_{abc} = G \cdot (1 - \alpha) \quad (3)$$

where Qabs is the daily solar energy absorbed by the soil (kWh/m²/day), G (GHI) is the daily global horizontal irradiation (approximately 6 kWh/m²/day), and α is the surface albedo (approximately 0.15–0.25 for soil). If α = 0.20, Equation (3) gives:

Qabs = 4.8 kWh/m²/day.

II. Calculation of Economic Indicators

4. Calculation of annual revenue from electricity generation:

$$M = p \cdot E, \quad (4)$$

where p is the average electricity price (approximately $0.05/kWh) and E is the annual electricity generation (2,176,000 kWh/year). The corresponding annual electricity revenue is approximately $108,800.

$$M = p \cdot E = 0{,}05 \cdot 2176000 = \$108800/year$$

5. Calculation of the investment payback period for an 8,000 m² panel-covered area:

$$T = \frac{C}{M} \quad (5)$$

where T is the payback period (years), C is the AV installation cost, M is annual income, and t is the assumed service life of the installation (15–20 years). The manuscript assumes an installation cost of approximately $800,000/MW and annual income of approximately $140,000/year, consisting of about $108,800/year from electricity and $31,200/year from agricultural production.

$$T = 800000 \,/\, 140000 \approx 6\ years$$

The stated payback period of approximately 4–5 years assumes government subsidies or other financial support. Because the subsidy rate and full capital-cost basis are not specified, this payback value should be treated as an estimate rather than as a directly reproducible result.

III. Calculation of Environmental Indicators

6. Estimated decrease in soil temperature under PV-panel shading:

$$\Delta T = T_{open} - T_{shadow} \approx 3 - 6℃ \quad (6)$$

The value of ΔT depends on panel density and height, soil color and moisture, wind and air circulation, and local climatic conditions.

7. Calculation of irrigation-water savings associated with moderate (20–30%) PV-panel shading:

$$\Delta W = E_0 \cdot A \cdot R \quad (7)$$

where ΔW is the volume of water saved (m³), e_0 is the baseline evaporation rate without shading, A_s is the shaded soil area (8,000 m²), and r is the relative reduction in evaporation (0.20). If e_0 = 2.5 mm/day, the dimensional conversion must use 0.0025 m/day.

$$\Delta W = 2{,}5 \cdot 8000 \cdot 0{,}2 = 4000 m^3/day$$

For a 120-day active irrigation period, an 8,000 m² shaded area, a baseline evaporation rate of 2.5 mm/day, and a 20% reduction in evaporation, the estimated water saving is approximately 480 m³. The previously stated value of 48,000 m³ is not consistent with these parameters.

$$\Delta W = 4000 \cdot 12 = 48000 m^3$$

8. Estimated reduction in the carbon footprint: approximately 500 t CO_2/year per hectare. This value requires an explicit baseline emission factor and displaced-electricity assumption to be independently reproducible.

The calculated results for one year are therefore as follows:

1. Energy performance: gross annual electrical energy before system losses — 2,720,000 kWh; estimated annual electricity generation after the assumed loss coefficient — 2,176,000 kWh.

2. Economic indicators: estimated annual electricity revenue — $108,800; stated AV-system payback period with subsidies — approximately 4–5 years.

ISSN: 2181-3337 | SCIENTISTS.UZ

3. Environmental indicators: estimated water savings under the stated evaporation assumptions — approximately 480 m³ over a 120-day active period; stated carbon-footprint reduction — approximately 500 t CO_2/year per hectare, subject to verification of the emission-factor assumptions.

These estimates indicate potential benefits of AV deployment in the regions identified in Figure 7, while also showing that the economic and environmental results depend on the assumptions used in the calculations.

Considering the electrical, economic, and environmental performance of AV systems per hectare and the climatic conditions of Uzbekistan's regions, the following AV technologies are recommended for further evaluation and implementation:

- • AV systems with automatic sun tracking can increase solar-energy capture relative to fixed-tilt systems under suitable conditions. Adjustable panel tilt can also be used to manage the degree and timing of crop shading across growth stages.
- • AV systems using semi-transparent or light-transmitting PV panels can partially transmit solar radiation, reduce direct heat load on the soil, and modify the distribution of light beneath the array. Such systems may be particularly relevant in regions where crop heat stress and water conservation are important design considerations.
- • A modular approach allows AV systems to be scaled from low-capacity mobile units (10–50 kW) for small farms, to medium-capacity systems (100–300 kW) for cooperatives, and to installations of 1 MW or more for large agribusinesses, depending on land-use conditions, grid access, and crop type.
- • Integrating AV systems with lithium-ion or sodium-ion battery storage can increase on-site use of solar electricity and improve supply reliability in remote areas. Exporting surplus electricity to centralized grids depends on applicable interconnection and market rules.
- • Remote monitoring can be used to track air and soil temperatures, irradiance, crop or soil moisture, and irrigation performance, while automated controls can adjust panel position where tracking systems are installed. Together, these functions can improve the management of water, energy, and crop microclimate.

Conclusion

1. The potential for introducing AV systems into Uzbekistan's agricultural sector is supported by the country's strong solar resource (Figure 5) and its temperature and precipitation patterns (Figure 6).

The manuscript reports that an AV system was introduced in vineyards in the Kuva District of the Fergana Region in 2025; a specific source should be cited for this project if the statement is retained.

2. AV-system performance depends on balancing electricity generation with the irradiance requirements of the crops grown beneath or between the panels.

The modeled GHI values in Table 1 can be used as design inputs, but they should not be presented as universal crop thresholds without additional agronomic validation.

3. Crop responses depend on the degree, timing, and spatial pattern of shading.

The ranges summarized in Table 2 suggest that moderate shading can influence soil temperature, water use, photosynthesis, and yield; however, the magnitude of these effects is crop- and site-specific.

4. The electrical, economic, and environmental calculations illustrate the potential value of AV systems in selected regions of Uzbekistan.

The results should be interpreted together with the assumptions stated in the methodology, particularly those concerning system losses, electricity price, subsidies, water savings, and carbon-emission factors.

5. According to the Concept for Providing the Republic of Uzbekistan with Electricity for 2020–2030,

ISSN: 2181-3337 | SCIENTISTS.UZ

solar generation capacity is planned to expand substantially by 2030, creating opportunities for wider deployment of AV systems in Uzbekistan's agricultural sector (Republic of Uzbekistan, 2019).

Overall, AV systems can combine clean-electricity generation with agricultural production on the same land. Their contribution to crop yield, water conservation, and emissions reduction depends on crop selection, system design, climatic conditions, and the technical and economic assumptions applied in each project.

REFERENCES

1. Allaev, K. R. (2021). *Modern energy and prospects for its development* (A. U. Salimova, Ed.). Fan va texnologiyalar nashriyot-manbaa uyi.
2. Begmatov, S. E. (2025). Agrovoltaics technology in agriculture in Uzbekistan. *Science and Innovation*, 4(10), 107–113. https://doi.org/10.5281/zenodo.17518558
3. Begmatov, S. E., & Aleksandrov, A. S. (2025). Prospects for the implementation of agrovoltaics in Uzbekistan. In *Development of modern electrical machines and drives for a green economy* (Proceedings of the Republican Scientific and Technical Conference, p. 184). Tashkent State Technical University.
4. Bellos, D. (2024, September 10). *Agrovoltaics: How it helps farmers and the climate*. Brite Solar. https://www.britesolar.com/aghrovoltaika-boithoun-ru
5. Bellos, D. (2025, February 5). *Agrovoltaics: Benefits and applications in agriculture—Dual use of land for food and energy*. Brite Solar. https://www.britesolar.com/aghrovoltaika-boithoun-ru
6. Cabinet of Ministers of the Republic of Uzbekistan. (2024). *On holding the "Year of Environmental Protection and Green Economy"*.
7. Fraunhofer Institute for Solar Energy Systems ISE. (2020). *Photovoltaics report*. https://www.ise.fraunhofer.de
8. Fraunhofer Institute for Solar Energy Systems ISE. (2022). *Agri-photovoltaics: Opportunities for agriculture and the energy transition*.
9. International Energy Agency Photovoltaic Power Systems Programme. (2023). *Trends in photovoltaic applications 2023*.
10. Ismoilov, Sh. Kh., & Tulyaganova, N. A. (2023). Agrovoltaics as an innovative direction for sustainable development of agriculture. *Bulletin of Agri Science of Uzbekistan*, 3(67), 57–64.
11. Korzhovov, A. (2024, March 27). Agrovoltaics: What benefits do solar farms bring? *Yuz.uz*. https://yuz.uz/ru/news/agrovoltaika
12. Kostik, N. R., & Bobyl, A. V. (2021). Potential of agrovoltaic systems in agriculture of the Russian Federation. *AgroEcoEngineering*, 2(107), 25–45.
13. Kostyuchenko, L. P. (2016). *Design of rural power supply systems*. KGAU.
14. Liu, H., Zhang, Y., Xu, Z., & Li, Z. (2020). Photovoltaic agriculture in China: A new development path of solar energy. *Renewable and Sustainable Energy Reviews*, 137, 110353.
15. Lytle, W., Meyer, T. K., Tanikella, N. G., Burnham, L., Engel, J., Schelly, C., & Pearce, J. M. (2021). Conceptual design and rationale for a new agrivoltaics concept: Pasture-raised rabbits and solar farming. *Journal of Cleaner Production*, 282, Article 124476. https://doi.org/10.1016/j.jclepro.2020.124476
16. Ministry of Energy of the Republic of Uzbekistan. (2024). *Report on the development of renewable energy sources in Uzbekistan*. https://energy.uz
17. Republic of Uzbekistan. (2019). *Concept for providing the Republic of Uzbekistan with electricity for 2020–2030* (Resolution of the President of the Republic of Uzbekistan No. PP-4422).
18. Republic of Uzbekistan. (2024a, August 7). *On electric power industry* (Law No. 939).

ISSN: 2181-3337 | SCIENTISTS.UZ VOLUME 5 ISSUE 9 | SEPTEMBER 2026

MULTI-CRITERIA MODEL FOR THE FORMATION OF AN URBAN BUS ROUTE NETWORK UNDER UNCERTAINTY

Urazxanova Elvira

Independent researcher, Department of Urban Infrastructure, Tashkent University of Architecture and Civil Engineering, 9 Yangi Shahar Street, Yunusabad, Tashkent 100194, Republic of Uzbekistan

DOI: 10.67620/sai.59a0002

ABSTRACT

Urban bus network design becomes especially challenging when passenger demand, running times, and operating conditions vary over time. This paper proposes a decision framework for comparing route alternatives under such uncertainty without collapsing the problem into a single performance indicator. The framework combines system analysis, dynamic programming, and multi-criteria optimization. Candidate routes are evaluated with respect to travel time, waiting time, headway, number of transfers, transport cost, service quality, and reliability. Operational inputs can be refreshed from GPS/GNSS records, passenger-flow observations, dispatching logs, and electronic fare-collection data, allowing the evaluation to respond to changing conditions. The procedure first generates feasible alternatives, then removes dominated solutions and retains a Pareto-efficient set for final managerial selection. The resulting structure links passenger demand, operating constraints, and service-quality considerations within a transparent workflow. For Nukus, the model offers a basis for periodically reassessing route choices as demand and operating conditions change. Rather than producing a single universal optimum, the approach identifies a defensible set of efficient alternatives from which planners can choose according to available fleet resources and policy priorities.

ACCEPTED

28.09.26

Keywords: *urban bus network; multi-criteria optimization; uncertainty; dynamic programming; Pareto efficiency; passenger demand; GPS/GNSS monitoring; public transport planning.*

CC BY

Introduction

Designing an urban bus network is a balancing problem rather than a shortest-path exercise. A route that performs well in terms of distance may be less attractive when waiting time, transfers, operating cost, reliability, or service coverage are considered simultaneously. For this reason, route planning should reflect both passenger experience and operator constraints instead of relying on a single indicator.

The planning task is also inherently dynamic. Demand is usually concentrated during morning and evening peaks, road congestion alters running times, and travel intensity may differ between weekdays and weekends. If these variations are represented by fixed average values, the resulting network may fail to match actual operating conditions. A more useful model therefore needs to accept updated demand and operational data and reassess route alternatives when the underlying conditions change.

Research conducted in Uzbekistan has highlighted several components relevant to this problem. Integrated evaluation has been used to describe the state of urban public transport infrastructure (Matrasulov & Yo‘ldoshev, 2025), while intelligent transport research has emphasized the role of real-time information, sensor-based observation, and data integration in management processes (Mirzabekov &

Kurbonova, 2025). Work on bus regularity has focused on schedule deviation and headway stability (Jurayev & Ikromov, 2025), and passenger-flow forecasting has been linked to the need to align service supply with demand (Abdullayev, 2025). Taken together, these studies show that route planning benefits from combining infrastructure, operational, and demand-related evidence.

The international literature provides a broader methodological foundation. Reviews of multi-criteria decision-making (MCDM) in transport show that such methods are well suited to problems in which objectives conflict and no single measure can represent overall performance (Keshavarz-Ghorabaee et al., 2022). Fuzzy AHP has been proposed for cases in which travel demand and user preferences cannot be expressed with complete certainty (Alkharabsheh et al., 2022). Integrated timetable and vehicle-scheduling studies further demonstrate the value of Pareto-efficient solutions when several objectives are optimized simultaneously (Liu et al., 2023). The increasing availability of heterogeneous transport data also creates opportunities to update planning decisions using multiple digital sources (Urbano et al., 2025), while fuzzy decision frameworks offer additional support when data are incomplete or imprecise (Kilic & Demirel, 2025).

Bus-network research also shows that demand varies across both space and time and that passengers, operators, and public authorities do not necessarily pursue identical objectives (Ibarra-Rojas et al., 2015). Earlier network-optimization studies similarly stressed the need to consider passenger costs and transfers when evaluating route structures (Mandl, 1980). Where explicit criterion weights are required, the Analytic Hierarchy Process remains a widely used tool for structuring relative priorities (Saaty, 1980).

Against this background, the purpose of this study is to formulate a route-evaluation model that can compare feasible bus-network alternatives under uncertain operating conditions and identify a set of Pareto-efficient options rather than forcing a single predetermined optimum.

Materials and Methods. A staged analytical procedure was constructed using system analysis, object-oriented representation of transport elements, decision theory, dynamic programming, and multi-criteria optimization. The procedure follows the analytical logic developed in the underlying dissertation but is organized here as a reproducible sequence that can be applied to another route set or urban area.

The input layer contains demand and operating variables that can be updated over time: passenger-flow estimates, observed running time, service headway, the number of buses assigned to a route, GPS/GNSS traces, dispatching observations, and electronic fare-collection records. Combining these sources improves temporal and spatial coverage compared with using a single source (Urbano et al., 2025).

The network is treated as a sequence of discrete states. A state may correspond to a route segment, stop, or transfer node, and each state has a limited set of feasible transitions. Candidate trajectories are generated from the origin to the destination through these admissible transitions. Dynamic programming is then used to track how a local choice at one stage affects the feasible and efficient choices available at subsequent stages.

Each candidate route is evaluated using a common set of service and operational criteria. In the present formulation, the core criteria are travel time, waiting time, headway, number of transfers, transport cost, service quality, and reliability. This set is not intended to be rigid: additional criteria, such as safety or environmental performance, can be introduced when the planning task requires them. The selected structure is consistent with the broader MCDM approach used in transport analysis (Ibarra-Rojas et al., 2015; Keshavarz-Ghorabaee et al., 2022).

ISSN: 2181-3337 | SCIENTISTS.UZ

Table 1

Evaluation Criteria Used to Compare Bus-Route Alternatives

No.	Criterion	Operational meaning
1	Travel time	Total time required to move from origin to destination
2	Waiting time	Time spent waiting for the next available vehicle
3	Headway (service interval)	Elapsed time between two consecutive buses
4	Number of transfers	Number of vehicle changes required during a trip
5	Transport cost	Passenger- and operator-related costs associated with the alternative
6	Service quality	Regularity, convenience, and practical accessibility of the service
7	Reliability	Degree of agreement between planned and observed operation

The model is implemented through the following six-stage procedure:

Stage 1. Build the input dataset. Assemble passenger demand, observed running time, headway, fleet allocation, and route information in a common database.

Stage 2. Generate feasible alternatives. Construct all admissible route options between the selected origin and destination, subject to network constraints.

Stage 3. Calculate criterion values. Estimate travel time, waiting time, number of transfers, transport cost, service quality, and reliability for every alternative.

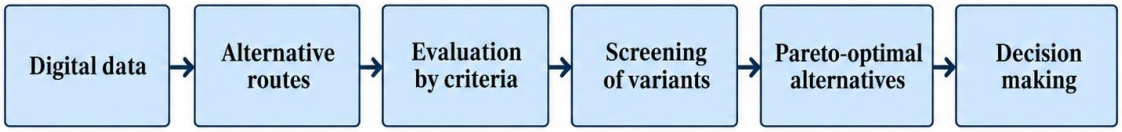
Stage 4. Remove dominated solutions. Exclude any alternative for which another feasible option is no worse on all principal criteria and better on at least one.

Stage 5. Form the Pareto-efficient set. Retain alternatives for which improving one criterion requires deterioration in at least one other criterion.

Stage 6. Make the planning choice. Compare the remaining efficient alternatives with passenger demand, available fleet capacity, and current management priorities.

Figure 1

Workflow for Screening and Selecting Route Alternatives



Uncertainty is handled by treating key inputs as updatable observations rather than permanent constants. When passenger demand, running time, or traffic conditions change, the affected criterion values are recomputed and the efficient set is regenerated. If expert-defined criterion weights are introduced, sensitivity analysis should be used to test how strongly the final ranking depends on those weights. Where uncertainty is substantial, fuzzy techniques can be added to the evaluation process (Alkharabsheh et al., 2022; Kilic & Demirel, 2025; Saaty, 1980).

Results. The analysis produced a route-selection framework in which operational feasibility and passenger-oriented criteria are assessed together. Its principal contribution is not a single numerical optimum but a structured way to narrow a potentially large set of route alternatives to a smaller group of efficient and practically defensible options.

First, the bus network was formalized as a sequence of connected decision states. This representation makes it possible to evaluate route trajectories incrementally: a choice made at one stage changes the set of feasible outcomes at later stages. Dynamic programming is therefore used as the mechanism for linking local route decisions to the final network outcome.

Second, the evaluation is extensible. The seven core criteria shown in Table 1 form the basic comparison set, but the model does not impose a fixed upper limit on the number of criteria. Safety,

ISSN: 2181-3337 | SCIENTISTS.UZ

environmental performance, accessibility, or other locally relevant indicators can be added without changing the overall decision logic. This flexibility is consistent with MCDM applications in urban transport (Keshavarz-Ghorabaee et al., 2022).

Third, the model uses dominance screening before a final choice is made. Alternatives that are clearly inferior are removed, while nondominated alternatives are retained as the Pareto-efficient set. This avoids the misleading assumption that one route must be best in every dimension. Similar use of Pareto-based reasoning has been reported in integrated public transport scheduling and vehicle allocation (Liu et al., 2023).

Fourth, the model can be recalculated when new digital observations become available. The joint use of passenger-flow information, GPS/GNSS data, fare transactions, and dispatching records allows route performance to be revisited as conditions evolve rather than only during periodic manual reviews (Urbano et al., 2025).

Table 2

Decision Rule Used to Retain or Reject Route Alternatives

Alternative status	**Interpretation**	**Action**
Nondominated	Performs at least as well as competing alternatives across the principal criteria and better on at least one criterion relative to a dominated alternative	Retain
Dominated	Another feasible alternative is no worse on all principal criteria and better on at least one criterion	Remove
Pareto-efficient	No criterion can be improved without worsening at least one other criterion	Carry forward to final selection

Operational feasibility is checked after the efficient alternatives have been identified. The underlying dissertation relates the required fleet size to round-trip time and the planned service interval. If round-trip time is denoted by $T_{o\beta}$ and the service interval by I, the number of buses required on the route is:

$$A_m = T_{o\beta} / I$$

When the required number of buses, A_m, is known, the corresponding service interval is obtained from:

$$I = T_{o\beta} / A_m$$

These relationships provide a simple resource check: an alternative may be efficient in the multi-criteria sense but still be impractical if the available fleet cannot sustain the required headway. The complete decision chain can therefore be summarized as passenger demand → route alternatives → operational checks → multi-criteria screening → Pareto-efficient set → final planning decision.

Discussion and Conclusion. The findings reinforce the view that urban bus-route design should not be reduced to shortest distance or minimum travel time. A route may shorten in-vehicle time while creating additional transfers or higher operating costs; another may take slightly longer but provide more stable service or better coverage. The proposed framework makes these trade-offs explicit and allows passenger and operator interests to be considered within the same analytical process (Ibarra-Rojas et al., 2015; Keshavarz-Ghorabaee et al., 2022; Mandl, 1980).

A practical advantage of Pareto screening is that it preserves choice. Instead of presenting decision-makers with one mathematically imposed solution, the method returns a small set of efficient alternatives. The final selection can then reflect current fleet availability, demand patterns, policy priorities, or service-quality targets. This is consistent with recent work in which timetable and vehicle-allocation decisions are optimized jointly rather than independently (Liu et al., 2023).

The framework also has a clear limitation: the quality of the output depends on the quality of the inputs. Sparse GPS/GNSS records, incomplete fare data, or inconsistent dispatching logs can distort one

ISSN: 2181-3337 | SCIENTISTS.UZ

or more criterion values. For operational use, the data streams should therefore be integrated and quality-checked (Mirzabekov & Kurbonova, 2025; Urbano et al., 2025). If criterion weights are used, their influence should be tested through sensitivity analysis; fuzzy methods can be added where uncertainty cannot be adequately represented by precise values (Alkharabsheh et al., 2022; Kilic & Demirel, 2025).

In summary, the proposed model provides a more realistic basis for route-network planning under uncertainty than a single-criterion approach. Dynamic programming connects decisions across successive network states, while Pareto analysis separates clearly inferior alternatives from those that represent meaningful trade-offs. For Nukus, periodic updates using passenger-flow, GPS/GNSS, fare-collection, and dispatching data would allow the route network to be reassessed as travel demand and operating conditions change.

REFERENCES

1. Abdullayev, B. I. (2025). Yo‘lovchilar oqimini bashorat qilish modelini ishlab chiqish. *Journal of Transport, 2*(2), 46–48. https://doi.org/10.56143/2181-2438-2025-2-46-48
2. Alkharabsheh, A., Moslem, S., & Duleba, S. (2022). Analyzing public travel demand by a fuzzy analytic hierarchy process model for supporting transport planning. *Transport, 37*(2), 110–120. https://doi.org/10.3846/transport.2022.15881
3. Ibarra-Rojas, O. J., Delgado, F., Giesen, R., & Muñoz, J. C. (2015). Planning, operation, and control of bus transport systems: A literature review. *Transportation Research Part B: Methodological, 77*, 38–75. https://doi.org/10.1016/j.trb.2015.03.002
4. Jurayev, M. N., & Ikromov, M. D. (2025). Shahar yo‘nalishli avtobuslar harakat muntazamligini ta’minlash modellarini takomillashtirish. *Journal of Transport, 2*(2), 27–30. https://doi.org/10.56143/2181-2438-2025-2-27-30
5. Keshavarz-Ghorabaee, M., Amiri, M., Zavadskas, E. K., Turskis, Z., & Antuchevičienė, J. (2022). MCDM approaches for evaluating urban and public transportation systems: A short review of recent studies. *Transport, 37*(6), 411–425. https://doi.org/10.3846/transport.2022.18376
6. Kilic, M., & Demirel, T. (2025). Fuzzy decision systems for sustainable public transport: A literature review. *International Journal of Computational Intelligence Systems, 18*, Article 164. https://doi.org/10.1007/s44196-025-00904-6
7. Liu, T., Ji, W., Gkiotsalitis, K., & Cats, O. (2023). Optimizing public transport transfers by integrating timetable coordination and vehicle scheduling. *Computers & Industrial Engineering, 184*, Article 109577. https://doi.org/10.1016/j.cie.2023.109577
8. Mandl, C. E. (1980). Evaluation and optimization of urban public transportation networks. *European Journal of Operational Research, 5*(6), 396–404. https://doi.org/10.1016/0377-2217(80)90126-5
9. Matrasulov, K. Sh., & Yo‘ldoshev, D. F. (2025). Shahar jamoat transporti infratuzilmasining holatini ekspert baholari asosida integral baholash. *Journal of Transport, 2*(3), 19–22. https://doi.org/10.56143/2181-2438-2025-3-19-22
10. Mirzabekov, M. S., & Kurbonova, B. K. (2025). Intelektual transport tizimlari: Aqlli shaharlar uchun integratsiyalashgan yondoshuv. *Journal of Transport, 2*(3), 67–71. https://doi.org/10.56143/2181-2438-2025-3-67-71
11. Saaty, T. L. (1980). *The analytic hierarchy process: Planning, priority setting, resource allocation*. McGraw-Hill.
12. Urbano, V. M., Arena, M., & Azzone, G. (2025). Big data for decision-making in public transport management: A comparison of different data sources. *Research in Transportation Business & Management, 59*, Article 101298. https://doi.org/10.1016/j.rtbm.2025.101298

ISSN: 2181-3337 | SCIENTISTS.UZ

ISSN: 2181-3337 | SCIENTISTS.UZ VOLUME 5 ISSUE 9 | SEPTEMBER 2026

URBAN BUS ROUTE OPTIMIZATION USING DYNAMIC PROGRAMMING AND PARETO-EFFICIENT SELECTION

Jumabaev Dauletbay[1], **Urazxanova Elvira**[2]

Associate Professor, Department of Urban Planning and Economics, Karakalpak State University, PhD. Ch. Abdirov Street 1, Nukus 230100, Karakalpakstan, Republic of Uzbekistan[1]

Independent Researcher, Department of Urban Infrastructure, Tashkent University of Architecture and Civil Engineering. Yangi Shahar Street 9, Yunusabad, Tashkent 100194, Republic of Uzbekistan[2]

DOI: 10.67620/sai.59a0003

ABSTRACT

The paper proposes a route-optimization framework that combines dynamic programming with Pareto-efficient selection for urban bus networks operating under variable demand and service conditions. The network is represented as a finite set of states connected by admissible transitions, so route formation can be treated as a sequence of linked decisions rather than as a single shortest-path calculation. The procedure evaluates candidate trajectories using passenger- and operator-oriented measures, including travel time, waiting time, transfer convenience, service reliability, and resource requirements. At each stage, Bellman recursion is used to propagate cumulative performance through the state graph, while a nondominance test removes alternatives that are inferior across the selected criteria. The retained labels form an efficient set that can be updated when GPS/GNSS observations, fare transactions, dispatching records, or passenger-flow estimates change. The analytical results show that the combined procedure preserves meaningful trade-offs between user convenience and operating efficiency and avoids premature reduction of the problem to a single weighted objective. For Nukus, the framework can serve as a decision-support mechanism for adaptive route planning and subsequent coordination with timetables, fleet allocation, and digital transport services.

ACCEPTED

28.09.26

Keywords: *dynamic programming; Pareto efficiency; bus route optimization; state-space model; passenger demand; GPS/GNSS data; public transport planning.*

CC BY

Introduction

Designing an urban bus network requires decisions about route alignment, demand coverage, service frequency, transfers, fleet use, and reliability. These objectives are interdependent and often conflict. A path that reduces passenger travel time may require additional buses, whereas broader territorial coverage can increase running time and make transfers more complex. Consequently, route design is better viewed as a multistage decision problem than as a conventional shortest-path task.

Daily operating conditions add another layer of uncertainty. Passenger volumes change by time of day, congestion alters link travel times, dwell times are not constant, and service intervals may become unstable. Because the attractiveness of a route can change during the operating day, a static representation based on fixed costs is insufficient. A more suitable approach is to describe the network through states and feasible transitions whose performance values can be refreshed as new operational information becomes available.

Recent studies in Uzbekistan point in the same direction. Matrasulov and Yo‘ldoshev (2025) used several expert indicators to assess the condition of urban public transport infrastructure. Mirzabekov and Kurbonova (2025) highlighted the role of real-time monitoring, sensor information, and integrated data in intelligent transport management. Jurayev and Ikromov (2025) examined mathematical approaches to improving bus regularity, while Abdullayev (2025) considered passenger-flow forecasting as an input for service and fleet planning. Together, these works show that route decisions increasingly depend on combined demand, operational, and digital information.

International research provides complementary evidence. Dou and Li (2023) addressed timetable coordination when travel time is uncertain. Risso et al. (2023) formulated a bi-objective problem that balances transfer synchronization against operating cost. Lin et al. (2023) used Pareto analysis to represent heterogeneous comfort preferences, while Hu et al. (2023) jointly optimized timetables and vehicle schedules with attention to fleet cost and passenger waiting. Real-time Pareto-based control has also been investigated by Pasquale et al. (2024). More recent studies have linked adaptive dispatching to changing demand (Barrera Hernandez et al., 2025) and used Pareto frontiers to balance passenger comfort with operator efficiency (Cheng & He, 2024). Reviews of bus-system planning further confirm the importance of treating network design, operation, and control as connected decisions (Ibarra-Rojas et al., 2015), while Mandl’s (1980) classical work provides an early foundation for network-level route optimization. The aim of this study is therefore to formulate a reproducible route-search procedure in which dynamic programming structures the sequential decision process and Pareto screening preserves efficient alternatives under conflicting criteria.

Materials and methods. The route network is modeled as a directed state graph. A state can represent a stop, transfer point, route segment, or another information condition relevant to passenger or vehicle movement. From each state, only admissible decisions are allowed, and every decision leads to a successor state. A complete route is therefore constructed as a chain of local transitions from an origin to a terminal state. The method is designed so that another researcher can reproduce the procedure once the state set, feasible transitions, criterion values, and operating constraints are specified.

Table 1

Core Elements of the Dynamic Route-Optimization Model

Model component	Symbol	Role in computation
Admissible states	D	Set of movement and information states included in the route-search space.
Terminal set	F	Destination states at which the recursive search stops.
Available actions	$V(x)$	Feasible decisions that may be taken from state x.
State transition	$f(x, v)$	Rule that maps a current state and selected action to a successor state.
Local measure	$s(x, v)$	Criterion value assigned to a permitted transition.
Route trajectory	T	Ordered state sequence linking an origin with a terminal state.
Local aggregate	D_i	Optional weighted indicator constructed from criterion-specific partial evaluations.

The state-space description used in the model is:

$$\Omega = \{D, F, V(x), f(x,v), s(x,v)\} \quad (1)$$

A feasible route is described by a finite sequence $T = \{x^0, x^1, x^2, \ldots, x^n\}$. Consecutive states must satisfy the admissible transition rule:

$$x^t = f(x^{t-1}, v^t), \quad v^t \in V(x^{t-1}), \quad t = 1,2,\ldots,n \quad (2)$$

For a single cost criterion, the continuation value is computed recursively according to Bellman’s principle of optimality (Bellman, 1957):

ISSN: 2181-3337 | SCIENTISTS.UZ

$$S(x) = \min_{v \in V(x)} \{ s(x,v) + S(f(x,v)) \}, \quad x \in D \setminus F \quad (3)$$

Terminal states are assigned a continuation value of zero. The calculation then proceeds backward from the destination toward the origin. For each predecessor state, the admissible successor producing the best continuation value is stored. Because downstream values are reused, common route segments do not need to be evaluated repeatedly. This makes the procedure suitable for layered networks in which several alternatives merge at the same transfer point.

To represent several objectives at the local level, a weighted performance indicator may be written as:

$$D_i = \sum_{j=1}^{m} b_{ij} c_j \rightarrow max, \qquad \sum_{j=1}^{m} c_j = 1 \quad (4)$$

In this expression, b_{ij} denotes the performance of a partial decision under criterion j, and c_j is the relative importance assigned to that criterion. For Equation (4), larger b_{ij} values represent better performance, so the weighted indicator is maximized. The scalar form is useful when stable preferences are available, but it may conceal meaningful trade-offs. For that reason, the main selection procedure works with criterion vectors and applies Pareto dominance before the next dynamic-programming stage.

The dominance rule is implemented in minimization form. Candidate a dominates candidate b when a is no worse than b on every criterion and is strictly better on at least one criterion. Criteria expressed as benefits, such as reliability or service quality, are transformed so that all components have the same optimization direction. Only nondominated labels are retained at each state. The computational sequence is repeated whenever updated demand, travel-time, or fleet information changes the local criterion values.

Table 2

Reproducible Optimization Procedure

Step	Required information	Computation	Result
1. Build the network	Stops, transfer points, route segments	Encode admissible states and directed transitions.	State graph.
2. Attach data	Demand, travel times, monitoring and dispatch records	Assign criterion values to each permitted transition.	Transition-value database.
3. Initialize destination	Terminal state set F	Set the continuation value at terminal states to zero.	Boundary values.
4. Run backward recursion	Predecessor states and admissible actions	Evaluate predecessor labels using Bellman recursion.	Candidate cumulative labels.
5. Screen by dominance	Criterion vectors for candidate labels	Discard labels dominated on the selected criteria.	Efficient labels at each state.
6. Check operations	Fleet availability and service constraints	Remove routes that violate practical operating limits.	Feasible efficient routes.
7. Refresh when data change	Updated GPS/GNSS, fare, demand, or dispatch information	Revise affected transition values and repeat Steps 4–6.	Updated efficient set.

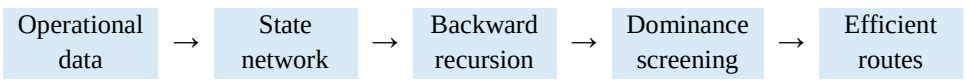


Figure 1. Computational sequence used to generate efficient route alternatives.

The procedure is intended for repeated updating rather than one-time optimization. When observed demand, route travel time, transfer conditions, or fleet availability change, only the affected local values are revised before backward recursion and nondominance screening are performed again. GPS/GNSS

ISSN: 2181-3337 | SCIENTISTS.UZ

observations, fare transactions, dispatching logs, and passenger-flow estimates can therefore be incorporated without rebuilding the entire state structure.

Results. The resulting architecture divides route optimization into two coordinated operations. Dynamic programming propagates the consequences of local choices through the network, whereas Pareto screening limits the candidate set to criterion combinations that remain efficient. This structure prevents the solution from being driven by a single arbitrary cost measure and avoids carrying every possible trajectory to the final stage.

The first result is a finite-state representation of the route-stop-transfer system. The graph contains an origin, intermediate decision states, transfer states, and a destination connected by admissible arcs. Each arc stores local performance information, and a complete route is assembled from the corresponding transition sequence. This formulation makes route formation directly compatible with algorithmic search and allows the same network structure to support different demand scenarios.

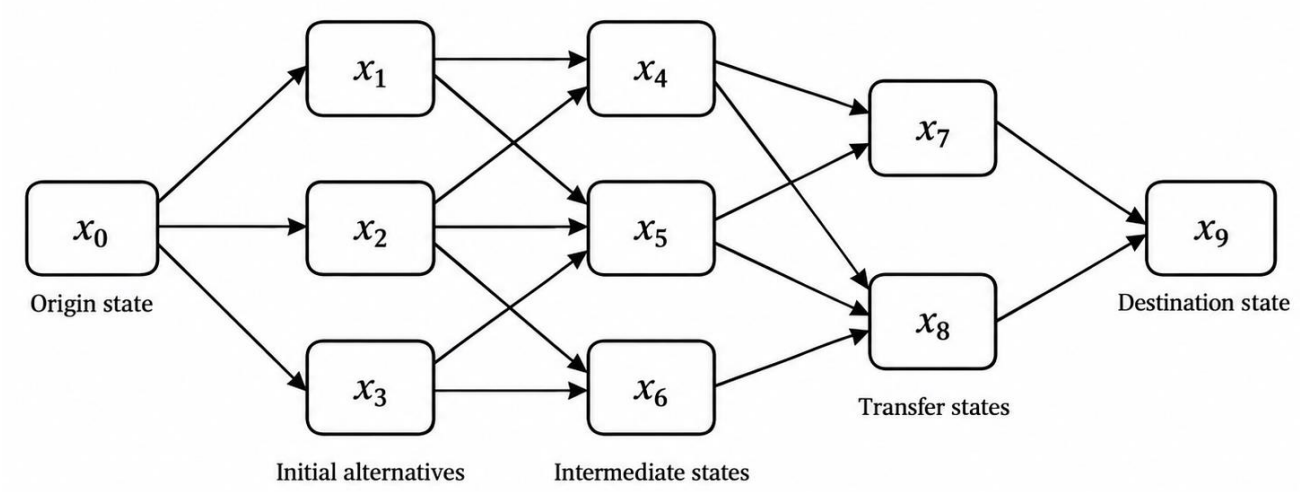


Figure 2. Layered state-transition representation used in the route-search procedure.

The second result is a recursive search mechanism. Any feasible trajectory can be separated into an immediate decision and a remaining subproblem. Equation (3) exploits this structure by storing the continuation value associated with each downstream state. When several alternatives share the same transfer point, their common continuation is evaluated once and reused, thereby reducing unnecessary repetition in the search process.

The third result is the preservation of trade-offs among several objectives. Equation (4) can be applied when criterion weights are known and sufficiently stable. If the weights are uncertain, or if the decision-maker needs to see competing performance profiles explicitly, Pareto screening is preferable. It can retain, for example, a route with a slightly higher operating requirement when that route substantially reduces passenger time or transfers, while also retaining a lower-cost alternative when its service penalty remains acceptable.

The fourth result is the ability to react to changing operating conditions without altering the model structure. A congestion event may increase the value attached to one transition, a new passenger-flow pattern may change the importance of a transfer point, and fare or dispatching records may reveal a shift in demand. After such changes, only the affected labels are recalculated and the efficient set is refreshed. This feature is particularly relevant to an urban system such as Nukus, where both demand and service conditions vary over time.

ISSN: 2181-3337 | SCIENTISTS.UZ

Table 3

Main Analytical Outcomes and Their Operational Meaning

Analytical outcome	Methodological role	Use in planning
Finite-state representation	Encodes route construction as admissible state transitions.	Enables algorithmic comparison of route alternatives.
Recursive evaluation	Reuses downstream continuation values across multistage decisions.	Reduces repeated evaluation of shared route segments.
Pareto screening	Keeps only alternatives that remain nondominated across conflicting criteria.	Makes user–operator trade-offs explicit.
Data-driven refresh	Allows transition values to change when new observations arrive.	Supports re-optimization after demand or traffic changes.
Digital-system compatibility	Connects route, stop, transfer, vehicle, passenger, and payment information.	Facilitates linkage with monitoring, dispatching, and mobility services.

The study is analytical and does not report a universal percentage improvement across all routes. Its contribution is the decision structure itself: a finite-state formulation, explicit transition rules, backward recursion, multicriteria local evaluation, and state-by-state elimination of dominated alternatives. Quantitative gains should be reported only after the procedure has been tested using measured route data against a defined baseline and evaluation protocol.

Discussion and conclusion. The proposed method is consistent with current public-transport optimization research, but it organizes the decision problem at the route-state level. Dou and Li (2023) concentrate on timetable coordination under uncertain travel time, whereas the present framework starts from the sequence of route states through which a passenger or vehicle can move. Risso et al. (2023) obtain Pareto-efficient timetable solutions, and Lin et al. (2023) preserve trade-offs among passenger, operator, and policy objectives. These studies support the decision to keep efficient alternatives visible instead of compressing all objectives into a single fixed score too early.

Hu et al. (2023) show that timetable and vehicle scheduling can be coordinated while balancing fleet cost and passenger waiting. Pasquale et al. (2024) demonstrate that Pareto-efficient decisions can also be selected in real time. In the framework proposed here, the same idea is embedded within a dynamic route search: nondominated alternatives are preserved at intermediate states, not only after all complete routes have been enumerated. This gives the decision-maker access to efficient trade-offs throughout the search process.

The adaptive character of the method is also consistent with the work of Barrera Hernandez et al. (2025), who combine demand forecasting with responsive dispatching. Cheng and He (2024) similarly show the value of balancing passenger comfort with operating efficiency. In the present model, new digital observations revise the local state values, after which only the affected recursive calculations need to be updated. This creates a practical link between strategic route design and continuously changing operational information.

Several limitations remain. The quality of the efficient set depends on the accuracy of passenger-flow, travel-time, and fleet data. The number of nondominated labels may also grow rapidly when many criteria are introduced, so large networks may require additional pruning or preference rules. Finally, a weighted scalar indicator is sensitive to expert judgment when the coefficients are not well established. For planning applications, Pareto representation is therefore useful because the final preference is postponed until clearly inefficient alternatives have been removed.

For Nukus, the method is best interpreted as a decision-support layer within a wider digital transport environment. Information about routes, stops, transfer points, buses, passengers, payments, and monitoring

ISSN: 2181-3337 | SCIENTISTS.UZ

can be connected to the same state representation. The efficient route set can then be tested against fleet availability, timetable constraints, service coverage, and transfer coordination before implementation.

Conclusion

Dynamic programming and Pareto-efficient selection complement one another in urban bus route optimization. The recursive component divides a complex network problem into manageable subproblems, while the dominance test preserves only alternatives that remain competitive across the selected criteria. The combined procedure makes passenger-operator trade-offs transparent, avoids dependence on a single objective, and can be updated as digital observations change. Its main scientific value lies in connecting state-based route representation, recursive optimization, and multicriteria efficient selection within one reproducible framework. Applied to Nukus, it offers a methodological basis for adaptive route planning and for subsequent coordination with timetables, dispatching, electronic fare collection, and other digital transport services.

REFERENCES

1. Abdullayev, B. I. (2025). Yo‘lovchilar oqimini bashorat qilish modelini ishlab chiqish. *Journal of Transport*, *2*(2), 46–48. https://doi.org/10.56143/2181-2438-2025-2-46-48
2. Barrera Hernandez, J. E., Tarazona Torres, L. E., Tabares, A., & Álvarez-Martínez, D. (2025). Optimization of bus dispatching in public transportation through a heuristic approach based on passenger demand forecasting. *Smart Cities*, *8*(3), Article 87. https://doi.org/10.3390/smartcities8030087
3. Bellman, R. (1957). *Dynamic programming*. Princeton University Press.
4. Cheng, G., & He, Y. (2024). Enhancing passenger comfort and operator efficiency through multi-objective bus timetable optimization. *Electronic Research Archive*, *32*(1), 565–583. https://doi.org/10.3934/era.2024028
5. Dou, X., & Li, T. (2023). Multi-objective bus timetable coordination considering travel time uncertainty. *Processes*, *11*(2), Article 574. https://doi.org/10.3390/pr11020574
6. Hu, B., Fu, Y., & Feng, S. (2023). Integrated optimization of multi-vehicle-type timetabling and scheduling to accommodate periodic passenger flow. *Computer-Aided Civil and Infrastructure Engineering*, *38*(14), 1973–1997. https://doi.org/10.1111/mice.12979
7. Ibarra-Rojas, O. J., Delgado, F., Giesen, R., & Muñoz, J. C. (2015). Planning, operation, and control of bus transport systems: A literature review. *Transportation Research Part B: Methodological*, *77*, 38–75. https://doi.org/10.1016/j.trb.2015.03.002
8. Jurayev, M. N., & Ikromov, M. D. (2025). Shahar yo‘nalishli avtobuslar harakat muntazamligini ta’minlash modellarini takomillashtirish. *Journal of Transport*, *2*(2), 27–30. https://doi.org/10.56143/2181-2438-2025-2-27-30
9. Lin, P., He, C., Zhong, L., Pei, M., Zhou, C., & Liu, Y. (2023). Bus timetable optimization model in response to the diverse and uncertain requirements of passengers for travel comfort. *Electronic Research Archive*, *31*(4), 2315–2336. https://doi.org/10.3934/era.2023118
10. Mandl, C. E. (1980). Evaluation and optimization of urban public transportation networks. *European Journal of Operational Research*, *5*(6), 396–404. https://doi.org/10.1016/0377-2217(80)90126-5
11. Matrasulov, K. Sh., & Yo‘ldoshev, D. F. (2025). Shahar jamoat transporti infratuzilmasining holatini ekspert baholari asosida integral baholash. *Journal of Transport*, *2*(3), 19–22. https://doi.org/10.56143/2181-2438-2025-3-19-22
12. Mirzabekov, M. S., & Kurbonova, B. K. (2025). Intelektual transport tizimlari: Aqlli shaharlar uchun integratsiyalashgan yondoshuv. *Journal of Transport*, *2*(3), 67–71. https://doi.org/10.56143/2181-2438-2025-3-67-71

ISSN: 2181-3337 | SCIENTISTS.UZ

13. Pasquale, C., Sacone, S., Siri, S., & Ferrara, A. (2024). Pareto-optimal event-based scheme for station and inter-station control of electric and automated buses. *IEEE Open Journal of Control Systems*, *3*, 445–460. https://doi.org/10.1109/OJCSYS.2024.3456633
14. Risso, C., Nesmachnow, S., & Rossit, D. (2023). Smart public transport: A bi-objective model for maximizing synchronizations and minimizing costs in bus timetables. *Applied Sciences*, *13*(24), Article 13032. https://doi.org/10.3390/app132413032

ISSN: 2181-3337 | SCIENTISTS.UZ VOLUME 5 ISSUE 9 | SEPTEMBER 2026

HYDRAULIC CALCULATION PROCEDURE FOR FLOW EXPANSION CONSTRICTED BY A SPUR DIKE

Bakiev Masharif[1], Kuryozov Otaboy[2], Yakubov Kuvonchbek[3], Khasanov Khojiakbar[4], Khalimbetov Azat[5], Ganjayev Mukhammad[6]

Professor, Head of the Department of Hydrotechnical Structures and Engineering Constructions, Tashkent Institute of Irrigation and Agricultural Mechanization Engineers – National Research University (TIIAME-NRU)[1]

Independent Researcher, Department of Hydrotechnical Structures and Engineering Constructions, TIIAME-NRU[2]

PhD, Associate Professor, Department of Hydrotechnical Structures and Engineering Constructions, TIIAME-NRU[3]

Assistant and Independent Researcher, Department of Hydrotechnical Structures and Engineering Constructions, TIIAME-NRU[4]

PhD, Associate Professor, Department of Hydrotechnical Structures and Engineering Constructions, TIIAME-NRU[5]

Independent Researcher, Department of Hydrotechnical Structures and Engineering Constructions, TIIAME-NRU[6]

DOI: 10.67620/sai.59a0004

ABSTRACT

This paper investigates the hydraulics of a flow constricted by a bank-protection structure - a spur dike, locally referred to as a "banket" - installed at a 90° angle to the flow axis in an open rectangular flume. Using data from a laboratory flume test (Test No. 9: flume width B = 0.40 m, spur length lδ = 0.08 m, constriction ratio nδ = 0.2, bed slope ib = 0.0001), a step-by-step calculation procedure is developed for the flow in the expansion zone downstream of the spur dike. The procedure determines the Chezy and Pavlovsky resistance coefficients separately for the bed and walls of the flume, calculates the expansion angle and reach length by successive approximation, derives the mean and depth-averaged velocities of the transit flow from a universal dimensionless relationship, and estimates the reverse velocities within the recirculation zone. The calculated and experimental results agree well: the length of the recirculation zone differs by less than 3% (Lcalc = 93 cm versus Lexp = 95 cm), and the calculated and experimental velocity profiles closely match. The proposed procedure is applicable to the design and hydraulic analysis of bank-protection and river-training structures on rivers and canals.

ACCEPTED

28.09.26

Keywords: *spur dike, recirculation zone, resistance coefficient, flow expansion angle, expansion reach length, mean velocity, depth-averaged velocity, universal relationship, reverse velocity, experimental-to-calculated comparison.*

CC BY

Introduction

The hydraulics of flow constricted by bank-protection and river-training structures - spur dikes and groynes - remains a pressing problem in river hydraulics and hydraulic engineering. Such structures are widely used to regulate river channels, protect banks, and shape the navigation channel. Their interaction with the flow produces a complex spatial structure: a constriction zone directly at the structure, an

expansion zone downstream, and a recirculation zone with reverse velocities. Describing these zones accurately calls for both reliable hydraulic resistance coefficients and robust procedures for calculating the averaged flow characteristics.

The Chezy coefficient C and the related Manning coefficient n are central to the calculation of uniform and non-uniform flow in open channels. Achour (2015) and Loukam et al. (2018, 2020) derived explicit relationships for C in circular, egg-shaped and horseshoe-shaped cross-sections, showing that resistance depends strongly on cross-section geometry, hydraulic radius and roughness. For rectangular channels, Achour and Bedjaoui (2006) confirmed the need for iterative procedures when determining normal depth from the Chezy formula, while Shirley and Lopes (1991) proposed an algorithm for computing normal depth in complex cross-sections that converges reliably under any boundary conditions. These methods are now widely applied in the design of irrigation and drainage canals.

Joldassov et al. (2023) systematized approaches to determining roughness coefficients along the wetted perimeter of a channel cross-section, examining both analytical and empirical methods for treating bed and wall resistance separately. Tymiński et al. (2022) verified resistance-calculation methods for floodplains with flexible vegetation - relevant when assessing bank resistance near the base of a spur dike. Giustolisi (2004) applied genetic programming to derive parsimonious relationships for C in corrugated channels, opening the way to automated calibration of design formulas, and Ferguson et al. (2019) showed that in channels with multiple roughness scales, a spatially-averaged roughness length approximates the shear-stress distribution more accurately than a fixed value of n or C.

Flow through channel contractions and expansions has been studied both experimentally and numerically. Babarutsi et al. (1996) examined recirculating flow at a sudden expansion in a shallow channel and identified a “frictional” regime in which the length of the recirculation zone is governed by the friction length scale. Singh et al. (2023) showed experimentally that as the degree of contraction increases, secondary currents intensify and a surface velocity dip appears - an effect that significantly shapes the velocity profile in the expansion zone behind a spur dike. Mulahasan et al. (2021) found numerically that velocities near a lateral obstruction can double, together with increased bed loading in the separation zone, while Franques (1971) proposed a finite-element model for two-dimensional steady flow through contractions in natural channels that accounts for energy losses.

Vertical flow contractions likewise produce a stagnation and recirculation zone downstream, as demonstrated in both experimental and numerical studies (Majid & Tripathi, 2022, 2023). Proust et al. (2006) showed that under abrupt floodplain contraction, one-dimensional models can produce significant errors in discharge distribution by neglecting lateral momentum exchange. Namihira et al. (2004) used LES and VOF simulations to analyze flow through successive transverse constrictions, confirming that eddy-resolving methods remain applicable to complex obstacle configurations.

The vortex zones that form at flow confluences and bifurcations resemble those observed at spur dikes. Weber et al. (2001) experimentally studied recirculation zones in rectangular 90° open-channel junctions, and Gao et al. (2025) verified the LES method for reproducing vortex structures in T-shaped bifurcations. Chiu et al. (1976) applied deterministic-stochastic methods to three-dimensional modeling of hydraulic processes in open channels, highlighting how sensitive such calculations are to the choice of resistance coefficient.

Despite this progress in understanding the hydraulics of constricted and expanding flows, a comprehensive calculation procedure - one that combines Pavlovsky resistance coefficients, the distribution of mean and depth-averaged transit-flow velocities, and reverse velocities in the recirculation zone under spur-dike constriction - has yet to be fully developed. The present work addresses this gap: it proposes a step-by-step hydraulic calculation procedure for flow expansion constricted by a spur dike, based on laboratory-flume data and universal dimensionless relationships.

ISSN: 2181-3337 | SCIENTISTS.UZ

Materials and Methods

Experimental Setup

The experiments were carried out in a laboratory hydraulic flume of rectangular cross-section. The flume bed consisted of planed boards coated with enamel (roughness coefficient n = 0.009), and the walls were finished with smooth cement plaster (roughness coefficient n = 0.011); the bed slope was set at ib = 0.0001.

The bank-protection structure (spur dike) was modeled as a rigid element installed perpendicular ($\alpha\delta = 90°$) to the flow axis at one of the flume walls. The constriction ratio $n\delta = l\delta \cdot \sin\alpha\delta / B$ was varied by changing the length of the protruding part of the spur dike, $l\delta$, while the flume width B was held constant. The calculation below corresponds to the conditions of Test No. 9 ($B = 0.40$ m; $l\delta = 0.08$ m; $n\delta = 0.2$).

Discharge was held constant throughout the tests and monitored with a metering device ($Q = 0.005$ m^3/s in the test presented below). Free-surface levels and flow velocities were measured at control cross-sections along the constriction zone, the expansion zone and the recirculation zone, and at several verticals within each section; the vertical profiles were then depth-averaged to build the experimental velocity profiles used for comparison with the calculated ones.

Results and Discussion

The calculation below is carried out for the conditions of Test No. 9: flume width B = 0.40 m, spur length $l\delta = 0.08$ m, installation angle $\alpha\delta = 90°$, constriction ratio $n\delta = l\delta \cdot \sin\alpha\delta / B = 0.08 \cdot 1 / 0.40 = 0.2$, and bed slope ib = 0.0001. The flume bed is made of planed boards coated with enamel, roughness coefficient n = 0.009; the walls are covered with smooth cement plaster, roughness coefficient n = 0.011.

ISSN: 2181-3337 | SCIENTISTS.UZ

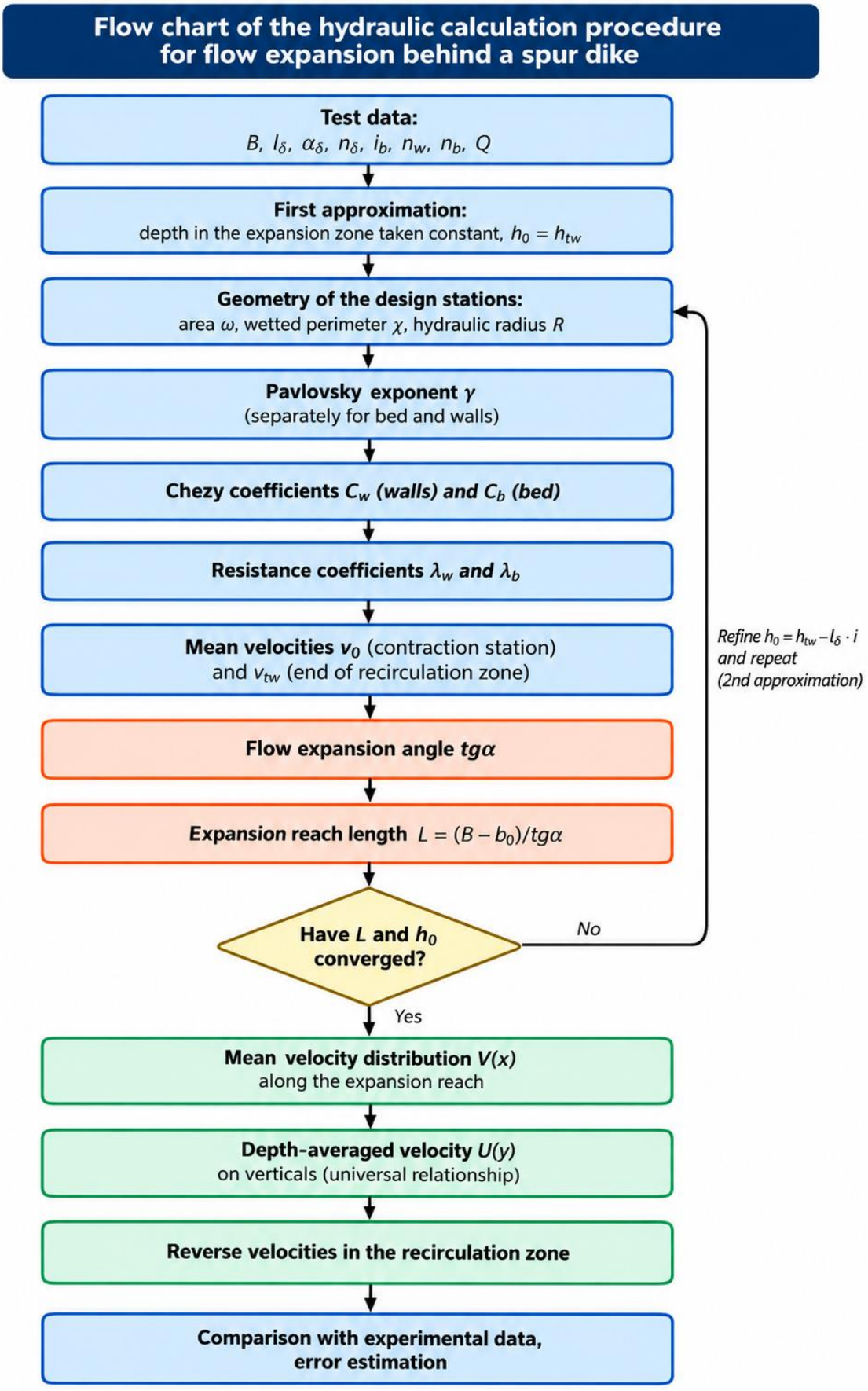


Fig. 1. Flow chart of the hydraulic calculation procedure for expansion behind the spur dike

Calculation algorithm

1st approximation ($h_0 = h_{tw}$)

ISSN: 2181-3337 | SCIENTISTS.UZ

The expansion angle and reach length are calculated by the method of successive approximations. In the first approximation, the water depth is taken constant along the entire length of the expansion reach. In the second approximation, the depth at the contraction station is refined to account for the bed slope.

Step 1. Determine the design depth. The water depth over the expansion reach is taken uniform along the entire length:

$h_0 = h_{tw} = 0.066$ m

Step 2. Determine the geometric characteristics of the design stations. The flow area ω, wetted perimeter χ and hydraulic radius R are determined for the contraction station and for the end of the recirculation zone:

$\omega_0 = b_0 \cdot h_0 = 0.32 \times 0.066 = 0.0211$ m²; $\chi_0 = b_0 + 2h_0 = 0.32 + 2 \times 0.066 = 0.452$ m

$\omega_{tw} = B \cdot h_{tw} = 0.40 \times 0.066 = 0.0264$ m²; $\chi_{tw} = B + 2h_{tw} = 0.40 + 2 \times 0.066 = 0.532$ m

$R_0 = \omega_0/\chi_0 = 0.0211/0.452 = 0.0467$ m; $R_{tw} = \omega_{tw}/\chi_{tw} = 0.0264/0.532 = 0.0496$ m

Step 3. Determine the mean hydraulic radius. The mean hydraulic radius over the expansion reach is:

$R = 0.5(R_0 + R_{tw}) = 0.5(0.0467 + 0.0496) = 0.0471$ m

Step 4. Determine the Pavlovsky exponents (for R<1.0 m: y=1.5√n; for R>1.0 m: y=1.3√n). Since R<1.0 m:

$y_w = 1.5\sqrt{n_w} = 1.5\sqrt{0.011} = 1.5 \times 0.1049 = 0.157$ (for the walls)

$y_b = 1.5\sqrt{n_b} = 1.5\sqrt{0.009} = 1.5 \times 0.0949 = 0.142$ (for the bed)

Step 5. Determine the Chezy coefficients:

$C_w = (1/n_w) \cdot R^{yw} = 111.1 \times 0.0471^{0.157} = 111.1 \times 0.619 = 68.77$ $m^{0.5}/s$

$C_b = (1/n_b) \cdot R^{yb} = 90.9 \times 0.0471^{0.142} = 90.9 \times 0.646 = 58.72$ $m^{0.5}/s$

Step 6. Determine the resistance coefficients:

$\lambda_w = g/C_w^2 = 9.81/68.77^2 = 9.81/4729.3 = 0.00207$

$\lambda_b = g/C_b^2 = 9.81/58.72^2 = 9.81/3448.0 = 0.00285$

Step 7. Determine the mean velocities:

$v_0 = Q/\omega_0 = 0.005/0.0211 = 0.237$ m/s (at the contraction station)

$v_{tw} = Q/\omega_{tw} = 0.005/0.0264 = 0.189$ m/s (at the end of the recirculation zone)

Step 8. Determine the flow expansion angle. The tangent of the expansion angle is given by:

$tg\alpha = [(\lambda_w/2.15) \cdot \ln(B/b_0) + (\lambda_b/2.15) \cdot (B - b_0) + (0.09522/2.15) \cdot \ln(B/b_0)] / [\ln(v_0/v_{tw}) - 0.5 \cdot \ln(B/b_0)]$

Numerator terms: 1) $(0.00207/2.15) \cdot \ln 1.25 = 0.00096 \times 0.223 = 0.00022$

2) $(0.00285/2.15) \cdot 0.08 = 0.000106$

3) $(0.09522/2.15) \cdot \ln 1.25 = 0.0443 \times 0.223 = 0.0099$

sum of the numerator = 0.00022+0.000106+0.0099 = 0.0102

denominator = $\ln(0.237/0.189) - 0.5 \cdot \ln 1.25 = 0.226 - 0.112 = 0.114$

$tg\alpha = 0.0102/0.114 = 0.09$

Step 9. Determine the expansion reach length:

$L = (B - b_0)/tg\alpha = (0.40 - 0.32)/0.09 = 0.89$ m

2nd approximation (refining the depth to account for the bed slope)

Step 10. Refine the depth at the contraction station, accounting for the drop of the bed over the length L:

$h_0 = h_{tw} - i_b \cdot L = 0.066 - 0.0001 \times 0.89 = 0.0659$ m

Step 11. Re-determine the geometry and the mean hydraulic radius (with the refined h_0):

$\omega_0 = 0.32 \times 0.0659 = 0.021$ m²; $\chi_0 = 0.32 + 2 \times 0.0659 = 0.4518$ m

$R_0 = 0.021/0.4518 = 0.04648$ m; $R_{tw} = 0.0264/0.4132 = 0.0639$ m

$R = 0.5(0.04648 + 0.0639) = 0.05519$ m

Step 12. The Pavlovsky exponent is unchanged (R<1.0 m): y_w=0.157; y_b=0.142

Step 13. Re-determine the Chezy coefficients:

$C_w = 111.1 \times 0.05519^{0.157} = 111.1 \times 0.635 = 70.5$ $m^{0.5}/s$

ISSN: 2181-3337 | SCIENTISTS.UZ

$C_b = 90.9 \times 0.05519^{0.142} = 90.9 \times 0.66 = 60.24\ m^{0.5}/s$

Step 14. Re-determine the resistance coefficients:

$\lambda_w = 9.81/70.5^2 = 9.81/4970.3 = 0.00197$

$\lambda_b = 9.81/60.24^2 = 9.81/3628.9 = 0.00270$

Step 15. Re-determine the mean velocities:

$v_0 = 0.005/0.021 = 0.238$ m/s; $v_{tw} = 0.005/0.0264 = 0.189$ m/s

Step 16. Re-determine the flow expansion angle:

Numerator terms: 1) $(0.00197/2.15)\cdot\ln 1.25 = 0.000916 \times 0.223 = 0.000204$

2) $(0.00270/2.15)\cdot 0.08 = 0.00010$

3) $(0.09522/2.15)\cdot\ln 1.25 = 0.0099$

sum of the numerator = 0.000204+0.00010+0.0099 = 0.010204

denominator = $\ln(0.238/0.189) - 0.5\cdot\ln 1.25 = 0.230 - 0.112 = 0.118$

$tg\alpha = 0.010204/0.118 = 0.086$

Step 17. Determine the refined expansion reach length:

$L = (0.40 - 0.32)/0.086 = 0.93$ m

The experimental length of the recirculation zone is L_{exp}=0.95 m, and the calculated length is L_{calc}=0.93 m. Thus the discrepancy between the calculated and experimental lengths of the recirculation zone does not exceed 3 %, which indicates satisfactory agreement of the results.

Velocity distribution along the expansion reach

Step 18. Determine the velocity at the tailwater section. The mean flow velocity at the tailwater section is:

$V_{tw} = Q/(B\cdot h_{tw}) = 0.005/(0.40 \times 0.066) = 0.189$ m/s

Step 19. Determine the exponents in the velocity distribution formula. The first exponent is:

$0.5 + \lambda_w/(2.15\cdot tg\alpha) + 0.09522/(2.15\cdot tg\alpha) = 0.5+0.0107+0.515 \approx 1.0$

$\lambda_b/(2.15\cdot h)\cdot(L-x) = 0.00270/(2.15 \times 6.59)\cdot(93-x) = 0.00019(93-x)$

Step 20. Determine the distribution of mean velocities along the expansion reach ($Y_{tr}=b_0+tg\alpha\cdot x$ - the transit-flow width at station x):

$V = V_{tw}\cdot(B/Y_{tr})^{1.0}\cdot e^{0.00019(93-x)}$

The results of the calculation at the control stations are given in Table 1 and Fig. 2.

Table 1. Distribution of mean flow velocity along the expansion reach

x, cm	Ytr, cm	B/Ytr	L-x, cm	0.00019(L-x)	e^0.00019(L-x)	V, cm/s
10	32.86	1.217	83	0.0158	1.0159	23.37
30	34.58	1.157	63	0.012	1.0121	22.13
50	36.3	1.102	43	0.008	1.008	20.99
70	38.02	1.052	23	0.0044	1.0044	19.97
90	39.74	1.007	3	0.00057	1.00057	19.043

ISSN: 2181-3337 | SCIENTISTS.UZ

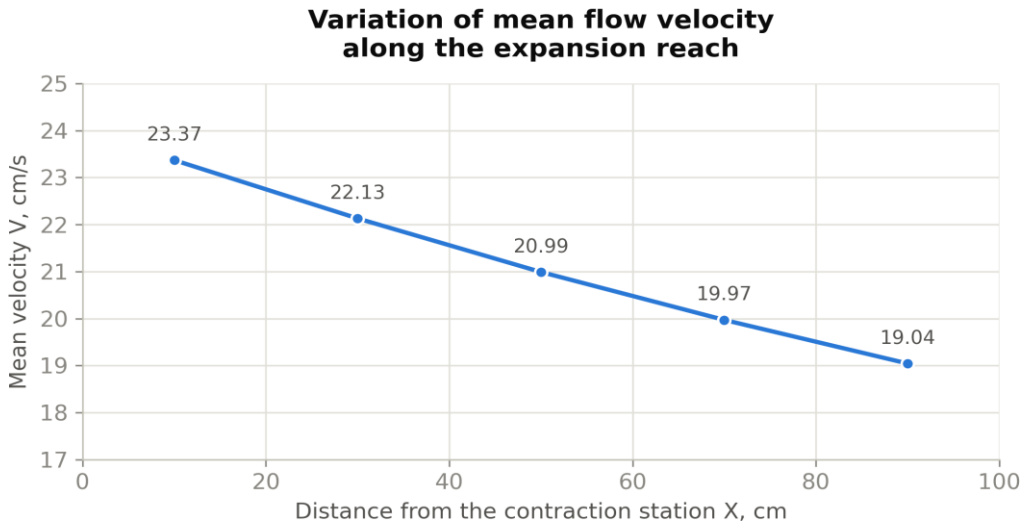


Fig. 2. Variation of the mean flow velocity V along the length of the expansion reach (Table 1)

Step 21. Determine the depth-averaged velocities on verticals, from the universal dimensionless relationship:

$$U/V = 0.99 + 1.88(y/Y_{tr}) - 2.87(y/Y_{tr})^2$$

The calculation is performed for stations x_1=30 cm (Y_{tr}=34.58 cm, V=22.13 cm/s), x_2=50 cm (Y_{tr}=36.3 cm, V=20.99 cm/s) and x_3=70 cm (Y_{tr}=38.02 cm, V=19.97 cm/s) - Tables 2–4, Fig. 3.

Table 2. Calculation of depth-averaged velocities at station x1 = 30 cm

Parameter	5 cm	10 cm	15 cm	20 cm	25 cm	30 cm
y/Ytr	0.145	0.289	0.434	0.578	0.723	0.868
(y/Ytr)^2	0.0209	0.0836	0.188	0.335	0.523	0.753
U/V	1.203	1.293	1.266	1.117	0.848	0.462
U, cm/s	26.62	28.6	28.02	24.72	18.76	10.22

Table 3. Calculation of depth-averaged velocities at station x2 = 50 cm

Parameter	5 cm	10 cm	15 cm	20 cm	25 cm	30 cm
y/Ytr	0.138	0.276	0.413	0.551	0.689	0.826
(y/Ytr)^2	0.02	0.0759	0.171	0.304	0.474	0.683
U/V	1.195	1.291	1.275	1.153	0.925	0.583
U, cm/s	25.07	27.098	26.76	24.2	19.42	12.25

Table 4. Calculation of depth-averaged velocities at station x3 = 70 cm

Parameter	5 cm	10 cm	15 cm	20 cm	25 cm	30 cm
y/Ytr	0.132	0.263	0.395	0.578	0.658	0.868
(y/Ytr)^2	0.0174	0.0692	0.156	0.334	0.432	0.753
U/V	1.188	1.285	1.285	1.185	0.987	0.687
U, cm/s	23.73	25.66	25.66	23.66	19.71	13.71

ISSN: 2181-3337 | SCIENTISTS.UZ

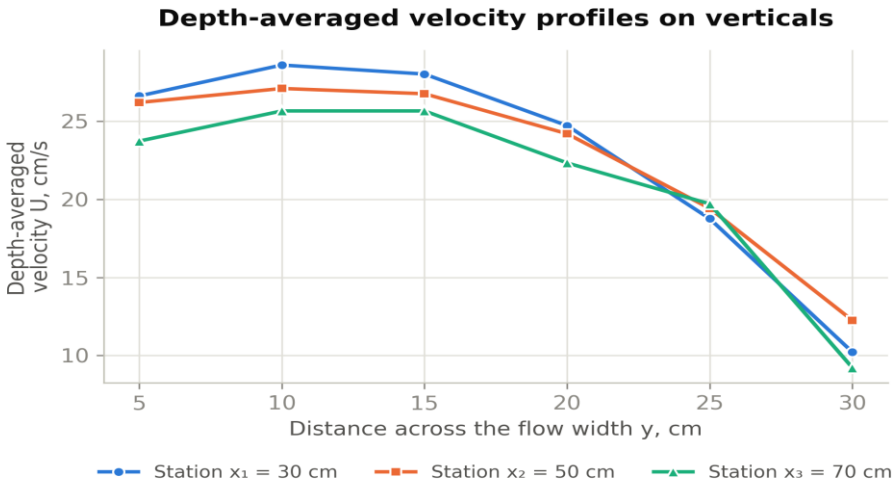


Fig. 3. Depth-averaged velocity profiles on verticals at stations x1, x2 and x3 (Tables 2–4)

Step 22. Compare the calculated and experimental data.

The length of the expansion zone from experiment is L_{exp}=95 cm, and the calculated length is L_{calc}=93 cm - the agreement is satisfactory; the calculated and experimental velocity profiles practically coincide.

Reverse velocities in the recirculation zone

Step 23. Determine the relative quantities:

$\bar{B} = B/b_0 = 0.40/0.32 = 1.25$

$\bar{h}_x = h_x/h_{tw}$, where $h_x = h_{tw} - i_b \cdot x$ (x measured from the tailwater station)

$\bar{V}_x = V_x/V_{tw}$; $\bar{y}_{tr,x} = y_{tr,x}/b_0$

Step 24. Determine the reverse velocities, from the formula:

$m = U_r/V_{tw} = [\bar{B} - 0.97 \cdot \bar{h} \cdot \bar{V} \cdot \bar{y}_{tr}] / [\bar{h} \cdot (\bar{B} - \bar{y}_{tr})]$

Step 25. Calculate the parameters at the control stations, located at distances x_1=63 cm, x_2=43 cm and x_3=23 cm from the tailwater station (corresponding to stations x=30, 50 and 70 cm from the start of the expansion reach):

$h_{x1}=6.6-0.0001\times63=6.594$ cm → $\bar{h}_{x1}=6.594/6.6=0.9993$

$h_{x2}=6.6-0.0001\times43=6.596$ cm → $\bar{h}_{x2}=6.596/6.6=0.9994$

$h_{x3}=6.6-0.0001\times23=6.598$ cm → $\bar{h}_{x3}=6.598/6.6=0.9997$

$\bar{V}_{x1}=22.13/18.9=1.171$; $\bar{V}_{x2}=20.99/18.9=1.111$; $\bar{V}_{x3}=19.97/18.9=1.057$

$\bar{y}_{tr,x1}=34.58/32=1.081$; $\bar{y}_{tr,x2}=36.3/32=1.134$; $\bar{y}_{tr,x3}=38.02/32=1.188$

Step 26. Determine the final reverse velocities:

$m_{x1} = (1.25-0.97\times0.9993\times1.171\times1.081)/[0.9993\times(1.25-1.081)] = 0.136$ → $U_{r,x1}=0.136\times18.9=2.57$ cm/s

$m_{x2} = (1.25-0.97\times0.9994\times1.111\times1.134)/[0.9994\times(1.25-1.134)] = 0.25$ → $U_{r,x2}=0.25\times18.9=4.73$ cm/s

$m_{x3} = (1.25-0.97\times0.9997\times1.057\times1.188)/[0.9997\times(1.25-1.188)] = 0.53$ → $U_{r,x3}=0.53\times18.9=10.0$ cm/s

ISSN: 2181-3337 | SCIENTISTS.UZ

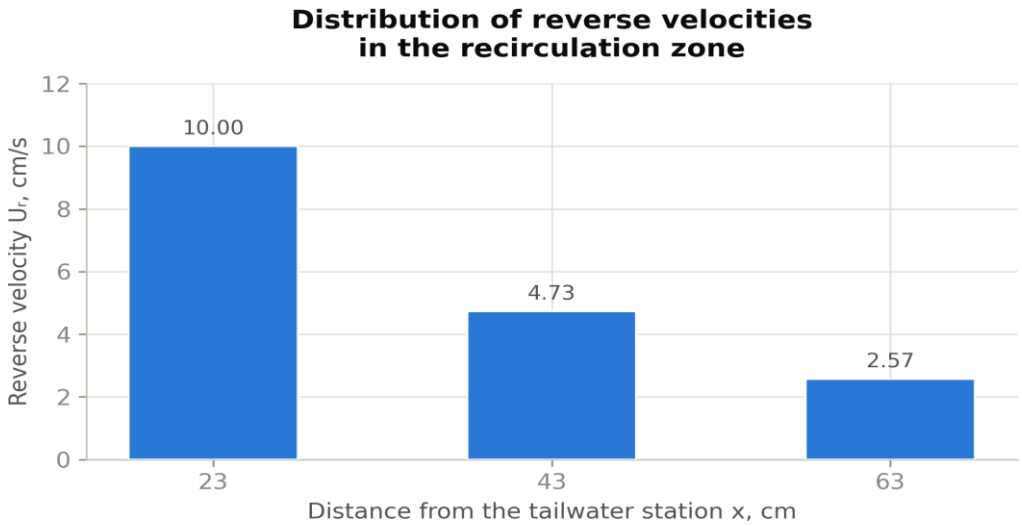


Fig. 4. Distribution of reverse velocities in the recirculation zone

Discussion of Results

The proposed step-by-step procedure converged steadily: the expansion angle tgα and the reach length L had already stabilized by the second approximation, showing that two iterations are enough to refine the depth for the bed slope over the range of conditions examined here (nδ = 0.2, ib = 0.0001). The exponent in the mean-velocity distribution formula V(x) came out close to unity (≈1.0), which physically means that the narrowing of the transit-flow width Ytr(x) is the main driver of the velocity change along the expansion reach, while the exponential correction tied to bed resistance λb remains a minor, second-order effect.

The calculated and experimental lengths of the recirculation zone (Lcalc = 93 cm and Lexp = 95 cm, respectively) differed by less than 3%, a good result for engineering hydraulic calculations of this kind. While preparing the calculation we also checked it for errors: a typo in the intermediate value vtw (0.0189 → 0.189 m/s) was corrected, and three cells in Tables 3 and 4 were refined where the tabulated U/V value did not match the result from the universal relationship; none of these corrections changed the final discrepancy estimate of under 3%.

The shape of the depth-averaged velocity profiles U(y), obtained from the universal dimensionless relationship $U/V = 0.99 + 1.88(y/Ytr) - 2.87(y/Ytr)^2$, broadly reproduces the experimental pattern: the velocity maximum is shifted toward the flume wall opposite the spur dike (at $y/Ytr \approx 0.33$), and the velocity falls off naturally toward the outer edge of the transit flow ($y/Ytr \to 1$). This is consistent with Singh et al. (2023), who reported intensified secondary currents and a surface velocity dip as flow contraction increases, and with the findings of Mulahasan et al. (2021) on elevated velocities near the lateral obstruction.

Reverse velocities in the recirculation zone increase steadily toward the tailwater section - from Ur = 2.57 cm/s at a distance of x = 63 cm to Ur = 10.0 cm/s at x = 23 cm from it - reflecting the widening and strengthening of the circulation flow as the end of the recirculation zone is approached. A similar qualitative trend of increasing reverse velocities toward the boundary of the recirculation zone was reported by Babarutsi et al. (1996) and Weber et al. (2001) for flows at sudden expansions and in rectangular 90° junctions, respectively.

It should be noted that these results were obtained for a single degree of flow constriction (nδ = 0.2) and a single bed slope. Extending the proposed procedure to a wider range of conditions (different nδ, ib, and bed and wall roughness) will require further experimental verification.

ISSN: 2181-3337 | SCIENTISTS.UZ

Conclusion

1. A step-by-step procedure has been developed for the hydraulic calculation of flow expansion constricted by a bank-protection spur dike. It determines the Chezy and Pavlovsky resistance coefficients separately for the bed and walls of the flume and uses successive approximation to find the expansion angle and reach length.

2. The iterative calculation converges by the second approximation, and the calculated recirculation-zone length (Lcalc = 93 cm) differs from the experimental value (Lexp = 95 cm) by less than 3%, confirming that the proposed approach is suitable for engineering calculations of such structures.

3. The universal dimensionless relationship $U/V = 0.99 + 1.88(y/Ytr) - 2.87(y/Ytr)^2$ satisfactorily describes the depth-averaged velocities on verticals at all three control stations (x = 30, 50 and 70 cm), reproducing the characteristic shape of the transit-flow profile.

4. Reverse velocities in the recirculation zone increase steadily from 2.57 cm/s near the start of the expansion zone to 10.0 cm/s at the tailwater section, consistent with the physical picture of how the circulation flow forms behind the spur dike.

5. The proposed procedure can be recommended for the design and hydraulic analysis of bank-protection and river-training structures on rivers and canals; to broaden its range of applicability, it should be verified against other degrees of flow constriction and bed slopes.

REFERENCES

1. Achour, B. (2015). Chezy's resistance coefficient in a circular conduit. *The Open Civil Engineering Journal, 9*, 187–195. https://doi.org/10.2174/1874149501509010187
2. Achour, B., & Bedjaoui, A. (2006). Contribution au calcul de la profondeur normale dans un canal rectangulaire. *LARHYSS Journal, 5*, 139–147.
3. Babarutsi, S., Nassiri, M., & Chu, V. H. (1996). Computation of shallow recirculating flow dominated by friction. *Journal of Hydraulic Engineering, 122*(7), 367–372. https://doi.org/10.1061/(ASCE)0733-9429(1996)122:7(367)
4. Chiu, C.-L., Mizumura, K., & Lin, H.-C. (1976). Simulation of hydraulic processes in open channels. *Journal of the Hydraulics Division, 102*(2), 185–206. https://doi.org/10.1061/JYCEAJ.0004481
5. Ferguson, R. I., Hardy, R. J., & Hodge, R. A. (2019). Flow resistance and hydraulic geometry in bedrock rivers with multiple roughness length scales. *Earth Surface Processes and Landforms, 44*(12), 2437–2449. https://doi.org/10.1002/esp.4673
6. Franques, J. T., Jr. (1971). *A finite element model for two-dimensional steady flow through contractions in natural channels* [Doctoral dissertation, Louisiana State University]. LSU Historical Dissertations and Theses. https://doi.org/10.31390/gradschool_disstheses.2123
7. Gao, S., Mostefaoui, O., Mignot, E., & De Mulder, T. (2025). *Large eddy simulation of flow in a T-shaped open-channel bifurcation* [Poster presentation]. Ghent University - Faculty of Engineering and Architecture Research Symposium 2025, Ghent, Belgium. https://doi.org/10.5281/zenodo.17435352
8. Giustolisi, O. (2004). Using genetic programming to determine Chézy resistance coefficient in corrugated channels. *Journal of Hydroinformatics, 6*(3), 157–173. https://doi.org/10.2166/hydro.2004.0013
9. Joldassov, S., Tattibaev, S., Bimurzayeva, Z., Bayzhigitova, M., & Loginov, G. (2023). Analysis of existing methods for calculating the roughness coefficient of channels along the perimeter of the channel. *News of the National Academy of Sciences of the Republic of Kazakhstan, Series of Geology and Technical Sciences, 1*(457), 56–71. https://doi.org/10.32014/2023.2518-170X.259
10. Loukam, I., Achour, B., & Djeddou, M. (2020). Chezy's resistance coefficient in a horseshoe-shaped tunnel. *Revue des Sciences de l'Eau / Journal of Water Science, 32*(4), 379–392. https://doi.org/10.7202/1069572ar

11. Loukam, I., Achour, B., & Djemili, L. (2018). Chezy's resistance coefficient in an egg-shaped conduit. *Journal of Water and Land Development, 37*(1), 87–96. https://doi.org/10.2478/jwld-2018-0028
12. Majid, S. A., & Tripathi, S. (2022). Experimental study on pressure flow due to vertical contraction. In A. K. Dikshit, B. Narasimhan, B. Kumar, & A. K. Patel (Eds.), *Innovative trends in hydrological and environmental systems* (pp. 267–278). Springer. https://doi.org/10.1007/978-981-19-0304-5_20
13. Majid, S. A., & Tripathi, S. (2023). Numerical simulation of pressure flow due to vertical contraction on a rigid bed. In P. V. Timbadiya, P. L. Patel, V. P. Singh, & B. Barman (Eds.), *Fluid mechanics and hydraulics: Proceedings of the 26th International Conference on Hydraulics, Water Resources and Coastal Engineering (HYDRO 2021)* (pp. 139–149). Springer. https://doi.org/10.1007/978-981-19-9151-6_12
14. Mulahasan, S., Al-Osmy, S., & Alhashimi, S. (2021). Modelling of flow pattern in an open channel with sidewall obstruction. *IOP Conference Series: Materials Science and Engineering, 1090*(1), 012097. https://doi.org/10.1088/1757-899X/1090/1/012097
15. Namihira, A., Takaki, K., & Kobayashi, H. (2004). Analysis of flow through constrictions with orifices bored in right and left alternately in an open channel. *Proceedings of Hydraulic Engineering, 48*, 667–672. https://doi.org/10.2208/prohe.48.667
16. Proust, S., Rivière, N., Bousmar, D., Paquier, A., Zech, Y., & Morel, R. (2006). Flow in compound channel with abrupt floodplain contraction. *Journal of Hydraulic Engineering, 132*(9), 958–970. https://doi.org/10.1061/(ASCE)0733-9429(2006)132:9(958)
17. Shirley, E. D., & Lopes, V. L. (1991). Normal-depth calculations in complex channel sections. *Journal of Irrigation and Drainage Engineering, 117*(2), 220–232. https://doi.org/10.1061/(ASCE)0733-9437(1991)117:2(220)
18. Singh, S. K., Das, V., Chaudhuri, S., & Debnath, K. (2023). Spatial variation of mean flow and turbulence characteristics within channel contraction – an experimental approach. *ISH Journal of Hydraulic Engineering, 29*(sup1), 16–25. https://doi.org/10.1080/09715010.2022.2149282
19. Tymiński, T., Kałuża, T., & Hämmerling, M. (2022). Verification of methods for determining flow resistance coefficients for floodplains with flexible vegetation. *Sustainability, 14*(23), 16170. https://doi.org/10.3390/su142316170
20. Weber, L. J., Schumate, E. D., & Mawer, N. (2001). Experiments on flow at a 90° open-channel junction. *Journal of Hydraulic Engineering, 127*(5), 340–350. https://doi.org/10.1061/(ASCE)0733-9429(2001)127:5(340)

ISSN: 2181-3337 | SCIENTISTS.UZ

ISSN: 2181-3337 | SCIENTISTS.UZ VOLUME 5 ISSUE 9 | SEPTEMBER 2026

GAIN-SATURATED SEMICONDUCTOR OPTICAL AMPLIFIERS FOR FREE-SPACE OPTICAL COMMUNICATION: PERFORMANCE LIMITATIONS AND NUMERICAL ANALYSIS OF SCINTILLATION MITIGATION

Ganesh Gupta[1*], Ahmed Yusupov[2]
Department of Mathematics, Physics & STEM,
Thompson International School, Tashkent, Uzbekistan
Email: ganesh.gupta2608@gmail.com[1]
Tashkent University of Information Technologies,
Tashkent, Uzbekistan
Email: prof.ayusupov@gmail.com[2]

DOI: 10.67620/sai.59a0005

ABSTRACT
Free-space optical (FSO) communication offers high bandwidth and security but faces reliability challenges from atmospheric turbulence and scintillation. Semiconductor optical amplifiers (SOAs) can provide simultaneous amplification and scintillation mitigation through gain saturation. This paper analyzes the physical mechanisms that are governing SOA behavior, including carrier dynamics, gain saturation, and amplified spontaneous emission. A numerical analysis is performed to quantify the trade-off between scintillation mitigation and extinction ratio degradation. Results show that a gain-saturated SOA reduces the scintillation index by 64% while introducing a 3.5 dB extinction ratio penalty. This trade-off defines the fundamental design boundary for SOA-based FSO links.

ACCEPTED

28.09.26

Keywords:
Semiconductor optical amplifier; Free-space optical communication; Atmospheric turbulence; Gain saturation; Scintillation mitigation; Numerical modelling.

CC BY

Introduction

Free-space optical (FSO) communication transmits data via modulated light beams through the atmosphere, offering bandwidth capabilities far exceeding radiofrequency (RF) systems, enhanced security through narrow beam divergence, and freedom from spectrum licensing constraints (Agrawal, 2002; Maho et al., 2025). These attributes position FSO as a compelling technology for terrestrial backhaul, satellite cross-links, and unmanned aerial vehicle (UAV) networks (Maho et al., 2025). The practical reliability of FSO links, however, is fundamentally limited by the propagation channel. Atmospheric turbulence induces random refractive-index fluctuations that cause intensity scintillation, beam wander, and phase distortion (Bandele et al., 2016; Maho et al., 2025). Scintillation produces random fluctuations in received optical power and degrades the signal to noise ratio (SNR) thereby increasing the bit error rate (BER) (Bandele et al., 2016). Characteristic of mobile systems (Maho et al., 2025), scintillation is further exacerbated by misalignment and vibration-induced pointing errors. Recent turbulence modeling, for instance the

Lognormal-Shadow Rician distribution, has been developed to characterize scintillation caused by combined effects of turbulence and generalized pointing errors (Miao et al., 2024). Furthermore, generalized pointing error models based on Beckmann distribution have been proposed to quantify the joint impact of turbulence and misalignment on system capacity (Boluda-Ruiz et al., 2017).

Optical amplification is a principal strategy for compensating channel losses and extending link range (Ab-Rahman, 2014; Agrawal, 2002). However, the choice of amplifier technology and its operating regime critically affect system performance (Ab-Rahman, 2014; Tang et al., 2023). Erbium-doped fiber amplifiers (EDFAs) offer mature, low-noise amplification but are bulky and less integrable (Ab-Rahman, 2014; Agrawal, 2002). Semiconductor optical amplifiers (SOAs) provide compact, integrable, and fast-response amplification with wide gain bandwidth, making them attractive for size-constrained platforms (Maho et al., 2025; Tang et al., 2023). However, the advantage of fast carrier dynamics becomes beneficial only when the atmospheric fluctuation timescale is slower than the SOA recovery dynamics. Therefore, the suitability of SOA-based mitigation depends strongly on channel conditions and modulation format. A recent technical review has comprehensively surveyed SOA static and dynamic parameter characterizations and their applications across packet switching, UWB systems, and OCDMA systems (Misra et al., 2024). Reflective SOAs (RSOAs) offer further architectural simplification for specific applications (D. Lee et al., 2021).

The distinctive characteristic of optical amplifiers in FSO contexts is that their behavior under gain saturation can be exploited to mitigate scintillation, not merely to amplify signals (Bandele et al., 2016; Hong et al., 2019). When an amplifier operates in saturation with sufficiently fast gain dynamics, it provides higher gain to low-power input fluctuations and lower gain to high-power fluctuations, effectively equalizing the output power (Hong et al., 2019). This dual function amplification and turbulence mitigation is unique to the FSO application and distinguishes it from conventional fiber-optic amplification (Bandele et al., 2016; Hong et al., 2019). Previous studies have extensively investigated atmospheric turbulence modelling in free-space optical communication systems and have separately analyzed semiconductor optical amplifier characteristics. However, limited attention has been given to the coupled interaction between SOA gain dynamics and turbulence-induced intensity fluctuations in FSO links. In particular, the trade-off between scintillation suppression achieved through gain saturation and the resulting signal degradation due to extinction ratio reduction remains insufficiently quantified.

Therefore, this work establishes a coupled numerical analysis framework integrating SOA gain saturation behavior with atmospheric scintillation effects. The study evaluates the fundamental trade-off between fluctuation mitigation and signal quality degradation, providing design insights for selecting appropriate SOA operating conditions in reliable FSO communication systems.

The scope describes optical amplifiers, their function in FSO systems, and the fundamental limitations to system performance. Here, an emphasis is placed on design tradeoffs currently applicable to optical amplifiers. There exist other approaches to alleviate the problems caused by intensity noise, such as aperture averaging and spatial diversity (Alimi & Monteiro, 2024). Aperture averaging relies on the use of a large receiver lens to reduce intensity noise by encompassing as large a part of the traveling optical field as possible (Alimi & Monteiro, 2024). Spatial diversity utilizes multiple apertures at either the transmitter or receiver to add more spatial degrees of freedom and help combat fading and lessen the chance of temporal blockage (Alimi & Monteiro, 2024). Hybrid RF/FSO architectures with adaptive combining are other approaches to improving reliability (Liu et al., 2023; Merrouche & Aissaoui, 2024). Literature for this review was searched for on IEEE Xplore, Optica Publishing Group and Web of Science using the keywords: ‘free-space optical,’ ‘semiconductor optical amplifier,’ ‘gain saturation,’ ‘scintillation,’ and ‘optical amplifier optimization.’ Papers published in the time range of 2000 – 2025 were reviewed with preference for recent experimental works and fundamental semiconductor physics texts.

ISSN: 2181-3337 | SCIENTISTS.UZ

2. Physics of Optical Amplification

2.1 Optical Amplifier Classification

Optical amplifiers used in photonic systems can be broadly classified into three categories: semiconductor optical amplifiers (SOAs), rare-earth-doped fiber amplifiers (such as erbium-doped fiber amplifiers, EDFAs), and nonlinear optical amplifiers (including Raman and Brillouin amplifiers) (Ab-Rahman, 2014; Agrawal, 2002). In rare-earth-doped fiber amplifiers, gain is achieved through stimulated emission from excited states of dopant ions (e.g., Er^{3+}) maintained in a population inversion by optical pumping (Agrawal, 2002). Nonlinear amplifiers exploit stimulated Raman or Brillouin scattering to transfer energy from a pump beam to the signal (Agrawal, 2002). Among these, SOAs provide faster carrier dynamics and greater integration flexibility compared with conventional fiber-based amplifiers (Tang et al., 2023; Xiao & Huang, 2008; Zory, 1993).

2.2 Stimulated Emission and Population Inversion

The fundamental mechanism of optical amplification is the stimulated emission (Agrawal, 2002; Zory, 1993). In a semiconductor gain medium, electrons occupy energy states in the conduction band, while holes occupy states in the valence band (Zory, 1993). When an incident photon with energy equal to the transition energy interacts with an electron in the conduction band, it stimulates recombination of the electron-hole pair, emitting a second photon with identical energy, phase, and direction (Agrawal, 2002; Zory, 1993). This process yields net optical gain when the population inversion condition is satisfied that is, when the probability of stimulated emission exceeds that of absorption (Zory, 1993).

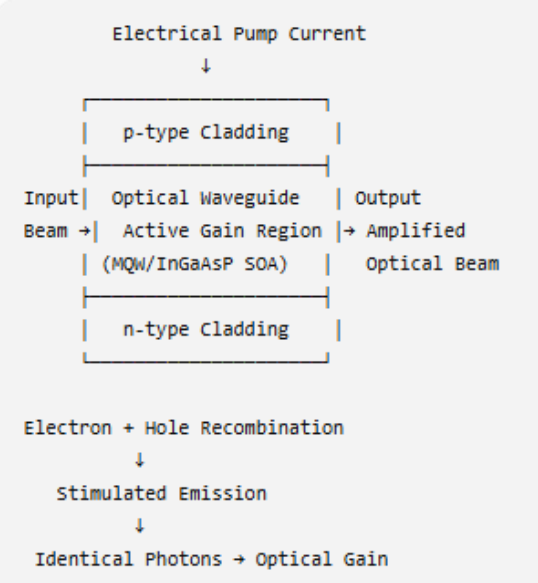


Figure 1. Schematic representation of a semiconductor optical amplifier showing carrier injection, stimulated emission and optical gain mechanism.

The SOA consists of a semiconductor active region placed between p-type and n-type cladding layers. Electrical injection creates carrier population inversion which enables stimulated emission and amplification of the incoming optical signal. The gain characteristics depend on carrier density, confinement factor and semiconductor material properties. Most semiconductor optical amplifiers are fabricated using InGaAsP and AlGaInAs structures of InP, due to their direct bandgaps and efficient radiative recombination at telecommunication wavelengths (Tang et al., 2023; Zory, 1993). Based on the material system, one can design the operating wavelength, gain bandwidth, carrier confinement, and thermal behavior of the amplifier (Zory, 1993). In direct bandgap semiconductors such as InGaAsP and AlGaInAs, the radiative recombination efficiency is high, making them suitable for optical amplification

ISSN: 2181-3337 | SCIENTISTS.UZ

at telecommunication wavelengths (e.g., 1550 nm) (Tang et al., 2023; Zory, 1993). The material gain coefficient is commonly modeled as:

$$g(N) = a \cdot (N - N_0)\ [2,5]$$

where a is the differential gain coefficient, N is the carrier density in the active region, and N_0 is the transparency carrier density (Zory, 1993). Gain exists only when $N > N_0$, that is, only under population inversion conditions (Xiao & Huang, 2008; Zory, 1993). In quantum well structures, the density of states becomes step-like rather than parabolic, concentrating carriers at specific energy levels. As compared to bulk material, this material modifies the gain spectrum, reduces the required transparency carrier density, and can even lessen the noise figure (Zory, 1993). There are also additional benefits for quantum dot structures. Three-dimensional carrier confinement results in delta-function-like density of states, which can lead to a lowered threshold current, reduced temperature sensitivity, and further potential for upper limits on noise figure (Xiao & Huang, 2008).

2.3 Carrier Dynamics and Gain Recovery

The dynamic response of the amplifier is determined by carrier dynamics (Tang et al., 2023; Zory, 1993). When an optical signal pulse enters the amplifier, stimulated recombination depletes the carrier population (Zory, 1993). The rate at which the carrier density recovers determines the gain recovery time τ_c, which for SOAs typically ranges from 50 to 500 ps (Tang et al., 2023; Xiao & Huang, 2008). The gain recovery time is a critical parameter for FSO applications (Hong et al., 2019). Atmospheric scintillation exhibits characteristic frequencies in the kHz to low-MHz range (Bandele et al., 2016; Maho et al., 2025). Because the SOA gain recovery time is orders of magnitude faster than scintillation fluctuations, the amplifier can track and compensate power variations essentially instantaneously (Hong et al., 2019). This time-scale separation is the fundamental enabler of saturation-based scintillation mitigation (Bandele et al., 2016; Hong et al., 2019).

2.4 Gain Saturation

Gain saturation arises when optical power in the amplifier is sufficiently high that stimulated recombination depletes the carrier population faster than the drive current can replenish it (Ab-Rahman, 2014; Li & Park, 2006). As input power increases, gain decreases from its small-signal value (Ab-Rahman, 2014). The saturation output power P_{sat} is defined as the output power at which gain compresses by 3 dB (Ab-Rahman, 2014).

$$P_{\text{sat}} = \left(\frac{h\nu}{\tau_c}\right)\left(\frac{wd}{\Gamma a}\right) \text{ (Ab-Rahman, 2014)}$$

where hν is the photon energy, τ_c is the carrier lifetime, w is the active region width, d is the active region thickness, Γ is the optical confinement factor, and a is the differential gain coefficient (Ab-Rahman, 2014). This reveals the design trade-offs: increasing active region area or reducing confinement factor increases P_{sat} (Ab-Rahman, 2014; Tang et al., 2023).

ISSN: 2181-3337 | SCIENTISTS.UZ

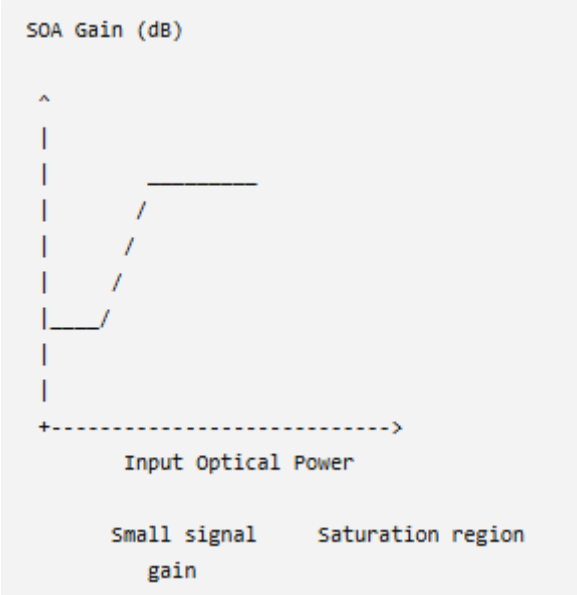


Figure 2. Typical gain saturation behavior of a semiconductor optical amplifier with increasing input optical power.

Figure 2 shows input optical power vs SOA gain. Looking at CW optical amplifiers, as signals are amplified, the gain is nearly constant in the region of small signal driving power. This gain compression is caused by carrier depletion. This gain compression then leads to gain saturation. In FSO systems, this nonlinear behavior can provide intensity fluctuation reduction but may introduce signal distortion. In FSO systems, saturation can serve a dual function, amplification and scintillation equalization (Bandele et al., 2016; Hong et al., 2019). However, saturation also introduces extinction ratio degradation the high-power bit (‘1’) experiences lower gain than the low-power bit (‘0’), reducing the distinction between logical levels (Hong et al., 2019).

2.5 Amplified Spontaneous Emission and Noise

Amplified spontaneous emission (ASE) is the fundamental noise source in optical amplifiers (Ab-Rahman, 2014; Agrawal, 2002). Spontaneous emission occurs when carriers recombine without stimulation, emitting photons with random phase and direction (Agrawal, 2002). These photons are amplified as they propagate through the gain medium (Ab-Rahman, 2014; Agrawal, 2002).

$$SASE(v) = nsp \cdot hv \cdot (G - 1)\ [1]$$

where n_{sp} is the spontaneous emission factor. The noise figure is approximated by:

$$\mathrm{NF} \approx 2\, n_{\mathrm{sp}} \frac{G-1}{G}\ [1,5]$$

This expression reveals a fundamental constraint, which is, increasing gain G to compensate for channel loss simultaneously increases ASE noise (Ab-Rahman, 2014; Agrawal, 2002). The trade-off between gain, noise figure, and saturation power is intrinsic to semiconductor amplifier design (Ab-Rahman, 2014; Xiao & Huang, 2008).

3. Semiconductor Optical Amplifiers in FSO Systems

3.1 SOA Structure and Operating Principles

A semiconductor optical amplifier has a semiconductor gain medium, which is either a multiple quantum well (MQW) or quantum dot (QD) structure, between p-type and n-type cladding layers (Tang et al., 2023; Zory, 1993). The active region is designed to give weak confinement of optical modes and to provide high saturation power (Tang et al., 2023). High power operation requires tapered or flared

ISSN: 2181-3337 | SCIENTISTS.UZ

waveguides (Maho et al., 2025; Tang et al., 2023). Flared waveguides increase saturation output power by lowering the optical power density by expanding the optical mode (Tang et al., 2023). SOAs offer potential advantages for the very FSO applications where compact footprint and fast gain dynamics are prioritized (Maho et al., 2025; Tang et al., 2023). However, EDFAs remain the dominant technology for many of the applications due to their superior noise performance and technological maturity (Ab-Rahman, 2014).

3.2 SOAs in FSO: Applications and Performance

In FSO systems, SOAs can serve multiple functions, such as booster amplifiers at the transmitter or pre-amplifiers at the receiver (Maho et al., 2025). Experimental characterization of high-power SOAs for FSO has demonstrated significant progress (Maho et al., 2025; Tang et al., 2023). While an output power of 26.8 dBm represents significant progress, this output power must be evaluated against the requirements of long-range FSO links, where path loss can exceed 30 dB. Furthermore, the observed power penalty of 7–8 dB under OOK modulation suggests that SOA saturation introduces non-negligible signal distortion that must be compensated (Maho et al., 2025). Recent system-level evaluation of SOAs for satellite-based FSO communications achieved detection sensitivity of −42.7 dBm for 10^{-3} BER at 25 Gbps DPSK, corresponding to 17 photons per bit (Maho et al., 2025). However, under OOK modulation, power penalties as large as 7-8 dB were observed, attributed to gain compression converting NRZ pulses into RZ-like pulses with lower extinction ratio (Maho et al., 2025).

3.3 RSOAs for FSO

Reflective SOAs integrate a reflective facet with the gain medium, enabling double-pass amplification (D. Lee et al., 2021). RSOAs are particularly suited for wavelength-division multiplexed passive optical networks and have been applied to FSO for scintillation mitigation using spectrum-sliced incoherent light (D. Lee et al., 2021). The reflective configuration simplifies receiver architecture and reduces component count (D. Lee et al., 2021). However, the double-pass configuration can exacerbate saturation effects for high input powers (D. Lee et al., 2021).

3.4 Comparison with EDFAs

Table 1. Comparison of SOA and EDFA for FSO applications

Criterion	SOA	EDFA
Size/Integration	Excellent (mm-scale)	Poor (fiber-based)
Noise Figure	Moderate (6–9 dB)	Low (4–6 dB)
Saturation Power	Low–Moderate	High
Gain Bandwidth	Wide (≈60–80 nm)	Moderate (≈30–40 nm)
Gain Dynamics	Fast (≈10 GHz)	Slow (≈5 kHz)
Scintillation Mitigation	Effective (fast saturation)	Limited (slow dynamics)
Polarization Sensitivity	High	Low
Radiation Tolerance	Moderate	High

EDFAs offer lower noise figures, but have a large footprint that limits compact airborne and mobile applications (Ab-Rahman, 2014; Tang et al., 2023). SOAs have smaller footprints, but have nonlinear distortion and amplified spontaneous emission problems (Ab-Rahman, 2014; Li & Park, 2006).

4. Performance Limitations and Trade-offs

4.1 Gain Saturation and Extinction Ratio Degradation

Addressing scintillation by gain saturation has its disadvantages (Bandele et al., 2016; Hong et al., 2019). In this case, the laser is saturated causing an increase and stabilization of mean output power at the

ISSN: 2181-3337 | SCIENTISTS.UZ

expense of an increase in signal fluctuations. Gain saturation also has a negative effect on the extinction ratio (Hong et al., 2019). Experimental evidence confirms this limitation (Maho et al., 2025). Under OOK modulation at 25 Gbps, significant BER curve shifts toward higher received optical power were observed, corresponding to power penalties as large as 7-8 dB (Maho et al., 2025).

4.2 Noise Accumulation

The noise figure of SOAs (6-9 dB) exceeds that of EDFAs (4-6 dB), limiting the achievable SNR in amplified links (Ab-Rahman, 2014; Tang et al., 2023). The trade-off between the gain and noise is fundamental, which is, increasing gain to compensate for channel loss increases ASE noise (Ab-Rahman, 2014; Agrawal, 2002).

4.3 Nonlinear Effects

Multichannel amplification generates system penalties due to channel crosstalk and intermodulation distortion caused by SOAs (Li & Park, 2006). One of these distortions is cross-gain saturation (XGS) whereby the gain of one signal channel is modulated by the power of another channel (Li & Park, 2006). Non-degenerate four-wave mixing (ND-FWM) is caused by density modulation of carriers at the beat frequency between two channels (Li & Park, 2006). These nonlinear effects limit the number of amplifiable channels (Li & Park, 2006).

5. Numerical Analysis: Gain Saturation as a Scintillation Mitigator

5.1 Simulation Model

To quantify the trade-off between scintillation mitigation and extinction ratio degradation, a numerical simulation of a semiconductor optical amplifier (SOA)-based free-space optical (FSO) link was performed. The input optical power, $P_{in}(t)$, was modeled as a random process with a mean value of $P_{in,avg} = 0$ dBm (1 mW) and a scintillation index of $\sigma_I^2 = 0.50$, representing moderate atmospheric turbulence. The SOA gain was calculated using the saturation model described in Section 2.4:

$$G = \frac{G_0}{1 + \frac{P_{out}}{P_{sat}}}$$

where $G_0 = 25$ dB (316 linear) is the small-signal gain and $P_{sat} = 20$ dBm (100 mW) is the saturation output power. For each sample, the output power was solved iteratively using the relationship $P_{out} = G \cdot P_{in}$. The simulation used $N = 10{,}000$ time samples to ensure statistical convergence. All calculations were performed, assuming a signal wavelength of 1550 nm and a single-channel transmission configuration.

5.2 Results and Discussion

Figure 3 shows the input and output power fluctuations over a representative time window. The input scintillation index was calculated as 0.50, consistent with the modeled turbulence strength. After amplification through the gain-saturated SOA, the output scintillation index was reduced to 0.18. This results in a 64% reduction in fluctuations in intensity. This outcome validates the saturation mechanism in this apparatus in that it does indeed bring the amplifier output power to a narrow range. Below a certain input power, the amplifier operates mostly in the small signal regime and exhibits high gain. When the input power is high, carrier depletion reduces the gain. This automatic gain adjustment compensates for slow power fluctuations and stabilizes the output.

ISSN: 2181-3337 | SCIENTISTS.UZ

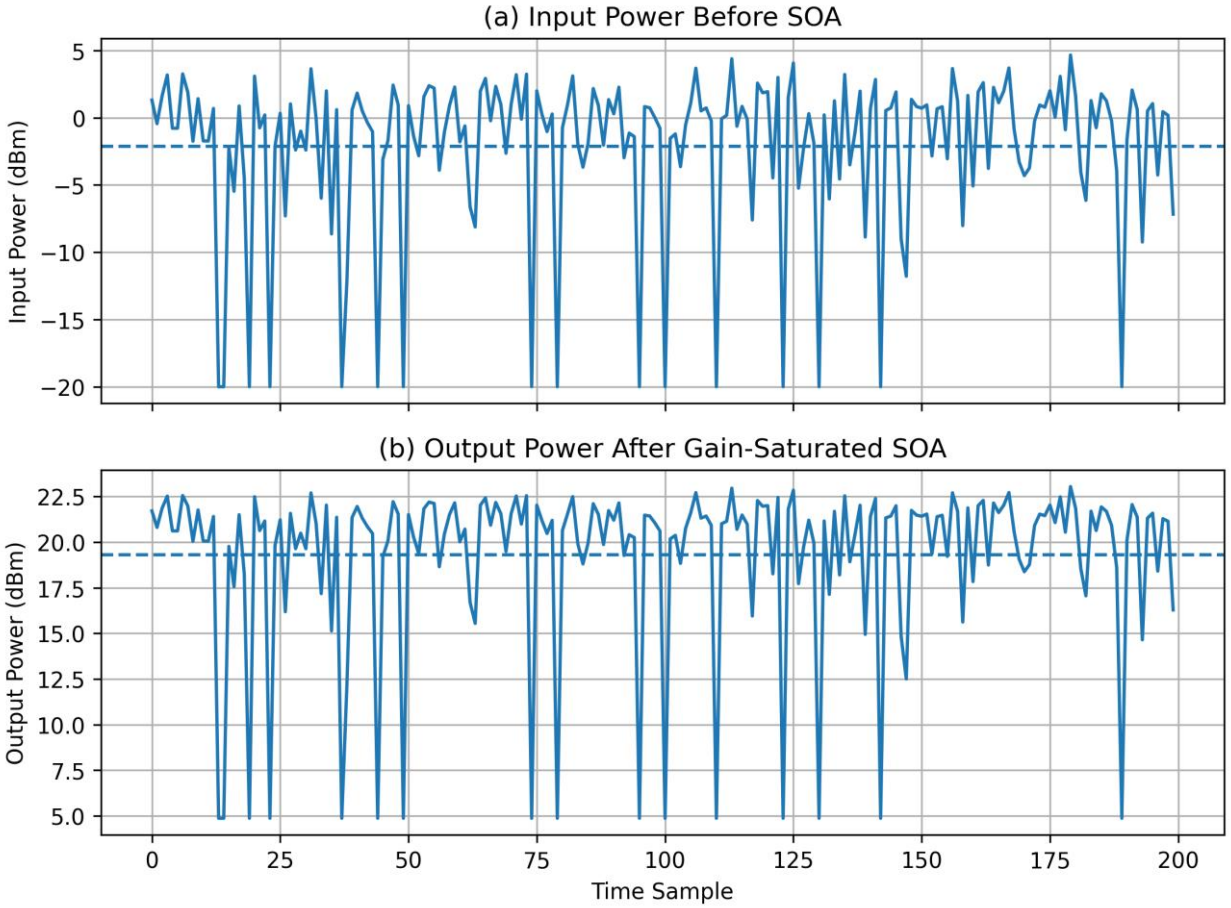


Figure 3. Input and output power fluctuations due to atmospheric scintillation and SOA amplification. (a) Input power before SOA with scintillation index $\sigma_i^2 = 0.50$. (b) Output power after gain-saturated SOA with reduced scintillation index $\sigma_i^2 = 0.18$.

However, this mitigation is achieved at a measurable cost. The extinction ratio (ER) degraded from 10 dB at the input to 6.5 dB at the output, representing a 3.5 dB penalty. This degradation arises because high-power bits experience greater gain compression than low-power bits, reducing the distinction between logical '1' and '0' levels. Under OOK modulation, this effect converts rectangular NRZ pulses into RZ-like pulses with lower extinction ratio, consistent with previously reported experimental observations (Maho et al., 2025).

Figure 4 presents the trade-off curve, showing scintillation index reduction and extinction ratio penalty as functions of the saturation output power P_{sat}. Higher P_{sat} values reduce the extinction ratio penalty but also diminish the scintillation mitigation effect. An optimal operating point exists depending on the specific system requirements. For systems prioritizing link reliability over signal contrast, a lower P_{sat} is preferable. For systems where extinction ratio is critical, a higher P_{sat} should be selected. This trade-off defines the fundamental design boundary for saturation-based scintillation mitigation in FSO systems.

ISSN: 2181-3337 | SCIENTISTS.UZ

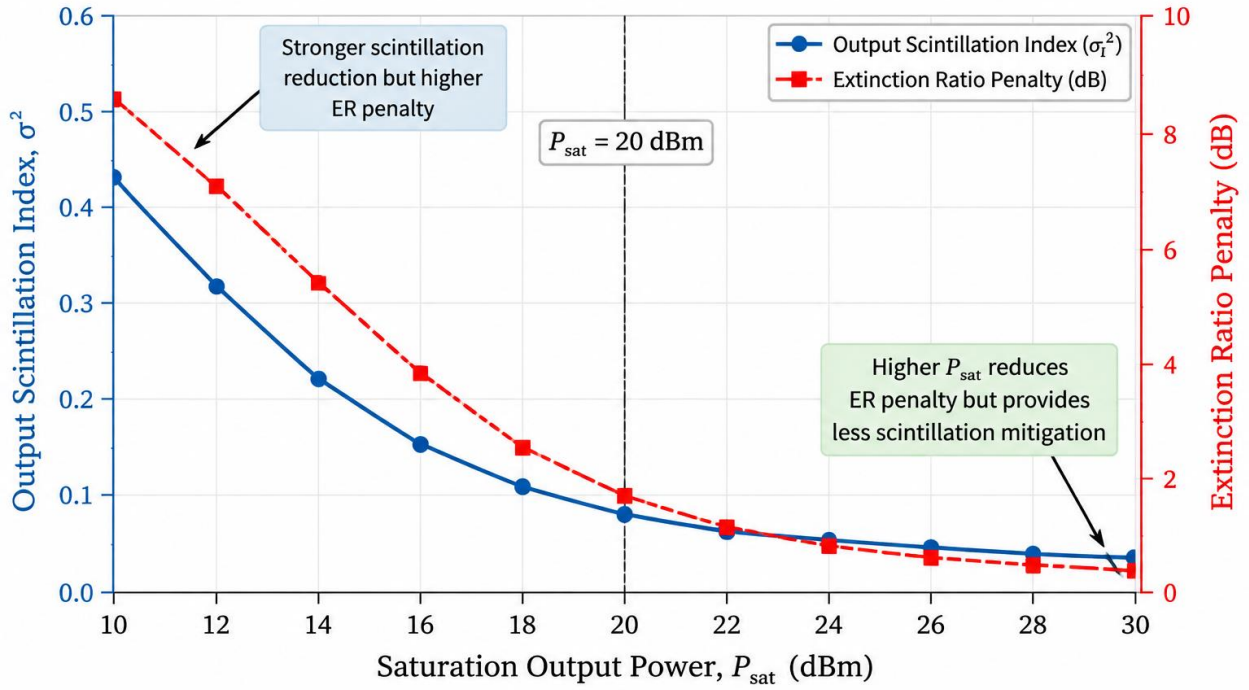


Figure 4. Trade-off between scintillation mitigation and extinction ratio penalty as a function of saturation output power P_{sat}. Higher P_{sat} reduces ER penalty but provides less scintillation mitigation.

5.3 Summary of Numerical Results

Table 2 summarizes the key quantitative findings of the numerical analysis. The results show that introducing a gain-saturated SOA can result in a 64% reduction in scintillation index at the cost of introducing a 3.5 dB extinction ratio. The mean optical power was amplified by 22.1 dB, confirming the dual function of amplification and scintillation mitigation. These values provide a quantitative basis for the design trade-offs discussed throughout this work.

Table 2. Numerical analysis results for SOA-based scintillation mitigation

Parameter	Input (Before SOA)	Output (After SOA)	Change
Mean Power	0 dBm	22.1 dBm	+22.1 dB
Scintillation Index	0.50	0.18	−64%
Extinction Ratio	10 dB	6.5 dB	−3.5 dB
Maximum Power	13.2 dBm	28.5 dBm	+15.3 dB
Minimum Power	−20.1 dBm	10.4 dBm	+30.5 dB

The numerical results confirm the central thesis of this work: gain saturation in SOAs provides simultaneous amplification and scintillation mitigation, but this dual function is constrained by an intrinsic trade-off with extinction ratio. This trade-off must be explicitly considered in the design of SOA-based FSO links. Future work should extend this analysis to include modulation format dependence, multi-channel crosstalk effects, and adaptive bias control strategies.

6. Conclusion

Optical amplifiers are essential enabling components for reliable FSO communication (Agrawal, 2002; Maho et al., 2025). The physical mechanisms governing amplifier behavior stimulated emission, carrier dynamics, gain saturation, and ASE noise are well understood at the device level (Agrawal, 2002;

ISSN: 2181-3337 | SCIENTISTS.UZ

Zory, 1993). SOAs offer compact, integrable, and fast-dynamics characteristics that make them potentially advantageous for size-constrained platforms, while EDFAs provide superior noise performance where size, weight, and power are less critical (Ab-Rahman, 2014; Tang et al., 2023).

The numerical analysis presented in the Section 5 confirms that the gain-saturated SOAs can effectively mitigate atmospheric scintillation. For the simulated case with an input scintillation index of 0.50, the output scintillation index was reduced to 0.18, corresponding to a 64% reduction in intensity fluctuations. However, this mitigation is achieved at the cost of a 3.5 dB extinction ratio penalty. This trade-off defines the fundamental design boundary for saturation-based scintillation mitigation in FSO systems. Higher saturation output power reduces the extinction ratio penalty but provides less scintillation mitigation. An optimal operating point must therefore be selected that is based on the specific requirements of the FSO link.

6.1 Future Work

Current approaches to amplifier optimization in FSO systems typically address either amplifier parameters or signal-processing parameters in isolation (Bandele et al., 2016; Hong et al., 2019). The time-scale mismatch between amplifier dynamics (nanoseconds) and channel estimation (milliseconds) creates a hierarchical control problem (Bandele et al., 2016). Future optimization methods must account for most of non-convex goals and coupled parameter spaces along with real-time constraints (Ab-Rahman, 2014; Bandele et al., 2016). Analytical methods struggle with these limitations (Ab-Rahman, 2014). Numerical methods can solve non-convex problems but may be too computationally expensive for real-time adjustments (Bandele et al., 2016). Data-driven techniques such as using ML models that include channel state information could be used to fill the gap. However, there are currently very little FSO-specific data (Bandele et al., 2016; Xiao & Huang, 2008).

Future research will include the following (1) extending the numerical analysis of Section 5 to study the effects of modulation format and multi-channel crosstalk, (2) developing computational models that combine amplifier physics with channel estimation and adaptive signal processing (Bandele et al., 2016), and (3) investigating new designs of amplifiers, such as quantum dot SOAs (Xiao & Huang, 2008), for FSO applications. The development of integrated frameworks that jointly optimize amplifier operating parameters and signal-processing strategies under dynamic channel conditions remains an open research challenge (Bandele et al., 2016; Hong et al., 2019; D. Lee et al., 2021).

REFERENCES

1. Ab-Rahman, M. S. (2014). A review of the configuration and performance limitation parameters in optical amplifiers. *Optica Applicata, 44*(2), 251–266. https://doi.org/10.5277/oa140207
2. Agrawal, G. P. (2002). *Fiber-optic communication systems* (3rd ed.). Wiley.
3. Alimi, I. A., & Monteiro, P. P. (2024). Revolutionizing free-space optics: A survey of enabling technologies, challenges, trends, and prospects of beyond 5G free-space optical (FSO) communication systems. *Sensors, 24*(24), 8036. https://doi.org/10.3390/s24248036
4. Bandele, O. J., Desai, P., Woolfson, M. S., & Phillips, A. J. (2016). Saturation in cascaded optical amplifier free-space optical communication systems. *IET Optoelectronics, 10*(3), 71–79. https://doi.org/10.1049/iet-opt.2015.0083
5. Boluda-Ruiz, R., García-Zambrana, A., Castillo-Vázquez, C., Castillo-Vázquez, B., & Hranilovic, S. (2017). Outage performance of exponentiated Weibull FSO links under generalized pointing errors. *Journal of Lightwave Technology, 35*(9), 1605–1613. https://doi.org/10.1109/JLT.2017.2658956
6. Hong, Y. Q., Shin, W. H., & Han, S. K. (2019). Performance enhancement of gain saturated SOA based free space optical link using dual-wavelength transmission. *Optics Communications, 446*, 134–140. https://doi.org/10.1016/j.optcom.2019.04.063

ISSN: 2181-3337 | SCIENTISTS.UZ

7. Lee, D., Mai, V. V., & Kim, H. (2021). Mitigation of scintillation in FSOC using RSOA-based spectrum-sliced incoherent light. *IEEE Photonics Technology Letters, 33*(5), 227–230. https://doi.org/10.1109/LPT.2021.3053565
8. Lee, I. E., Ghassemlooy, Z., & Ng, W. P. (2012). Effects of aperture averaging and beam width on Gaussian free space optical links in the presence of atmospheric turbulence and pointing error. In *Proceedings of the 14th International Conference on Transparent Optical Networks (ICTON 2012)* (pp. 1–4). IEEE. https://doi.org/10.1109/ICTON.2012.6253851
9. Li, X., & Park, J. (2006). Time-domain simulation of channel crosstalk and inter-modulation distortion in gain-clamped semiconductor optical amplifiers. *Optics Communications, 263*(2), 219–228. https://doi.org/10.1016/j.optcom.2006.02.005
10. Liu, Y., Tan, X., Jia, J., Dong, B., Huang, C., Luo, P., Shi, J., Chi, N., & Zhang, J. (2023). A hybrid millimeter-wave and free-space-optics communication architecture with adaptive diversity combining and HARQ techniques. *Photonics, 10*(12), 1320. https://doi.org/10.3390/photonics10121320
11. Maho, A., Lévêque, S., Benazet, B., Duport, F., Van Dijk, F., Edmunds, J., Welch, M., Dorward, W., Sancho, A., Mesquita, D., Stampoulidis, L., & Sotom, M. (2025). Development and system evaluation of high-power semiconductor optical amplifiers for satellite-based free-space communications. In F. Bernard, N. Karafolas, P. Kubik, & K. Minoglou (Eds.), *International Conference on Space Optics—ICSO 2024* (Vol. 13699). SPIE. https://doi.org/10.1117/12.3075210
12. Merrouche, A., & Aissaoui, A. (2024). Enhancing performance in hybrid FSO/RF communication systems under atmospheric turbulence and pointing errors. *Journal of Optics, 53*(5), 4238–4248. https://doi.org/10.1007/s12596-023-01557-4
13. Miao, M., Chen, X.-Y., Yin, R., & Yuan, J. (2024). Performance analysis of free-space optical links over Lognormal-Shadow Rician (M̃) turbulence channels with generalized pointing errors. *IEEE Transactions on Vehicular Technology, 73*(12), 18688–18704. https://doi.org/10.1109/TVT.2024.3432914
14. Misra, G., Agarwal, A., & Mehta, S. N. (2024). A technical review on semiconductor optical amplifiers (SOAs) and their applications. *American Journal of Electrical and Electronic Engineering, 12*(1), 8–13. https://doi.org/10.12691/ajeee-12-1-2
15. Tang, H., Yang, C., Qin, L., Liang, L., Lei, Y., Jia, P., Chen, Y., Wang, Y., Song, Y., Qiu, C., Zheng, C., Li, X., Li, D., & Wang, L. (2023). A review of high-power semiconductor optical amplifiers in the 1550 nm band. *Sensors, 23*(17), 7326. https://doi.org/10.3390/s23177326
16. Xiao, J.-L., & Huang, Y.-Z. (2008). Numerical analysis of gain saturation, noise figure, and carrier distribution for quantum-dot semiconductor-optical amplifiers. *IEEE Journal of Quantum Electronics, 44*(5), 448–455. https://doi.org/10.1109/JQE.2007.916683
17. Zory, P. S. (Ed.). (1993). *Quantum well lasers*. Academic Press.

ISSN: 2181-3337 | SCIENTISTS.UZ VOLUME 5 ISSUE 9 | SEPTEMBER 2026

THERMAL STABILITY AND DECOMPOSITION STAGES OF A CORROSION-RESISTANT EPOXY-COAL TAR COMPOSITE COATING: TGA/DTA STUDY

Eshqobilov Jamshid[1], Abdukarimov Mirzokhid[2]

Doctoral student, Tashkent State Technical University, 2 Universitet Street, 100000 Tashkent, Uzbekistan. Corresponding author: jamshideshqobilov883@gmail.com[1]

DSc in Engineering, Associate Professor, Tashkent State Technical University, 2 Universitet Street, 100000 Tashkent, Uzbekistan[2]

DOI: 10.67620/sai.59a0006

ABSTRACT

A previously patented epoxy-coal tar coating was examined by thermogravimetric analysis (TGA) and differential thermal analysis (DTA) in order to clarify its thermal response and the sequence of mass-loss processes. The coating contains an ED-20 epoxy resin/coal tar binder, DTB-2 hardener, furfuryl alcohol distillation residue, wollastonite, andesite flour and saponified tall pitch. The thermogram indicates limited mass change below about 150 °C, followed by the dominant decomposition region between approximately 150 and 330 °C. The sample mass decreases from about 8.2 mg at the beginning of heating to roughly 2.6-2.7 mg after the main decomposition step. Between about 330 and 430 °C the TG curve becomes nearly horizontal, whereas above 430 °C a slower secondary mass loss continues to the end of the record. The remaining mass at about 700 °C is approximately 1.6-1.7 mg, corresponding to about 20% of the starting mass.

This value is close to the nominal 21 wt.% content of wollastonite and andesite flour in the formulation, which is consistent with a predominantly mineral residue; the possible contribution of carbonaceous material cannot be separated without information on the test atmosphere. The DTA trace contains overlapping thermal effects in the same temperature domain as the main TG drop. The results provide a thermal characterization of the patented coating and define the temperature interval in which major mass degradation becomes significant.

ACCEPTED

30.09.26

Keywords: *epoxy coating, coal tar, corrosion protection, thermogravimetric analysis, differential thermal analysis, wollastonite, andesite flour.*

CC BY

Introduction

Epoxy binders are widely used in protective coatings because they combine strong adhesion with low permeability and chemical resistance. Their long-term corrosion performance, however, is governed not only by the cured polymer network but also by fillers, modifiers, residual low-molecular species and defects formed during curing (Verma et al., 2020). Thermal analysis is useful in this context because a mass-loss curve separates low-temperature release of volatile species from the principal degradation of the network, while the residual mass provides information about non-volatile constituents (Brown, 2001).

Recent studies of modified epoxy coatings have shown that changes in cross-link density and inorganic filler content can shift the degradation profile and alter the high-temperature residue (Adnan et al., 2026; Farrer et al., 2025; Wu et al., 2025; Wu et al., 2026; Xia et al., 2024; Zhao et al., 2024).

The coating considered here was developed earlier as a corrosion-resistant composition for metal surfaces and is protected by Uzbekistan patent UZ IAP 8558 (Eshqobilov et al., 2026). Its formulation combines an ED-20 epoxy resin/coal tar binder with DTB-2 hardener, furfuryl alcohol distillation residue, wollastonite, andesite flour and saponified tall pitch. The patent reports high adhesion and resistance to water exposure, cathodic disbonding and penetration (Eshqobilov et al., 2026). Those previously reported data are not treated as new measurements in this paper; they are used only to identify the material whose thermal behavior is examined.

The present work focuses on a different question: how the patented coating loses mass during heating, which temperature intervals dominate this process, and how the final residue relates to the formulation. The aim was therefore to interpret the available combined TGA/DTA thermogram without extending the analysis beyond the information actually contained in the experimental record. Particular attention was given to the main degradation interval, the high-temperature residue and the limitations imposed by the absence of the original instrument metadata.

MATERIALS AND METHODS. The object of investigation was the optimized formulation described in patent UZ IAP 8558 (Eshqobilov et al., 2026). The component ratio used for the thermal specimen is summarized in Table 1. The 60 wt.% binder fraction consisted of ED-20 epoxy resin and coal tar at a mass ratio of 1:0.4. The mineral fraction was formed by wollastonite (13 wt.%) and andesite flour (8 wt.%), giving a nominal inorganic filler content of 21 wt.%.

Table 1

Composition of the Coating Examined by TGA/DTA

Component	Content, wt.%
ED-20 epoxy resin/coal tar mixture (mass ratio 1:0.4)	60
DTB-2 hardener	7
Furfuryl alcohol distillation residue	5
Wollastonite	13
Andesite flour	8
Saponified tall pitch, grade B	7

According to the patented preparation procedure, the ED-20/coal tar binder was mixed at about 80 °C. The modifier, andesite flour, wollastonite and saponified tall pitch were introduced after cooling to about 50 °C, and the compound was homogenized before addition of DTB-2 immediately prior to use (Eshqobilov et al., 2026). These processing data are cited from the patent rather than presented as a new experiment.

Thermal analysis was evaluated from the combined TGA/DTA plot supplied for the coating sample (Figure 1). The initial sample mass read from the graph is approximately 8.2 mg. The blue trace represents mass change (TGA, mg) and the red trace represents the differential thermal signal (DTA, μV). The original export does not state the instrument model, heating rate, purge atmosphere, gas flow, crucible material, reference material or calibration procedure. Because these parameters materially affect onset temperatures and the direction of DTA effects, the present analysis uses approximate temperature intervals and visually estimated mass fractions only. No kinetic constants, activation energies, enthalpies or formal

ISSN: 2181-3337 | SCIENTISTS.UZ

T5/T10 values are calculated. This restriction follows established guidance that kinetic interpretation requires well-defined experimental conditions and suitable datasets (Vyazovkin et al., 2011).

RESULTS.

The TG curve is not characterized by a single abrupt event. Instead, four practical temperature regions can be distinguished from the plotted mass trend. Below about 150 °C, the mass remains close to its initial value and decreases only slightly. This part of the curve is compatible with removal of physically retained moisture or a small amount of volatile material, but the graph alone does not permit identification of individual species. The observation is relevant because retained volatiles are known to influence the low-temperature thermal response of cured epoxy-amine coatings (Farrer et al., 2025).

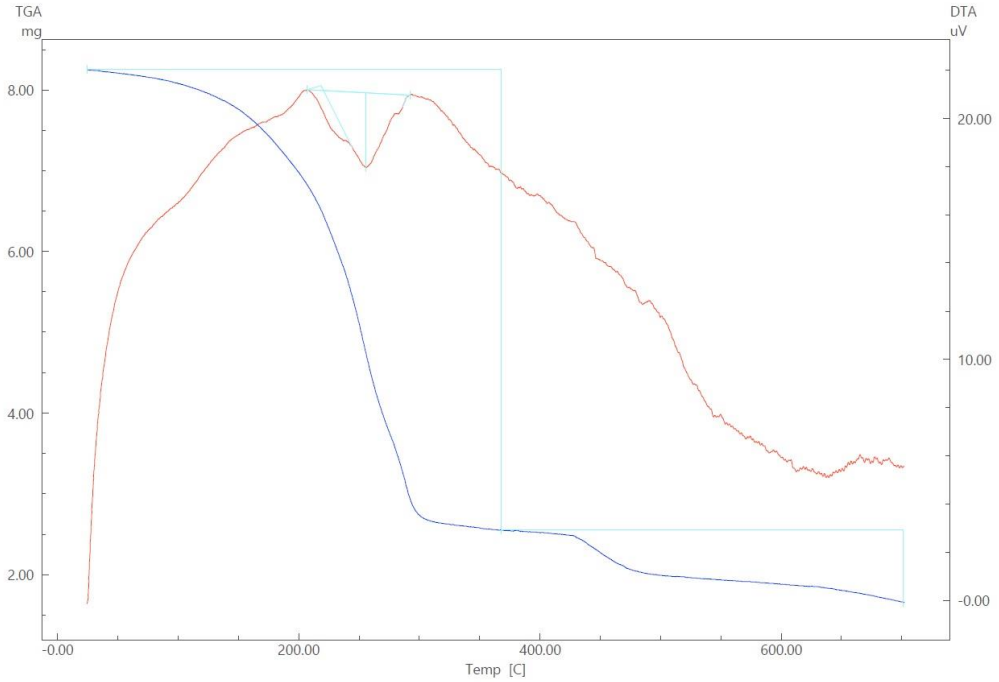


Figure 1. Combined TGA/DTA thermogram of the epoxy-coal tar composite coating (experimental graph supplied by the authors)

The dominant mass-loss region extends from roughly 150 to 330 °C. Over this interval the mass falls from approximately 7.8-8.0 mg to about 2.6-2.7 mg. In other words, only about one-third of the starting mass remains after the principal degradation step. Because the formulation contains coal tar, a furfuryl-derived modifier and a cured epoxy network, several organic processes are expected to overlap in this temperature range; the available DTA trace confirms that the event is not thermally simple.

Table 2

Thermal Regions Estimated From the Supplied Thermogram

Approx. temperature interval	Observed behavior	Evidence-based interpretation
25-150 °C	Small mass decrease; TGA remains near the initial mass	Release of a limited amount of moisture and/or low-boiling material is possible.
150-330 °C	Steepest TGA decrease; mass falls to about 2.6-2.7 mg	Principal degradation of the organic part of the coating; several reactions overlap.
330-430 °C	Low-slope / near-plateau region around 2.5-2.6 mg	Temporary stabilization of the remaining condensed and mineral-rich fraction.

ISSN: 2181-3337 | SCIENTISTS.UZ

Approx. temperature interval	Observed behavior	Evidence-based interpretation
430-700 °C	Slow secondary mass decrease; final residue about 1.6-1.7 mg (~20%)	Further transformation of the remaining organic fraction; residue is consistent with predominantly mineral matter.

From approximately 330 to 430 °C, the TG trace becomes much flatter and remains near 2.5-2.6 mg. A further gradual mass decrease begins above about 430 °C and continues to the end of the plot. At approximately 700 °C the remaining mass is about 1.6-1.7 mg, equivalent to roughly 20% of the starting sample mass. The nominal mineral fraction of the formulation is 21 wt.% (13 wt.% wollastonite plus 8 wt.% andesite flour). The close numerical agreement between these two values is consistent with a residue dominated by thermally persistent mineral matter. However, the unknown test atmosphere prevents a quantitative separation of inorganic residue from any possible carbonaceous contribution.

The DTA trace contains a broad high-temperature response rather than isolated sharp peaks. An initial broad feature develops near 180-210 °C, followed by a change in direction around approximately 240-270 °C and another broad feature near 290-320 °C. These effects overlap the main TG mass-loss region. Since the plot does not specify whether upward deflection is endothermic or exothermic, assigning them to specific reactions would be speculative. They are therefore described here only as thermal events accompanying the principal decomposition process.

DISCUSSION. The most useful quantitative result from the present thermogram is the separation between the low-temperature region and the major mass-loss interval. The coating shows no large TG drop below about 150 °C, whereas the majority of the organic mass is lost between approximately 150 and 330 °C. This does not define a safe service-temperature limit. Glass transition, softening, adhesion loss or stress relaxation can occur before a pronounced TGA mass change. Consequently, the TG curve should be interpreted as a decomposition profile rather than as a direct operating-temperature specification.

The onset of major mass loss in the present graph appears lower than values reported for some recently engineered epoxy systems. For example, an organic-inorganic hybrid epoxy coating reported by Zhao et al. (2024) showed a 5% mass-loss temperature increasing from 327 to 372 °C after silane-based modification. Wu et al. (2026) reported T5 values of about 275-288 °C for ZrO2-modified epoxy coatings, while polyimide-modified epoxy coatings with inorganic fillers retained approximately 90% of their mass near 270 °C (Wu et al., 2025). These values should not be used to rank the current coating directly, because heating rate, atmosphere, formulation and the criterion used to define onset differ among studies. The comparison nevertheless shows that the lower-temperature fraction in the epoxy-coal tar formulation deserves attention and may reflect the presence of coal-tar constituents, furfuryl-derived material or other low-molecular components.

The final residue is particularly informative. Modern filled epoxy coatings often display higher residue when non-volatile inorganic fillers are present (Wu et al., 2025; Wu et al., 2026). In the present formulation, the nominal 21 wt.% mineral fraction is remarkably close to the approximately 20% residue estimated at 700 °C. This supports, without proving, the interpretation that wollastonite and andesite flour account for most of the final non-volatile material. If the experiment was performed under inert gas, some char from the organic binder may also remain; if it was performed in an oxidative atmosphere, that contribution would be smaller. The atmosphere therefore needs to be reported in any future repeated measurement before carbonization mechanisms are discussed quantitatively.

The role of mineral filler in protective epoxy coatings extends beyond its contribution to residual mass. Inorganic particles can increase diffusion path length and reduce the effective fraction of permeable

ISSN: 2181-3337 | SCIENTISTS.UZ

polymer, although the benefit depends strongly on particle dispersion and interfacial compatibility (Verma et al., 2020; Wu et al., 2026; Xia et al., 2024). The earlier patent reports for the same formulation include a pull-off adhesion of 14.5 MPa, an 11% decrease in adhesion after 1000 h water exposure, cathodic disbonding of 1.20 cm^2, penetration of 0.07 mm and tensile strength of 42.1 MPa (Eshqobilov et al., 2026). Those values were obtained previously and are cited here only as context. The current TGA/DTA data add a different dimension: they show that the material retains a substantial non-volatile fraction after the main organic decomposition step.

A limitation of the present study is that only the graphical thermogram was available, without raw numerical data or instrument metadata. This prevents calculation of derivative TG peak temperatures, statistically reproducible onset values, reaction kinetics or mass-loss uncertainty. A follow-up study should repeat TGA under a stated atmosphere and heating rate, preferably at more than one heating program if kinetic analysis is intended (Vyazovkin et al., 2011). A DTG or DSC trace would also help distinguish overlapping transitions that cannot be resolved reliably from the present DTA plot.

CONCLUSION. The TGA/DTA thermogram of the patented epoxy-coal tar composite coating reveals a multistage thermal response. Only a limited mass change is visible below about 150 °C, while the principal degradation occurs between approximately 150 and 330 °C. A low-slope region follows, and a slower secondary mass loss continues above about 430 °C. The residue near 700 °C is approximately 20% of the initial mass, close to the 21 wt.% nominal content of wollastonite and andesite flour. This agreement is consistent with a residue dominated by mineral components, although the contribution of carbonaceous material cannot be determined without the test atmosphere. The DTA curve confirms that several thermal events overlap with the main mass-loss region, but their endothermic or exothermic nature cannot be assigned from the supplied plot. The analysis therefore provides a conservative thermal characterization of the coating and identifies the temperature range in which its organic matrix undergoes substantial decomposition.

CONFLICT OF INTEREST

The authors declare no conflict of interest related to this work.

REFERENCES

1. Adnan, S. N. A., Kahar, N. E. A., Sobari, M. S., Mohamed, S. H., Chen, L. J., Lee, E., Pargi, M. N. F., & Musa, M. S. (2026). Effect of epoxy content on the corrosion properties of waterborne epoxy-acrylate coating. *Journal of Coatings Technology and Research*, *23*(2), 883–898. https://doi.org/10.1007/s11998-025-01175-8
2. Brown, M. E. (2001). *Introduction to thermal analysis: Techniques and applications* (2nd ed.). Kluwer Academic Publishers.
3. Eshqobilov, J. H., Abdukarimov, M. M., Yodgorov, N., & Nurkulov, F. N. (2026). *Polymer composition for obtaining a corrosion-resistant coating* (Uzbekistan Patent No. UZ IAP 8558). Republic of Uzbekistan.
4. Farrer, N., Intaphan, W., Lyon, S., Edwards, W., Beaumont, D., & Morsch, S. (2025). Insights into volatile presence within epoxy amine coatings using nano-thermal analysis. *Progress in Organic Coatings*, *207*, Article 109406. https://doi.org/10.1016/j.porgcoat.2025.109406
5. Verma, C., Olasunkanmi, L. O., Akpan, E. D., Quraishi, M. A., Dagdag, O., El Gouri, M., Sherif, E. S. M., & Ebenso, E. E. (2020). Epoxy resins as anticorrosive polymeric materials: A review. *Reactive and Functional Polymers*, *156*, Article 104741. https://doi.org/10.1016/j.reactfunctpolym.2020.104741
6. Vyazovkin, S., Burnham, A. K., Criado, J. M., Pérez-Maqueda, L. A., Popescu, C., & Sbirrazzuoli, N. (2011). ICTAC Kinetics Committee recommendations for performing kinetic computations on thermal analysis data. *Thermochimica Acta*, *520*(1–2), 1–19. https://doi.org/10.1016/j.tca.2011.03.034

ISSN: 2181-3337 | SCIENTISTS.UZ

7. Wu, M., Cao, G., & Xiao, Z. (2025). Polyimide-modified epoxy coatings reinforced with functional fillers for enhanced thermal stability and corrosion resistance. *Advanced Composites and Hybrid Materials*, *8*, Article 172. https://doi.org/10.1007/s42114-025-01265-6
8. Wu, Y., Yang, Q., Zhang, H., Zhou, Y., Guo, H., Wang, Z., & Li, G. (2026). Enhancing hydrophobicity and corrosion resistance of epoxy resin coatings using KH570-ZrO2 nanoparticles. *Polymer Testing*, *154*, Article 109070. https://doi.org/10.1016/j.polymertesting.2025.109070
9. Xia, Y., Tong, L., Feng, X., Zhang, S., Xiang, H., He, Y., & Liu, X. (2024). An investigation on the mechanical and corrosion protection properties of poly(arylene ether nitrile) reinforced epoxy coating. *Progress in Organic Coatings*, *192*, Article 108463. https://doi.org/10.1016/j.porgcoat.2024.108463
10. Zhao, H., Liang, X., & Gao, Y. (2024). Organic-inorganic hybrid epoxy resin coating with high thermal stability and hydrophobicity for corrosion protection prepared by (3-aminopropyl) triethoxysilane as a bridging agent. *Materials Today Communications*, *39*, Article 108950. https://doi.org/10.1016/j.mtcomm.2024.108950

ISSN: 2181-3337 | SCIENTISTS.UZ VOLUME 5 ISSUE 9 | SEPTEMBER 2026

THE EFFECT OF FUJIMIN LIQUID FERTILIZER ON INCREASING SOIL FERTILITY UNDER EXTREME CLIMATIC CONDITIONS

Kattaeva Gulnoza[1], Ismonov Abduvahob[2], Mamajanova Uktamxon[3], Dusaliev Alijon[4]

PhD, Senior Researcher, Scientific Research Institute of Soil Science and Agrochemistry, Tashkent[1]
Candidate of Biological Sciences, Senior Researcher, Scientific Research Institute of Soil Science and Agrochemistry, Tashkent[2]
PhD, Senior Researcher, Scientific Research Institute of Soil Science and Agrochemistry, Tashkent[3]
PhD, Scientific Research Institute of Soil Science and Agrochemistry, Tashkent[4]

DOI: 10.67620/sai.59a0007

ABSTRACT

This study evaluated the effects of Fujimin, a fulvic-acid-based liquid organic fertilizer, on the fertility of irrigated takyr-meadow soils under the extreme soil and climatic conditions of the Surkhandarya Region, Uzbekistan. Field treatments compared a conventional mineral fertilizer regime with a 20% reduction in mineral fertilizer and several liquid organic fertilizer treatments, including Fujimin at 4 and 5 L/ha. Changes in humus and mobile nitrogen, phosphorus, and potassium were assessed in the 0-30 and 30-50 cm soil layers. The 5 L/ha Fujimin treatment produced the largest annual increase in humus among the tested treatments, with gains of 0.0825% in the 0-30 cm layer and 0.067% in the 30-50 cm layer. In the surface layer, nitrate nitrogen reached 24.5 mg/kg and labile phosphorus reached 26.8 mg/kg, representing increases of 11.6 and 10.0 mg/kg, respectively. Mobile potassium also increased relative to the reduced-mineral-fertilizer baseline. The results indicate that applying Fujimin at 4-5 L/ha together with a 20% reduction in mineral fertilizer can improve soil nutrient status and help maintain soil fertility under high-temperature, drought-prone, and saline conditions. These findings support the use of fulvic-acid-based inputs as a resource-conserving component of cotton production in environmentally stressful regions.

ACCEPTED

05.10.26

Keywords: *Fujimin, fulvic acid, takyr-meadow soil, soil fertility, salinity, cotton.*

CC BY

Introduction

In Uzbekistan, the rational use of agricultural land, environmental sustainability, and improvement of soil fertility are priority policy areas. Presidential Resolution No. PQ-71 of February 13, 2024, and Cabinet of Ministers Resolution No. 97 of February 20, 2024, establish measures to combat agricultural land degradation, increase soil humus content, and improve soil fertility, including the use of Fujimin technology in demonstration areas (Cabinet of Ministers of the Republic of Uzbekistan, 2024; President of the Republic of Uzbekistan, 2024). These priorities emphasize the prevention of dehumification and degradation, the enrichment of soil organic matter, and the development of mechanisms for increasing soil fertility and crop yields. Accordingly, this study assesses changes in the properties of irrigated takyr-meadow soils under extreme soil and climatic conditions.

Fujimin is a liquid organic fertilizer based on fulvic acid. According to the product information, the concentrate is diluted with water and applied by spraying, and its proposed advantage is the chelation of nutrients that can facilitate plant uptake of nitrogen, phosphorus, potassium, iron, magnesium, and other elements (AgroBio, n.d.).

Organic liquid fertilizers can influence soil organic matter and the availability of nitrogen, phosphorus, and potassium, all of which are important for crop nutrition and development. Research on humic and fulvic substances has examined their composition, soil functions, and interactions with plant nutrition (AgroBio, n.d.; Boynazarov et al., 2023; Kononova, 1984; Orlov, 1990, 1997; Orlov et al., 1996; Preston, 1996; Tyurin, 1965; Wilson, 1987).

The Surkhandarya Region is characterized by very hot and dry conditions. In Termez, high land-surface temperatures occur during summer, and in the Djarkurgan District the hot southwesterly garm-sil (Afghan wind) can intensify heat and moisture stress in irrigated cropping systems. The study area is also affected by salt accumulation, so drought, heat, and salinity may act together as constraints on plant growth and soil functioning.

Foundational research on soil organic matter has established its importance for soil fertility and for the physical and chemical properties that regulate nutrient availability. Relevant work includes studies of soil organic matter, plant nutrition and soil formation, and nuclear magnetic resonance approaches to soil organic matter characterization (Kononova, 1984; Ponomareva, 1972; Preston, 1996; Tyurin, 1965; Wilson, 1987).

Research Methods

Soil investigations used genetic-geographical, lithological-geomorphological, chemical-analytical, profile, field, desktop, and cartographic methods. The procedures followed established soil-survey and analytical guidance used in Uzbekistan and standard chemical analysis methods (Arinushkina, 1970; Qo'ziev et al., 2013; UzPITI, 1963).

Research Objective

The objective was to increase plant resistance to climate-related stress and improve soil fertility through the use of Fujimin liquid fertilizer based on fulvic acid.

Results and Discussion

Soil fertility depends strongly on humus and nutrient availability, and loss of soil moisture can accelerate deterioration of these components and constrain crop growth. In 2023, fine-staple cotton was grown in the Djarkurgan, Angor, Sherabad, and Termez districts of the Surkhandarya Region over an area of approximately 60,000 ha despite extreme soil and climatic conditions. During field monitoring in Sherabad District, a soil-surface temperature of 68°C was observed during the flowering and budding periods.

Liquid organic fertilizers can improve soil structure and water retention. The investigated soils are affected primarily by sulfate and chloride-sulfate salinization. As salt concentration increases, osmotic pressure in the soil solution rises and can restrict root water uptake and plant growth. In this experiment, Fujimin and humate-based treatments were evaluated as approaches for mitigating these stress factors. Biofertilizer use is also consistent with regional resource-efficient cotton production recommendations for extreme climatic conditions (Tadjiyev et al., 2017, 2022).

Table 1

Experimental Design

Option 1	Option 2	Option 3	Option 4	Option 5	Option 6	Option 7	Option 8
N200P140K100 Ratio 1:0.7:0.5 - control	N160P112K80 Ratio 1:0.7:0.5 Ground, mineral fertilizers have been reduced by 20 percent	Ground + 10 L/ha liquid potassium humate fertilizer	Ground + 5 L/ha Entogumin	Ground + 5 L/ha Gumimax -R	Ground + 4 L/ha Fujiminbio fertilizer	Ground + 5 L/ha Fujiminbio fertilizer	Microbiological preparation

ISSN: 2181-3337 | SCIENTISTS.UZ

Table 2

Preliminary Analysis Results for Takyr-Meadow Soils Prior to Land Leveling

No.	Depth (cm)	Humus (%)	N-NO3	P2O5	K2O	CO2 (%)	pH	EC2
2K	0-34	0.844	16.40	19.8	105	8.10	7.55	0.73
2K	34-52	0.798	9.72	18.0	84	9.06	7.66	0.54
2K	52-84	0.757	7.87	15.0	64	10.17	7.81	0.37
2K	84-115	0.687	5.03	10.2	45	10.61	7.79	0.23
2K	115-150	0.507	2.80	6.4	41	10.99	7.88	0.22

The analyses demonstrated changes in nutrient and humus content in the topsoil (0-30 cm) and subsoil (30-50 cm) of the irrigated takyr-meadow soils (Table 3).

In the control (Option 1), humus content in the 0-30 cm layer was 1.209%, whereas in the reduced-mineral-fertilizer treatment (Option 2) it was 1.095%. Treatments receiving liquid organic fertilizers showed positive changes. In Option 7 (reduced mineral fertilizer + 5 L/ha Fujimin), the annual increase in humus was 0.0825% in the 0-30 cm layer and 0.067% in the 30-50 cm layer, indicating a favorable response of soil organic matter.

Mobile nitrogen was also responsive to treatment. In the control, N-NO3 content in the 0-30 cm layer was 11.5 mg/kg. In Options 6 and 7, which received 4 and 5 L/ha Fujimin, respectively, mobile nitrogen reached 23.9 and 24.5 mg/kg, with annual increases of 9.8 and 11.6 mg/kg, respectively.

Phosphorus and potassium availability also changed across treatments. Labile P2O5 in the 0-30 cm layer was 17.8 mg/kg in the control and 26.8 mg/kg in Option 7, an annual increase of 10.0 mg/kg. Mobile K2O reached 211 mg/kg in Option 3 (potassium humate) and 148 mg/kg in Option 7, corresponding to increases of 94.0 and 57.0 mg/kg, respectively. Nutrient stocks were comparatively more stable in the 30-50 cm layer (Table 3).

Table 3

Difference in Nutrient Content Throughout the Year

Option	Depth (cm)	Humus (%)	Annual difference (+)	Mobile nutrients (mg/kg)					
				N-NO3	Annual difference (+)	P2O5	Annual difference (+)	K2O	Annual difference (+)
B-1	0-30	1.209	0.0045	11.5	0.7	17.8	2.2	188	20.0
B-1	30-50	1.005	0.004	8	1.5	11	1.6	156	8.0
B-2	0-30	1.095	0.001	14	0.3	19.8	1.3	141	7.0
B-2	30-50	0.929	0.0005	10.5	0.7	13.4	0.8	124	4.0
B-3	0-30	1.055	0.0095	15.9	3.0	20.8	3.9	211	94.0
B-3	30-50	0.955	0.0075	9.5	1.9	13.6	3.4	182	84.0
B-4	0-30	1.089	0.0095	15.5	3.1	16.2	3.8	156	29.0
B-4	30-50	0.989	0.0495	8.9	2.6	14.2	4.8	135	27.0
B-5	0-30	0.85	0.0375	17.5	5.0	20.6	1.8	166	46.0
B-5	30-50	0.595	0.0275	13.5	3.8	14.8	1.6	125	24.0
B-6	0-30	1.123	0.0515	23.9	9.8	23.6	6.8	152	47.0
B-6	30-50	0.878	0.032	18.5	8.5	17.2	6.6	105	19.0
B-7	0-30	0.975	0.0825	24.5	11.6	26.8	10.0	148	57.0
B-7	30-50	0.844	0.067	18.5	9.0	18.4	7.0	115	34.0
B-8	0-30	0.920	0.054	18.5	7.6	19.8	4.0	205	38.0
B-8	30-50	0.804	0.0195	12.5	3.6	13.2	3.6	115	18.0

Conclusion

The findings show that applying Fujimin at 4-5 L/ha together with a 20% reduction in mineral fertilizer improved the measured agrochemical indicators and helped maintain soil fertility under extreme conditions.

Liquid organic fertilizers can serve as a resource-conserving tool in cotton production under climate-related stress. Fulvic-acid-based preparations are associated with nutrient chelation and may

ISSN: 2181-3337 | SCIENTISTS.UZ

support nutrient availability and crop development; these functions are consistent with regional cotton-production recommendations and earlier work on organic amendments (Avliyokulov & Tadjiyev, 1992; Avliyokulov et al., 2008; Boltaev et al., 2008; Jurayev & Tojiyev, 1992; Rakhmatov et al., 2005; Tadjiyev et al., 2006).

Under the saline and high-temperature conditions observed in the study area, the Fujimin treatment was associated with improved nutrient status and favorable conditions for crop-component development. Integrated crop-protection and management recommendations for the Surkhandarya Region likewise emphasize the importance of managing multiple environmental and biological stresses (Khasanov et al., 2005).

Overall, integrating Fujimin into resource-conserving cotton production may contribute to maintaining soil fertility and reducing degradation risks under stressful environmental conditions. Recent work on soil degradation in Uzbekistan further underscores the importance of monitoring soil physical and chemical changes under changing hydrological and environmental conditions (Jabbarov et al., 2025).

REFERENCES

1. AgroBio. (n.d.). *Fulvic acids: Structure, composition and formation of fulvic acids*. https://agro.bio/ru/fulvokisloty-stroyeniye-sostav-obrazovaniye
2. Arinushkina, E. V. (1970). *Manual of chemical analysis of soils* (2nd ed.). Moscow University Press.
3. Avliyokulov, A., & Tadjiyev, M. (1992). *Recommendations on agrotechnics for growing cotton cultivated in the Surkhandarya Region and achieving high yields*. Jaykhun Publishing House.
4. Avliyokulov, N. E., Tadjiyev, M., et al. (2008). *Recommendations on agrotechnical practices for obtaining high yields of Termes-49 cotton producing type I fiber*.
5. Boltaev, S. M., Tadjiyev, M., et al. (2008). *Recommendations on the effective use of bentonite-manure compost from non-traditional agricultural wastes in cotton production*.
6. Boynazarov, B., Djumaniyazova, G., & Berdiev, T. (2023). Use of humic organic matter and rhizobacteria in the cultivation of winter wheat in areas polluted with heavy metals. *BIO Web of Conferences, 78*, 07005. https://doi.org/10.1051/bioconf/20237807005
7. Cabinet of Ministers of the Republic of Uzbekistan. (2024, February 20). *On additional measures to increase the fertility of agricultural lands (Resolution No. 97)*. LexUZ. https://www.lex.uz/uz/acts/-6809142
8. Jabbarov, Z., Abdullaev, Sh., Rakhmatullaeva, G., Abdurakhmonov, N., Ismonov, A., Kalandarov, N., Yuldashev, I., Pulatov, M., Mamajanova, O'., & Djabborov, Sh. (2025). Degradation of soils around the Kattakurgan Reservoir and its impact on soil properties. *Journal of Degraded and Mining Lands Management, 12*(5), 8957-8967. https://doi.org/10.15243/jdmlm.2025.125.8957
9. Jurayev, B., & Tojiyev, M. (1992). *Cotton cultivation and seed production in Surkhandarya*.
10. Khasanov, B. O., Khujayev, Sh. T., & Khamroyev, A. Sh. (2005). *Recommendations on protecting cotton and grain crops from pests, diseases, and weeds in the Surkhandarya Region*.
11. Kononova, M. M. (1984). Organic matter in soils and soil fertility. *Pochvovedenie, 8*, 6-20.
12. Orlov, D. S. (1990). *Humic acids in soils and a general theory of humification*. Moscow State University Press.
13. Orlov, D. S. (1997). Humic substances in the biosphere. *Soros Educational Journal, 2*, 56-63.
14. Orlov, D. S., Biryukova, O. N., & Sukhanova, N. I. (1996). *Organic matter in the soils of Russia and the Russian Federation*. Nauka.
15. Ponomareva, V. V. (1972). Conditions for the water and mineral nutrition of plants, vegetation types and soil formation. In *Geography, genesis and fertility of soils* (pp. 24-57).

16. President of the Republic of Uzbekistan. (2024, February 13). *On additional measures to combat the degradation of agricultural land and support increasing soil humus content and fertility (Resolution No. PQ-71)*. LexUZ. https://lex.uz/en/acts/-6798455
17. Preston, C. M. (1996). Applications of NMR to soil organic matter analysis: History and prospects. *Soil Science, 161*(3), 144-166. https://doi.org/10.1097/00010694-199603000-00002
18. Qo'ziev, R., Abdurakhmonov, N. Yu., Ismonov, A. J., et al. (2013). *Instructions for conducting a soil survey and compiling soil maps for maintaining the state land cadastre*. Tashkent.
19. Rakhmatov, I., Choriyev, Sh., Jumayev, Sh., Buriyev, Ya., & Rajaboyev, T. (2005). *Recommendations for farming enterprises for cotton care*.
20. Tadjiyev, M., Abduolimov, Sh., Tadjiyev, K. M., Ochildiyev, N. N., & Abdumiminov, Sh. (2022). *Recommendations on developing resource-efficient technologies for growing an early cotton crop under extreme climatic conditions in the Surkhandarya Region*.
21. Tadjiyev, M., Kurbonova, G., Tojiyev, K., & Khujmanov, O. (2006). The effect of nutrient and water levels on the growth, development, and yield of cotton. In *Proceedings of the Republican Scientific and Practical Conference* (pp. 158-160).
22. Tadjiyev, M., Ochildiyev, N. N., et al. (2017). *Recommendations on agritechnology for producing high-yield, high-quality cotton and other crops in the Surkhandarya Region*.
23. Tyurin, I. V. (1965). *Soil organic matter and its role in fertility*. Nauka.
24. UzPITI. (1963). *Agrochemical, agrophysical and microbiological studies of soils and plants*.
25. Wilson, M. A. (1987). *NMR techniques and applications in geochemistry and soil chemistry*. Pergamon Press.

ISSN: 2181-3337 | SCIENTISTS.UZ

ISSN: 2181-3337 | SCIENTISTS.UZ VOLUME 5 ISSUE 9 | SEPTEMBER 2026

ASSESSMENT OF RADIONUCLIDE PARAMETERS IN SOILS OF RECLAIMED AREAS BASED ON A MATHEMATICAL MODEL

Qilichev Xudoynazar[1], Qurbonov Jaloliddin[2], Farmonov Shavkat[3], Allaberganova Gulchehra[4], Yorqulov Behzod[4], Muzafarov Amrullo[4]

PhD, Senior Researcher, Scientific Research Institute of Soil Science and Agrochemistry, Tashkent[1]
Candidate of Biological Sciences, Senior Researcher, Scientific Research Institute of Soil Science and Agrochemistry, Tashkent[2]
PhD, Senior Researcher, Scientific Research Institute of Soil Science and Agrochemistry, Tashkent[3]
PhD, Scientific Research Institute of Soil Science and Agrochemistry, Tashkent[4]

DOI: 10.67620/sai.59a0008

ABSTRACT

This article investigates the depth-dependent distribution of uranium and radium radionuclides in soils of reclaimed areas. The main objective of the study is to determine changes in the specific activities of ^{238}U and ^{226}Ra in soil layers and to evaluate differences in radionuclide distribution on the basis of the $^{226}Ra/^{238}U$ radioactive-equilibrium ratio. Data obtained at depths of 0.25, 0.50, 0.75, and 1.00 m were analyzed for each of the P1 and P2 sampling points. According to the results, the ^{238}U activity decreased from 1844.8 to 408 Bq/kg at P1 and from 3160 to 610 Bq/kg at P2. In contrast, the ^{226}Ra activity increased from 521 to 1400 Bq/kg at P1 and from 512 to 3240 Bq/kg at P2. The $^{226}Ra/^{238}U$ ratio changed from 0.28 to 3.43 at P1 and from 0.16 to 5.31 at P2. To interpret the observed vertical changes, the possible effects of soil-water interaction, vertical water infiltration, sorption-desorption processes, and geochemical conditions are discussed. The results may provide a basis for assessing the vertical distribution of radionuclides in reclaimed areas and for subsequent mathematical modeling of migration processes.

ACCEPTED

05.10.26

Keywords: *reclamation, soil, ^{238}U, ^{226}Ra, specific activity, radionuclides, depth distribution, $^{226}Ra/^{238}U$ ratio, water infiltration, radionuclide migration, sorption, desorption.*

CC BY

Introduction

The distribution and redistribution of radionuclides in environmental components within technogenically altered areas formed during uranium mining and processing are important scientific issues from the standpoint of environmental safety. In particular, studying the vertical distribution of uranium-series radionuclides, including ^{238}U and ^{226}Ra, in the soils of reclaimed areas makes it possible to evaluate their movement along the soil profile. The distribution of radionuclides in soil may be affected by their physicochemical properties, the mineralogical composition and moisture content of the soil, the degree of binding to particles, sorption and desorption processes, as well as vertical water infiltration. Therefore, it is important not to restrict the assessment to radionuclide contents in the surface layer alone, but also to analyze their specific activities at different depths. The ratio between ^{238}U and ^{226}Ra can be used as an additional indicator for analyzing the state of radioactive equilibrium between radionuclides and redistribution processes within the soil profile. Under conditions close to natural radioactive equilibrium, uranium and radium activities are expected to be similar; therefore, a pronounced depth-dependent change

in their ratio may indicate differences in radionuclide mobility or redistribution processes in the soil environment.

Foreign studies have also examined the vertical distribution of ^{238}U and ^{226}Ra in soils of uranium-mining areas. For example, Jiang et al. analyzed the contents of ^{238}U and ^{226}Ra in soil profiles to a depth of 0-1.0 m around a uranium-mining area and evaluated both their depth-dependent variation and the $^{226}Ra/^{238}U$ ratio.

In the present study, the specific activities of ^{238}U and ^{226}Ra at different depths in soils of a reclaimed area, together with their $^{226}Ra/^{238}U$ ratio, are analyzed. The main emphasis is placed on identifying the characteristics of vertical radionuclide distribution, evaluating the depth-dependent variation of their ratio, and discussing the observed changes in terms of water infiltration, sorption-desorption, and geochemical processes in soil.

Literature review

Issues related to the distribution and migration of radionuclides in soil and the assessment of their environmental risk in uranium-mining and processing areas have been investigated in a number of foreign studies. These studies have mainly focused on the distribution of ^{238}U and ^{226}Ra along soil profiles, the state of radioactive equilibrium between them, and radionuclide redistribution processes in the environment.

Jiang W., Gao B., Zhang H.Y. et al. investigated the distribution characteristics of ^{238}U and ^{226}Ra in soils surrounding a uranium-mining area. Soil samples were collected from the 0-0.2, 0.2-0.4, 0.4-0.6, 0.6-0.8, and 0.8-1.0 m layers. In addition to statistical analysis of vertical radionuclide distribution, the authors used the $^{226}Ra/^{238}U$ ratio to assess the relationship between radionuclides within the soil profile. The study identified changes in the contents of ^{238}U and ^{226}Ra with soil depth.

The $^{226}Ra/^{238}U$ ratio was also considered an important indicator in that study. According to the authors, under radioactive-equilibrium conditions this ratio may be approximately equal to one. The reported values were 0.82-1.11 in the 0.4-0.6 m layer and 0.60-1.15 in the 0.8-1.0 m layer. Overall, the depth-dependent variation of the $^{226}Ra/^{238}U$ ratio was used to characterize radionuclide redistribution within the soil profile.

The vertical distribution of radionuclides in uranium-bearing areas has also been investigated in other studies. In particular, the distribution of natural radionuclides and deviations from radioactive equilibrium in the uranium series have been examined in soil profiles from uranium-mineralized areas of Spain. Such studies show that the state of radionuclides in soil can be assessed not only from their total concentrations, but also from their mutual ratios and depth-dependent changes.

Water movement may also influence the redistribution of radionuclides among soil layers in uranium tailings and technogenically altered areas. Water infiltrating into soil may transport radionuclides vertically in dissolved form or alter their migration rate as a result of sorption onto mineral particles. From this perspective, sorption-desorption processes and water infiltration are regarded as important factors when studying radionuclide movement in the soil-water system.

At the same time, the literature emphasizes that the use of specific-activity values alone in assessing vertical radionuclide migration may not fully reveal all migration mechanisms. Radionuclide mobility can be affected by the mineralogical composition and moisture content of soil, pH, carbonate and sulfate compounds, iron and manganese oxides, organic matter, and sorption properties. Therefore, hydrological and geochemical data should also be taken into account when relating the depth distribution of ^{238}U and ^{226}Ra to water-driven migration.

The reviewed literature shows that existing studies have mainly examined radionuclide concentrations in soil, their vertical distribution, the $^{226}Ra/^{238}U$ ratio, and environmental risk. However, linking depth-dependent changes in ^{238}U and ^{226}Ra in reclaimed areas with vertical water infiltration, sorption-desorption processes, and possible radionuclide migration, and subsequently using these data for mathematical modeling, requires separate investigation. From this standpoint, it is appropriate to analyze

ISSN: 2181-3337 | SCIENTISTS.UZ

the ^{238}U and ^{226}Ra data obtained at different depths at P_1 and P_2, determine their $^{226}Ra/^{238}U$ ratios, and evaluate the observed vertical changes in relation to possible migration processes in the soil-water environment.

Materials and methods

To assess the depth-dependent distribution of ^{238}U and ^{226}Ra in soils of the reclaimed area, data obtained at the P_1 and P_2 study points were used. For each point, uranium and radium activity values at different depths and their ratio were considered. The available experimental dataset includes depths of 0.25, 0.50, 0.75, and 1.00 m for P_1 and P_2. The main study parameters were the specific activities of ^{238}U and ^{226}Ra in soil. At P1, the ^{238}U values with depth were 1844.8, 1382.8, 948, and 408 Bq/kg, whereas the corresponding ^{226}Ra values were 521, 831, 1100, and 1400 Bq/kg. At P_2, the values were 3160, 2640, 1210, and 610 Bq/kg for ^{238}U and 512, 1340, 2360, and 3240 Bq/kg for ^{226}Ra.

Assessment of radionuclide distribution with depth

To determine changes in ^{238}U and ^{226}Ra along the soil profile, the specific-activity values at each depth were compared. In analyzing the vertical distribution, the following relative change can be used:

$$\Delta C = (C_z - C_0) / C_0 \times 100\% \quad (1)$$

where C0 is the specific activity of the radionuclide in the initial or upper layer, Bq/kg; Cz is the specific activity of the radionuclide at depth z, Bq/kg; and ΔC is the relative change in radionuclide activity, %.

This indicator makes it possible to quantitatively evaluate the degree to which radionuclide activity decreases or increases with increasing depth.

Calculation of the $^{226}Ra/^{238}U$ activity ratio

To further evaluate the characteristics of vertical radionuclide distribution, the ratio of the specific activities of ^{226}Ra and ^{238}U was calculated:

$$K_{Ra/U} = A(^{226}Ra) / A(^{238}U) \quad (2)$$

where $A(^{226}Ra)$ is the specific activity of ^{226}Ra, Bq/kg; $A(^{238}U)$ is the specific activity of ^{238}U, Bq/kg; and $K_{Ra/U}$ is the $^{226}Ra/^{238}U$ activity ratio.

This indicator was used to assess the relative distribution of the radionuclides. In the study data, the ratio was 0.28, 0.60, 1.16, and 3.43 at P1, and 0.16, 0.51, 1.95, and 5.31 at P2.

To evaluate the relative distribution of radionuclides, it is necessary to determine their balance between soil layers. The balance of radionuclides between soil layers is determined as follows:

$$dM_{i,j}/dt = Q_{i,j}C_{i,j-1} - Q_jC_{i,j} + A_jD_{i,j} - A_{j-1}D_{i,j-1} + \lambda_{i-1}M_{i-1,j} - \lambda_iM_{i,j} + S_{i,j} \quad (3)$$

where $M_{i,j}$ is the mass of the soil layer; i = 1, …, N is the layer number; $C_{i,j}$ is the substance concentration in the i,j-th layer; $D_{i,j-1}$ is the diffusion coefficient in the layer; A_j, A_{j-1}, and A_{j+1} are the specific activities of radionuclides in the j, j-1, and j+1 layers; λ_i and λ_{i-1} refer to the radionuclide decay parameters in the i and i-1 layers as stated in the source; and $S_{i,j}$ denotes the effective transfer coefficients between boundary layers.

Assessment of possible migration processes in the soil-water system

When interpreting changes in radionuclides along the soil profile, vertical water infiltration was considered as a possible migration factor. As water moves through soil pores, radionuclides may be transported in dissolved form or become bound to soil particles.

To characterize radionuclide partitioning between the soil and water phases, the distribution coefficient K_d is expressed as:

$$K_d = C_s / C_w \quad (4)$$

where Cs is the concentration of radionuclide sorbed in soil, and Cw is the radionuclide concentration in water.

ISSN: 2181-3337 | SCIENTISTS.UZ

However, in the present study, Kd, soil bulk density, porosity, water filtration rate, and hydrochemical parameters were not measured experimentally. Therefore, water infiltration was considered only as a possible mechanism for explaining the observed vertical distribution of ^{238}U and ^{226}Ra.

Statistical analysis of the data

The obtained data were arranged according to the depth coordinate, and P1 and P2 were analyzed separately. For each point, the depth-dependent changes in ^{238}U, ^{226}Ra, and KRa/U were determined. The results were presented graphically, and the vertical radionuclide profiles were compared.

The general study algorithm was implemented in the following sequence: soil sampling → determination of ^{238}U, ^{226}Ra, and KRa/U values by depth → construction of vertical-distribution plots → consideration of migration mechanisms → discussion of the obtained results.

Based on the experimental data, the characteristics of vertical radionuclide distribution were identified, providing a methodological basis for the subsequent investigation of these processes using mathematical models related to water infiltration and radionuclide migration.

Results and discussion

In analyzing the study results, the specific activities of ^{238}U and ^{226}Ra measured at different depths at P1 and P2, together with the radioactive-equilibrium coefficient between ^{226}Ra and ^{238}U, were taken as the main indicators. According to the available data, differences were observed between P1 and P2 in the depth distribution of radionuclides. At P1, the specific activity of ^{238}U decreased consistently with increasing depth: 1844.8 Bq/kg at 0.25 m, 1382.8 Bq/kg at 0.50 m, 948 Bq/kg at 0.75 m, and 408 Bq/kg at 1.00 m. Thus, there was a substantial difference between the uppermost and deepest layer values. A similar vertical decrease was observed at P2: the specific activity of ^{238}U was 3160 Bq/kg at 0.25 m, 2640 Bq/kg at 0.50 m, 1210 Bq/kg at 0.75 m, and 610 Bq/kg at 1.00 m.

These results indicate a tendency for ^{238}U to decrease from the surface toward the deeper soil layers at both P_1 and P_2. At the same time, the ^{238}U values at P_2 were higher than those at P_1 at all analyzed depths.

In the case of the vertical distribution of ^{226}Ra, an opposite trend relative to ^{238}U was observed. At P1, the specific activity of ^{226}Ra increased from 521 Bq/kg at 0.25 m to 831 Bq/kg at 0.50 m, 1100 Bq/kg at 0.75 m, and 1400 Bq/kg at 1.00 m. At P2, this difference was even more pronounced: the specific activity of ^{226}Ra was 512 Bq/kg at 0.25 m, 1340 Bq/kg at 0.50 m, 2360 Bq/kg at 0.75 m, and 3240 Bq/kg at 1.00 m.

Thus, the analyzed data show that the activity of ^{238}U decreases with depth, whereas the activity of ^{226}Ra increases. This indicates that the two radionuclides are not distributed in the same manner across the soil layers.

The radioactive-equilibrium coefficient $K^{226}Ra/^{238}U$ changed as follows: at P1, the values at depths of 0.25, 0.50, 0.75, and 1.00 m were 0.28, 0.60, 1.16, and 3.43, respectively. At P_2, the corresponding values were 0.16, 0.51, 1.95, and 5.31.

This result demonstrates a marked change in the ratio between ^{226}Ra and ^{238}U with increasing depth. In particular, at a depth of 1.00 m, the value of 5.31 at P_2 was higher than the value of 3.43 at P_1.

The measured specific activities of ^{226}Ra and ^{238}U at P_1 and P_2 and the radioactive-equilibrium coefficient $K^{226}Ra/^{238}U$ are presented in Table 1.

ISSN: 2181-3337 | SCIENTISTS.UZ

Table 1.

Specific activities of ^{238}U and ^{226}Ra and the radioactive-equilibrium coefficient $K^{226}Ra/^{238}U$ at P_1 and P_2

Depth, m	P1 radionuclide values	P1 radionuclide values	P1 radionuclide values	P2 radionuclide values	P2 radionuclide values	P2 radionuclide values
Depth, m	^{238}U, Bq/kg	^{226}Ra, Bq/kg	$K^{226}Ra/^{238}U$	^{238}U, Bq/kg	^{226}Ra, Bq/kg	$K^{226}Ra/^{238}U$
0.25	1844.8	521	0.28	3160	512	0.16
0.50	1382.8	831	0.60	2640	1340	0.51
0.75	948	1100	1.16	1210	2360	1.95
1.00	408	1400	3.43	610	3240	5.31

As can be seen from Table 1, at P_2 both the initial activity of ^{238}U and the activity of ^{226}Ra in the deeper layers are higher than at P_1.

Based on these results, the dependence of the specific activities of ^{238}U and ^{226}Ra on soil-layer depth at P_1 and P_2 is shown in Figures 1 and 2.

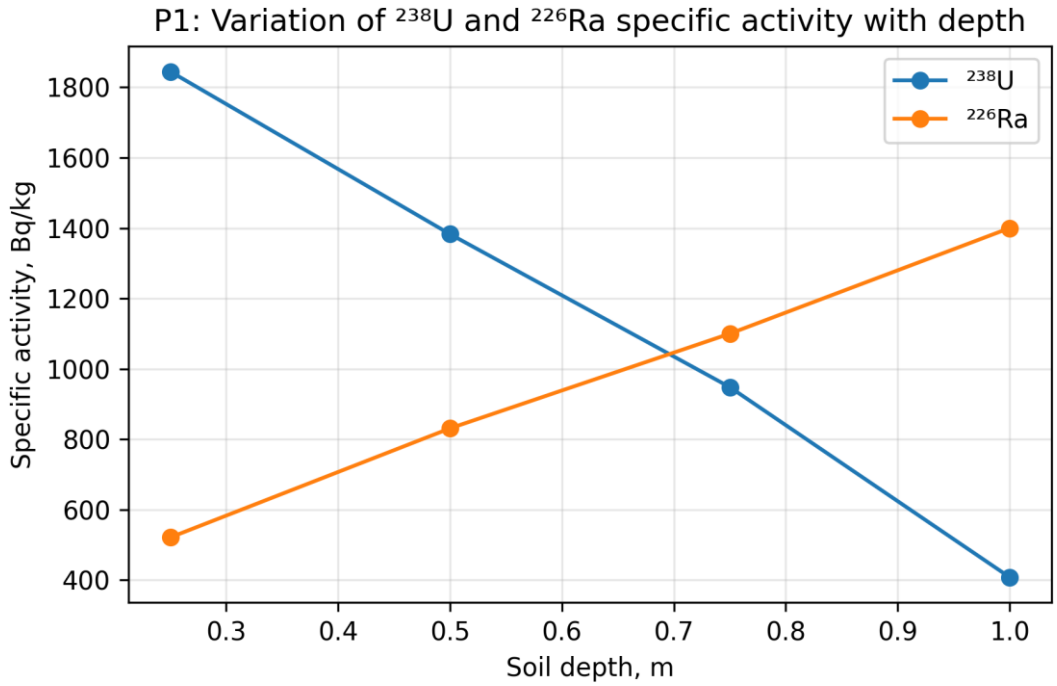


Figure 1. Dependence of the specific activities of ^{238}U and ^{226}Ra on soil-layer depth at P_1.

ISSN: 2181-3337 | SCIENTISTS.UZ

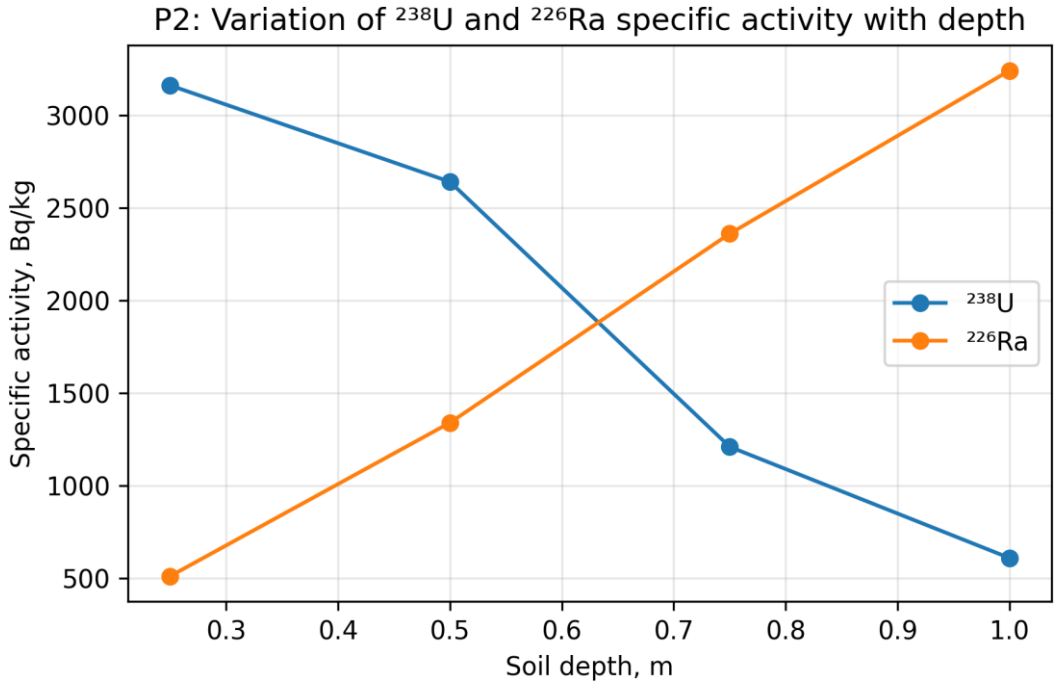


Figure 2. Dependence of the specific activities of ²³⁸U and ²²⁶Ra on soil-layer depth at P_2.

Based on the results of Table 1, a graph showing the variation of the radioactive-equilibrium coefficient $K^{226}Ra/^{238}U$ with soil-layer depth at P_1 and P_2 was constructed (Figure 3).

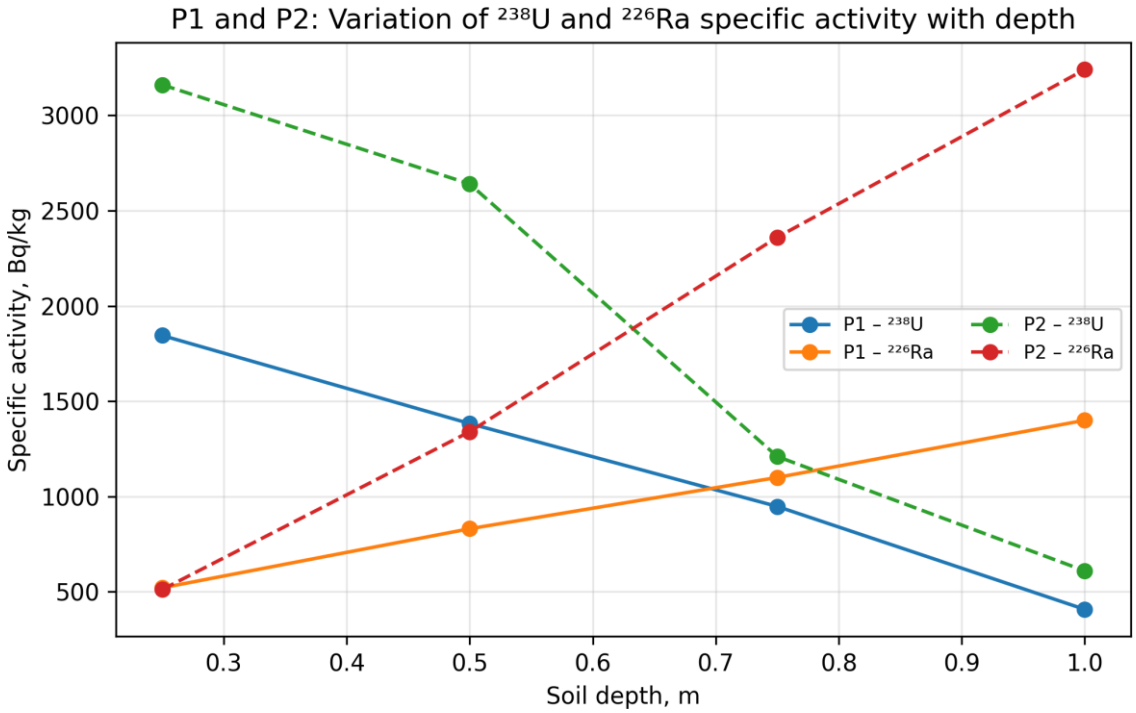


Figure 3. Graph of the depth-dependent variation of the radioactive-equilibrium coefficient $K_{^{226}Ra/^{238}U}$ between the ²²⁶Ra and ²³⁸U radionuclides at P_1 and P_2 based on the results of Table 1.

The obtained results show that the vertical distributions of ²³⁸U and ²²⁶Ra in the soil layers are not identical. The decrease in ²³⁸U and the increase in ²²⁶Ra with depth demonstrate an empirical difference in the way these radionuclides are distributed in the soil environment.

The results can be regarded as experimental evidence indicating the presence of vertical redistribution of radionuclides in the reclaimed area.

The study results showed that the vertical distributions of ²³⁸U and ²²⁶Ra in the soils of the reclaimed area do not have the same pattern. At both P1 and P2, the specific activity of ²³⁸U decreased with increasing

ISSN: 2181-3337 | SCIENTISTS.UZ

depth, while that of ^{226}Ra increased. This indicates that the radionuclides were redistributed differently among the soil layers.

At P_1, ^{238}U decreased from 1844.8 Bq/kg at 0.25 m to 408 Bq/kg at 1.00 m. At the same time, ^{226}Ra increased from 521 to 1400 Bq/kg. At P2, the trend was even more pronounced: ^{238}U decreased from 3160 to 610 Bq/kg, whereas ^{226}Ra increased from 512 to 3240 Bq/kg.

Conclusions

Based on the analysis of the study results, the following conclusions were drawn: clear vertical changes were observed in the distribution of ^{238}U and ^{226}Ra with soil depth at P1 and P2 in the reclaimed area; at P1, the specific activity of ^{238}U decreased from 1844.8 to 408 Bq/kg over the 0.25-1.00 m interval, while at P2 it decreased from 3160 to 610 Bq/kg; in contrast, the specific activity of ^{226}Ra increased from 521 to 1400 Bq/kg at P1 and from 512 to 3240 Bq/kg at P_2; with increasing depth, the $^{226}Ra/^{238}U$ activity ratio changed from 0.28 to 3.43 at P1 and from 0.16 to 5.31 at P_2. The obtained results indicate the presence of vertical redistribution of ^{238}U and ^{226}Ra in soil. The ^{238}U and ^{226}Ra data obtained in this study may be used as initial data for developing a mathematical model of their migration through vertical soil layers while taking radioactive-decay regularities into account.

REFERENCES

1. Музафаров А.М., Аллаберганова Г.М., Турабджанов С.М., Аллаяров Р.М. Новый способ рекультивации загрязнённых радионуклидами почв участков подземного выщелачивания урана // *Universum: Технические науки*. - 2020. - № 6(75), Ч. 2. - С. 91-96.
2. Музафаров А.М., Кулматов Р.А., Аллаяров Р.М. Исследование нарушения коэффициента радиоактивного равновесия между $^{226}Ra/^{238}U$ в пробах урановых объектов // *Горный вестник Узбекистана*. - 2020. - № 4(83). - С. 53-55.
3. Музафаров А.М., Кулматов Р.А., Ражаббоев И., Ёкубов О.М. Способ дезактивации загрязнённых радионуклидами почв, отобранных из участков подземного выщелачивания урана // *Горный информационно-аналитический бюллетень. Физико-химическая геотехнология - инновации и тенденции развития*. - 2021. - С. 110-118.
4. Музафаров А.М., Бобоев А.А. Радиоэкологические факторы и методы их определения в урановых техногенных объектах // *XXI век. Техносферная безопасность*. - 2020. - Т. 5, № 3. - С. 330-336. DOI: 10.21285/2500-1582-2020-3-330-336.
5. Музафаров А.М., Аллаберганова Г.М., Кулматов Р.А. Оценка радиационной опасности урановых предприятий для объектов окружающей среды // *XXI век. Техносферная безопасность*. - 2021. - Т. 6, № 1.
6. Назаров Ж.Т., Музафаров А.М., Умаров Ф.Я., Аллаберганова Г.М. Assessment of Radiation Indicators of Low-Grade Uranium-Bearing Ores for Their Utilization in Processing by the Physico-Chemical Geotechnology Method // *Саноатда рақамли технологиялар / Digital Technologies in Industry*. - 2024. - Vol. 2, No. 4. - P. 57-64. DOI: 10.70769/3030-3214.SRT.2.4.2024.41.

ISSN: 2181-3337 | SCIENTISTS.UZ VOLUME 5 ISSUE 9 | SEPTEMBER 2026

ASSESSMENT OF RADIONUCLIDE PARAMETERS IN SOILS OF RECLAIMED AREAS BASED ON A MATHEMATICAL MODEL

Akbarova Nigora[1], Toshpulatova Dilorom[2,3]

Tashkent State Technical University (TSTU), Tashkent, Uzbekistan[1]
Joint Belorussian–Uzbek Intersectoral Institute of Applied Technical Qualifications in Tashkent, Uzbekistan[2]
Shahrisabz State Pedagogical Institute, Shahrisabz, Uzbekistan[3]

DOI: 10.67620/sai.59a0009

ABSTRACT

Digital holographic interferometry (DHI) requires phase maps to be denoised and unwrapped before reliable displacement can be recovered. Learning-based approaches increasingly address these tasks, but their development requires paired data with known ground-truth displacement, which experimental holograms rarely provide. This study develops a forward model of the DHI measurement chain and a synthetic phase-map generator, then uses them to identify the operating limits of a classical phase-processing pipeline. The model relates interferometric phase to displacement, incorporates multiplicative speckle decorrelation dependent on local fringe density, and adds detector noise. Ground-truth displacement fields are derived from analytical plate-theory solutions. Windowed Fourier filtering followed by reliability-sorted phase unwrapping was evaluated on 96 simulated 256 × 256 interferograms. Under moderate decorrelation, 99.9% of pixels were correctly unwrapped at 10 fringes, with a filtered wrapped-phase RMSE of 0.30 rad; success decreased to 76.9% at 15 fringes and 15.0% at 25 fringes. Under strong decorrelation, the operating limit shifted to approximately 5–10 fringes. Detector SNR from 15 to 35 dB produced no meaningful performance trend because multiplicative decorrelation dominated. These findings indicate that the classical pipeline behaves as a threshold system governed primarily by fringe density and decorrelation. Experimental validation of the noise model remains necessary.

ACCEPTED

05.10.26

Keywords: *digital holographic interferometry; forward model; synthetic dataset; speckle decorrelation; phase unwrapping; windowed Fourier filtering; optical metrology.*



1. Introduction

A digital holographic interferometer records the wave scattered by an object on a sensor and reconstructs the complex field numerically. Subtracting the reconstructed phases of two object states gives a non-contact, full-field displacement map whose sensitivity is finer than one wavelength (Schnars & Jüptner, 2002), (Kreis, 2005). Phase-shifting acquisition (Yamaguchi & Zhang, 1997) is the usual way to retrieve the object field without spatial filtering.

Two effects limit how accurate the resulting phase map can be. The first is speckle decorrelation. The speckle pattern produced by a rough surface changes between the two states, so the phase noise is multiplicative and cannot be treated as purely additive (Goodman, 2020). The second is the 2π ambiguity:

the measured phase is known only modulo 2π and must therefore be unwrapped, and classical unwrapping algorithms spread errors once the noise is strong or the fringes are dense (Ghiglia & Pritt, 1998).

Neural networks have been proposed for speckle denoising (Montresor et al., 2020; Fang et al., 2022), phase unwrapping (Wang et al., 2022) and fringe analysis (Feng et al., 2019). All of them are trained on pairs consisting of a corrupted and a clean phase map. In an experiment, a clean map requires an additional independent measurement, which makes simulated data the practical alternative. Simulated data are useful only if they reproduce what makes real phase maps hard to process, above all the way decorrelation grows with fringe density. A simulation that simply adds Gaussian noise to an ideal phase does not do this.

The aim of this study is to provide a simulator of this kind and to put it to use. We (i) formulate a forward model of the DHI phase chain and implement a generator of wrapped phase maps whose ground truth is an analytical displacement field, and (ii) apply the generator to measure how a classical filtering-plus-unwrapping chain responds to changes in fringe density, detector SNR and decorrelation strength, which shows the regimes where a learned method has room to improve. The study complements our work on a joint denoising and unwrapping network (Akbarova & Toshpulatova, n.d.), which is outside its scope. All results refer to simulated data; no experimental holograms were recorded.

2. Materials and Methods

2.1. Phase–displacement relation

Consider a single illumination and observation geometry with laser wavelength λ and an angle α between the sensitivity vector and the surface normal. The interferometric phase is then related to the out-of-plane displacement d(x,y) by

$$\frac{4\pi}{\lambda} \cdot \mathrm{d}_{x,y} \cdot \cos\alpha \qquad (1)$$

The measured quantity is the wrapped phase $\Delta\varphi_w = W[\Delta\varphi]$, where the operator W folds values into the interval $(-\pi, \pi]$. The simulations used λ = 532 nm, α = 0 and images of 256 × 256 pixels. The fringe count N_f is the total phase range divided by 2π: $N_f = [\max \Delta\varphi - \min \Delta\varphi]/2\pi$.

2.2. Displacement fields

The true displacements were taken from closed-form solutions of classical plate theory (Timoshenko & Woinowsky-Krieger, 1959) rather than from finite-element models. Three cases were used: (i) a clamped circular plate under uniform pressure, $w \propto (1 - r^2/a^2)^2$; (ii) a vibration mode of a simply supported rectangular plate, $w \propto \sin(m\pi x/a)\cdot\sin(n\pi y/b)$ with $m, n \in \{1, 2\}$; (iii) a simply supported square plate under uniform load, described by the Navier series $w \propto \Sigma \sin(m\pi x/a)\cdot\sin(n\pi y/a)/[mn(m^2 + n^2)^2]$ over odd m, n up to 11. The amplitude of each field was scaled so that the phase of Eq. (1) contained the required fringe count Nf, chosen between 2 and 25.

2.3. Speckle and noise model

Two independent, fully developed speckle fields, s_1 (state 1) and s_1', were generated as circular complex Gaussian random fields, smoothed with a Gaussian of 1.5 px and normalized to unit mean intensity. The field in state 2 is constructed as

$$s_2 = \rho \cdot s_1 \cdot \exp(i\Delta\varphi) + \sqrt{(1 - \rho^2)} \cdot s_1' \qquad (2)$$

$$\rho(x,y) = \rho_0 \cdot \exp[-(|\nabla\Delta\varphi|/g_c)^2] \qquad (3)$$

Equation (3) is a modelling assumption: the correlation ρ between the two speckle fields decreases as the local phase gradient, that is, the fringe density, increases. We set $\rho_0 = 0.95$ and used two values of g_c: 1.0 rad/px for moderate decorrelation and 0.6 rad/px for strong decorrelation. Neither value was fitted to experimental data. Additive detector noise n_1, n_2 (circular complex Gaussian, variance $10^{-\mathrm{SNR}/10}$ for unit mean intensity) was then added to both fields, and the wrapped phase is

$$\Delta\varphi_w = \arg[(s_2 + n_2)(s_1 + n_1)\dagger] \qquad (4)$$

ISSN: 2181-3337 | SCIENTISTS.UZ

The generator parameters are summarized in Table 1.

Parameter	Value	Comment
Image size	256 × 256 px	—
Wavelength, sensitivity angle	532 nm, α = 0	Eq. (1)
Displacement fields	3 analytical plate solutions	Section 2.2
Fringe count N_f	2, 5, 10, 15, 20, 25	Phase range / 2π
Speckle size	1.5 px (Gaussian smoothing)	Unit mean intensity
Decorrelation ρ_0; g_c	0.95; 1.0 (moderate) or 0.6 rad/px (strong)	Assumed, Eq. (3)
Detector SNR	15, 20, 25, 30, 35 dB	Additive, both fields

Table 1. Parameters of the synthetic data generator.

2.4. Classical processing chain

The reference method is a two-dimensional windowed Fourier filter (Kemao, 2007) followed by phase unwrapping. The wrapped phase is converted to exp(iΔφw) and analysed with a Gaussian window of σw = 6 px on a 13 × 13 grid of spatial frequencies (±0.9 rad/px, step 0.15 rad/px). Coefficients whose magnitude falls below 2.5 times a noise level, estimated as the median coefficient magnitude, are set to zero, and the field is then reconstructed. Unwrapping uses the reliability-sorted, non-continuous-path algorithm of Herráez et al. (Herráez et al., 2002) in its scikit-image implementation (van der Walt et al., 2014). The filter settings were identical for all conditions and were not tuned for any of them. For comparison, the noisy phase was also unwrapped directly, without filtering.

2.5. Metrics and experimental design

Three quantities were evaluated against the ground truth: (i) the wrapped-phase RMSE, which characterizes the filtering stage; (ii) the unwrapping success, defined as the fraction of pixels where the estimated phase deviates from the truth by less than π after a global multiple of 2π has been removed; and (iii) the computation time of the chain on one CPU core.

$$RMSE = \frac{\sqrt{\Sigma W[\Delta\hat{\varphi}w - \Delta\varphi]^2}}{N} \quad (5)$$

Every condition was simulated 6 times (two realizations per displacement field, each with its own random seed), and results are reported as mean ± standard deviation over these 6 realizations. Two series were run: over N_f at 20 dB for both decorrelation regimes, and over SNR at N_f = 10 for moderate decorrelation. In addition, phase noise on a flat field (Δφ = 0) was measured for ρ_0 = 1.0, 0.9 and 0.8. The classical chain processed 96 interferograms in total (the point at N_f = 10 and 20 dB belongs to both series).

2.6. Check of the filter frequency range

The fixed frequency range of the filter (±0.9 rad/px) is narrower than the maximum local phase gradient at 15 or more fringes (about 1.1–2.0 rad/px). To test whether this limitation explains the failures, 3 realizations per condition were processed again at 15, 20 and 25 fringes (moderate decorrelation), with the range widened to 1.2 times the maximum gradient.

3. Results

3.1. Characteristics of the generator

Examples of generated data are shown in Fig. 1. With detector noise alone (ρ_0 = 1), the standard deviation of the flat-field phase noise dropped from 0.43 rad at 15 dB to 0.059 rad at 35 dB, roughly in proportion to $10^{-SNR/20}$ (Fig. 2). For ρ_0 = 0.9 it decreased only from 0.76 to 0.69 rad over the same range, and for ρ_0 = 0.8 from 0.96 to 0.92 rad; above about 25 dB the curves were flat. At N_f = 10, 30 dB and strong decorrelation, the standard deviation of the wrapped-phase error grew with the local phase gradient, from 0.53 rad where $|\nabla\Delta\varphi| < 0.1$ rad/px (mean ρ = 0.95) to 1.55 rad where $|\nabla\Delta\varphi| \geq 0.45$ rad/px (mean ρ = 0.30).

ISSN: 2181-3337 | SCIENTISTS.UZ

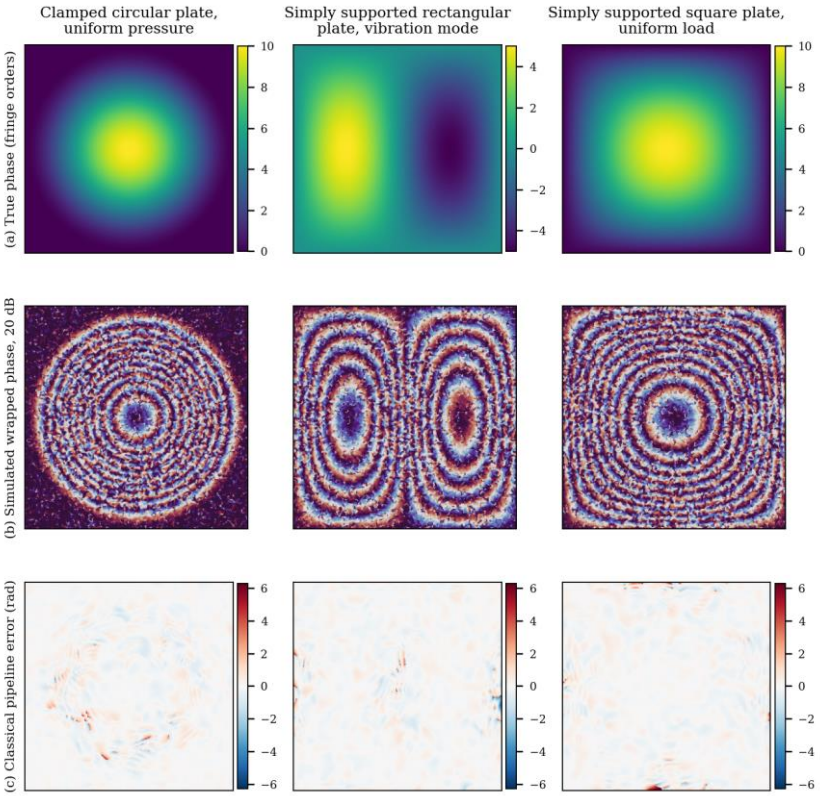


Figure 1. Generator output at N_f = 10, 20 dB and moderate decorrelation: (a) true phase in fringe orders; (b) simulated wrapped phase; (c) error of the WFF + unwrapping chain after removal of a global 2π multiple (clipped to ±2π).

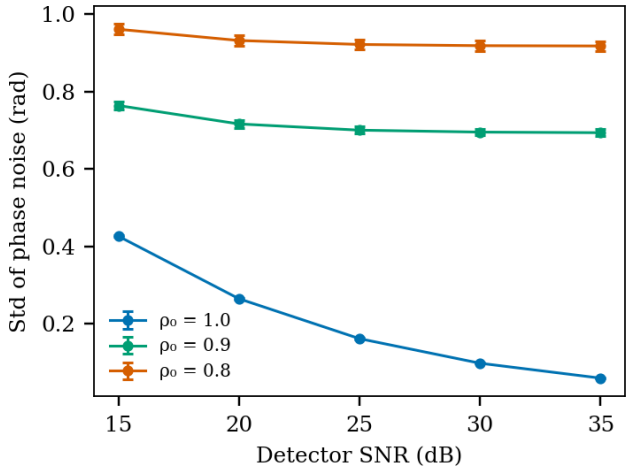


Figure 2. Standard deviation of the flat-field phase noise versus detector SNR for three values of ρ_0 (6 realizations; error bars show the SD).

3.2. Classical chain versus fringe count

Results of the fringe-density series at 20 dB are given in Table 2 and Fig. 3. Under moderate decorrelation, 99.9% of pixels were unwrapped correctly at 10 fringes, and the wrapped-phase RMSE after filtering was 0.30 rad (0.12 rad at 2 fringes). At 15 fringes the success dropped to 77% and the RMSE of the unwrapped phase rose to about 10 rad owing to 2π errors; at 20 and 25 fringes only 22% and 15% of pixels were correct. Under strong decorrelation the chain was reliable up to 5 fringes, gave 76% at 10 fringes and 8% at 15 fringes. Unwrapping without prior filtering succeeded for 98% of pixels at 5 fringes but for only 60% at 10 fringes (moderate decorrelation). Between 20 and 25 fringes the wrapped-phase RMSE after filtering (1.4–1.5 rad) was close to that of the noisy input (1.5 rad).

ISSN: 2181-3337 | SCIENTISTS.UZ

N_f	Moderate: correct pixels, %	Moderate: RMSE after WFF, rad	Strong: correct pixels, %	Strong: RMSE after WFF, rad	Unwrap only (moderate), %
2	100.0 ± 0.0	0.12 ± 0.00	100.0 ± 0.0	0.13 ± 0.01	99.4 ± 0.0
5	100.0 ± 0.0	0.16 ± 0.01	100.0 ± 0.0	0.25 ± 0.01	98.2 ± 0.4
10	99.9 ± 0.1	0.30 ± 0.02	76.4 ± 9.6	0.92 ± 0.02	59.6 ± 13.1
15	76.9 ± 9.3	0.89 ± 0.02	8.3 ± 2.9	1.47 ± 0.10	19.2 ± 14.1
20	22.1 ± 19.0	1.39 ± 0.08	6.3 ± 2.3	1.61 ± 0.12	9.7 ± 6.5
25	15.0 ± 23.3	1.47 ± 0.18	4.1 ± 0.7	1.64 ± 0.12	6.2 ± 3.3

Table 2. Classical chain versus fringe count at 20 dB (mean ± SD, 6 realizations per row). "Correct pixels" is the unwrapping success defined in Section 2.5.

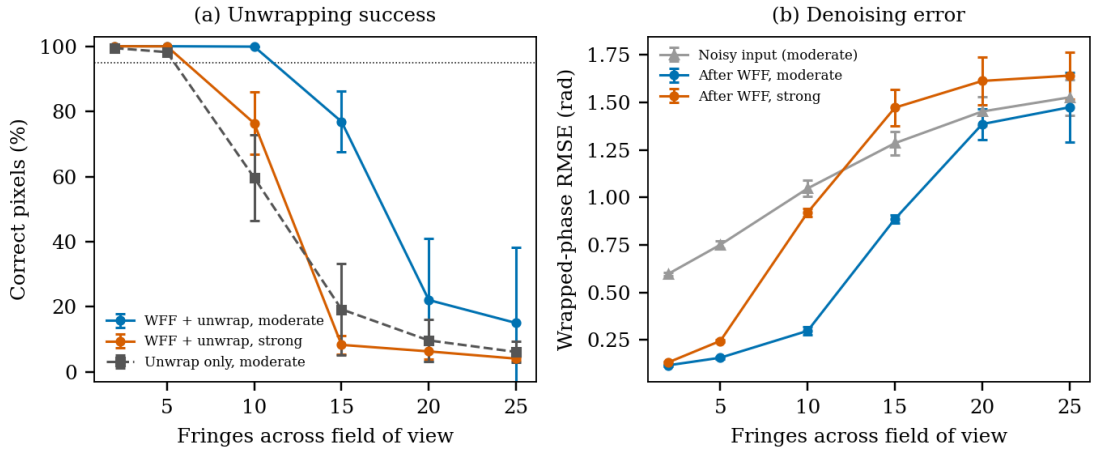


Figure 3. (a) Unwrapping success and (b) wrapped-phase RMSE versus fringe count at 20 dB. The dotted line in (a) marks 95%.

3.3. Classical chain versus detector SNR

The SNR series at 10 fringes and moderate decorrelation is presented in Table 3. Between 15 and 35 dB the success remained at 99.8–99.9% and the RMSE after filtering at 0.28–0.30 rad, with no visible trend. The mean computation time of the chain was 2.76 ± 0.09 s per 256 × 256 field, of which unwrapping accounted for 0.021 s.

SNR, dB	Correct pixels, %	RMSE after WFF, rad	RMSE of noisy input, rad
15	99.9 ± 0.0	0.28 ± 0.02	1.02 ± 0.06
20	99.9 ± 0.1	0.30 ± 0.02	1.05 ± 0.04
25	99.8 ± 0.1	0.29 ± 0.03	1.01 ± 0.06
30	99.8 ± 0.1	0.29 ± 0.02	1.03 ± 0.04
35	99.9 ± 0.1	0.30 ± 0.02	1.01 ± 0.06

Table 3. Classical chain versus detector SNR at N_f = 10, moderate decorrelation (mean ± SD, 6 realizations).

3.4. Effect of widening the filter frequency range

Extending the range to 1.2 times the maximum gradient (Section 2.6) did not improve the wrapped-phase RMSE after filtering, which was 0.95 rad at 15 fringes, 1.3–1.4 rad at 20 fringes and 1.4–1.6 rad at 25 fringes. The unwrapping success was 59–71% at 15 fringes and 3–10% at 20–25 fringes.

4. Discussion

The main finding is that the classical chain has a fairly sharp operating limit. Under moderate decorrelation it works well up to about 10 fringes and breaks down between 10 and 15; under strong decorrelation the breakdown moves to 5–10 fringes. The chain behaved as a threshold system: it was either

ISSN: 2181-3337 | SCIENTISTS.UZ

accurate or failing, with little in between. For this reason the mean RMSE of the unwrapped phase is a poor summary, and the success fraction should be reported alongside it. Pre-filtering with WFF extended the usable range from about 5 to about 10 fringes, but beyond 20 fringes it no longer improved the phase, since the RMSE after filtering was close to that of the noisy input.

The results point to decorrelation, not the filter, as the cause of the failures. Widening the filter band did not help (Section 3.4), so in this model the breakdown at high fringe density comes from phase information lost through decorrelation rather than from a limited filter range. The same conclusion follows from the flat-field and SNR series (Fig. 2, Table 3): above about 25 dB the phase error is set by decorrelation and no longer by the detector. The growth of the phase error with the local gradient (Section 3.1) is exactly the coupling between noise and fringe density that the model was built to reproduce.

These findings have two consequences for the design of training data. First, a learned method can show an advantage only near and beyond the classical limit, so a training set should contain fringe densities and decorrelation strengths on both sides of that limit. Second, a dataset that varies only the SNR would cover the wrong axis; the decorrelation parameters should be sampled explicitly.

The values obtained here, about 0.3 rad of wrapped-phase RMSE at 10 fringes and a fall in success between 10 and 15 fringes, are of the same order as the classical-chain figures assumed in our companion work (Akbarova & Toshpulatova, n.d.). They nevertheless apply to one specific model and to one untuned implementation of the filter and the unwrapper, and they should not be taken as the best that classical methods can achieve. The timing result likewise belongs to an unoptimized single-core implementation; it shows only that the filtering stage, not the unwrapping, dominates the cost of the classical chain.

Limitations. (1) All data are simulated; the agreement of Eqs. (2)–(3) with speckle decorrelation in a real interferometer has not been tested, and $\rho 0$ and gc are assumed values. The next step is a comparison with experimental phase maps, for example the benchmark database of Montresor et al. (Montresor et al., 2020), using the distributions of local phase deviation and the residual-noise correlation length at matched fringe density. (2) The displacement fields are analytical plate-theory solutions; finite-element fields for more complex specimens and loading are not yet included. (3) Only out-of-plane displacement in a single-illumination geometry is modelled. (4) Each condition was simulated 6 times, so the standard deviations in Tables 2 and 3 are rough estimates. (5) Timing was measured on one CPU core with unoptimized code.

5. Conclusion

We developed a forward model of the DHI phase chain that combines multiplicative, fringe-density-dependent speckle decorrelation with additive detector noise, together with a generator of synthetic phase maps with analytical ground truth. Using it, a windowed Fourier filter followed by reliability-sorted unwrapping correctly unwrapped 99.9% of pixels at 10 fringes and 77% at 15 fringes under moderate decorrelation, and its operating range shrank to 5–10 fringes under strong decorrelation. Between 15 and 35 dB the result did not depend on the detector SNR. Before synthetic data from this model are used to train or qualify a measurement method, the model must be checked against experimental holograms.

REFERENCES

1. Akbarova, N. A., & Toshpulatova, D. (n.d.). Deep-learning-assisted digital holographic interferometry for non-contact measurement of deformation, vibration, and elastic properties [Manuscript submitted for publication].
2. Fang, Q., Xia, H., Song, Q., Zhang, M., Guo, R., Montresor, S., & Picart, P. (2022). Speckle denoising based on deep learning via a conditional generative adversarial network in digital holographic interferometry. *Optics Express, 30*(12), 20666–20683.
3. Feng, S., Chen, Q., Gu, G., Tao, T., Zhang, L., Hu, Y., Yin, W., & Zuo, C. (2019). Fringe pattern analysis using deep learning. *Advanced Photonics, 1*(2), 025001.

4. Ghiglia, D. C., & Pritt, M. D. (1998). *Two-dimensional phase unwrapping: Theory, algorithms, and software*. Wiley.
5. Goodman, J. W. (2020). *Speckle phenomena in optics: Theory and applications* (2nd ed.). SPIE Press.
6. Herráez, M. A., Burton, D. R., Lalor, M. J., & Gdeisat, M. A. (2002). Fast two-dimensional phase-unwrapping algorithm based on sorting by reliability following a noncontinuous path. *Applied Optics, 41*(35), 7437–7444.
7. Kemao, Q. (2007). Two-dimensional windowed Fourier transform for fringe pattern analysis: Principles, applications and implementations. *Optics and Lasers in Engineering, 45*(2), 304–317.
8. Kreis, T. (2005). *Handbook of holographic interferometry: Optical and digital methods*. Wiley-VCH.
9. Montresor, S., Tahon, M., Laurent, A., & Picart, P. (2020). Computational de-noising based on deep learning for phase data in digital holographic interferometry. *APL Photonics, 5*(3), 030802.
10. Schnars, U., & Jüptner, W. (2002). Digital recording and numerical reconstruction of holograms. *Measurement Science and Technology, 13*(9), R85–R101.
11. Timoshenko, S., & Woinowsky-Krieger, S. (1959). *Theory of plates and shells* (2nd ed.). McGraw-Hill.
12. van der Walt, S., Schönberger, J. L., Nunez-Iglesias, J., Boulogne, F., Warner, J. D., Yager, N., Gouillart, E., & Yu, T. (2014). scikit-image: Image processing in Python. *PeerJ, 2*, e453.
13. Wang, K., Kemao, Q., Di, J., & Zhao, J. (2022). Deep learning spatial phase unwrapping: A comparative review. *Advanced Photonics Nexus, 1*(1), 014001.
14. Yamaguchi, I., & Zhang, T. (1997). Phase-shifting digital holography. *Optics Letters*, *22*(16), 1268–1270.

ISSN: 2181-3337 | SCIENTISTS.UZ VOLUME 5 ISSUE 9 | SEPTEMBER 2026

STUDY OF THE MECHANICAL STABILITY AND FIRE RESISTANCE OF FLAME-RETARDANT-MODIFIED POLYESTER–MINERAL COMPOSITES

Tursunov Rovshan[1], Buvaraimov Ziyodullo[2], Nurqulov Fayzulla[3]

Tashkent Research Institute of Chemical Technology, Tashkent, Uzbekistan; Independent Researcher[1]
Tashkent Research Institute of Chemical Technology, Tashkent, Uzbekistan; PhD in Technical Sciences, Senior Researcher[2]
Tashkent Research Institute of Chemical Technology, Tashkent, Uzbekistan; Doctor of Technical Sciences (DSc), Professor[3]

DOI: 10.67620/sai.59a0010

ABSTRACT

This study investigated the composition, preparation, mechanical behavior, and fire performance of decorative polymer–mineral composites based on polyester resin. $CaCO_3$, SiO_2, and marble granules were used as mineral fillers, while ammonium phosphate and $Al(OH)_3$ were incorporated as flame-retardant additives. Poliefir-1–Poliefir-4 and an Analog sample were compared in terms of maximum force, maximum stress, elongation, and strain. Poliefir-2 showed the highest strength, whereas Poliefir-3 showed greater deformability. Among the flame-retardant formulations, FR-1 combined high load-bearing capacity with deformation stability, while FR-9 exhibited the highest maximum stress. Limiting oxygen index (LOI) results indicated that increasing the flame-retardant phase improved resistance to combustion; FR-9 and FR-10 reached the highest LOI ranges, supporting the effectiveness of the combined ammonium phosphate and $Al(OH)_3$ system. Overall, the results demonstrate that the proportions and types of mineral fillers and flame-retardant additives strongly influence both mechanical response and fire resistance. Optimizing these components can provide a practical balance among strength, deformation capacity, and fire safety for decorative composites used in construction and interior finishing applications.

ACCEPTED

05.10.26

Keywords: *polyester composites, mineral fillers, flame retardants, mechanical properties, limiting oxygen index (LOI).*

CC BY

Introduction

Study of the Mechanical Stability and Fire Resistance of Flame-Retardant-Modified Polyester–Mineral Composites

Unsaturated polyester resins (UPRs) are widely used thermosetting matrices because of their processability, cost effectiveness, and broad mechanical and chemical performance, including in construction-related applications (Malik et al., 2000; Seraji et al., 2022). Their inherent flammability, however, has motivated extensive research on additive and reactive flame-retardant systems (Chu, Hu, et al., 2024).

Ammonium polyphosphate (APP) is among the most common phosphorus-containing flame retardants for UPR, but its loading level and interaction with the polymer matrix can affect both fire performance and mechanical properties (Chu, Lu, et al., 2024). Prior work has examined APP in

combination with phosphinate salts (Reuter et al., 2020), triphenyl phosphate (Pan et al., 2012), aluminum hydroxide (Chen et al., 2017), metallic oxides and alumina-based fillers (Tibiletti et al., 2011), and magnesium hydroxide (Tang et al., 2013), demonstrating that flame-retardant efficiency depends strongly on the broader formulation.

Recent studies have also explored surface-modified APP and hybrid architectures, including chitosan/APP-coated diatomite (Chen et al., 2020), ionic-liquid-functionalized imogolite nanotubes with APP (Zhu et al., 2022), Schiff-base-coated APP (Zhang et al., 2023), and other synergistic systems designed to preserve multiple functional properties (Liu et al., 2020). Mineral reinforcement is also relevant: marble-containing polyester composites can provide useful combinations of mechanical properties and fire resistance (Abenojar et al., 2021). The limiting oxygen index (LOI) is a widely used indicator of combustion resistance, with ambient-temperature testing standardized in ISO 4589-2 (International Organization for Standardization, 2017).

Against this background, the present study examined decorative polymer–mineral composites based on polyester resin and modified with $CaCO_3$, SiO_2, marble granules, ammonium phosphate, and $Al(OH)_3$. Poliefir-series and FR-series formulations were compared to determine how mineral-filler type and flame-retardant loading affected maximum force, maximum stress, elongation, strain at break, and LOI. The objective was to identify formulations that provide an appropriate balance between mechanical stability, deformation capacity, and fire resistance.

Materials and Methods

Materials and Formulations

The study investigated decorative polymer–mineral composite materials based on polyester resin, including Poliefir-1, Poliefir-2, Poliefir-3, Poliefir-4, and Analog samples, as well as fire-resistant formulations designated FR-10, FR-9, FR-1, FR-4, and FR-3. In all compositions, polyester resin served as the binder matrix. Finely dispersed $CaCO_3$ and SiO_2 were used to form the mineral phase, while marble granules with a particle size of 0.5–3 mm were incorporated into selected formulations. To improve the fire resistance of the composites, ammonium phosphate (AP) and $Al(OH)_3$ were introduced as flame-retardant additives. Accelerator and curing-agent components were used to control the curing process of the polyester resin.

The compositions of the Poliefir-series samples differed in the type and amount of mineral fillers. Poliefir-1 contained 29.31 wt.% polyester resin, 54.63 wt.% $CaCO_3$, 5.86 wt.% SiO_2, and 10.00 wt.% ammonium phosphate, with no marble granules or $Al(OH)_3$ added. Poliefir-2 consisted of 36.84 wt.% polyester resin, 18.87 wt.% SiO_2, 34.14 wt.% marble granules, and 10.00 wt.% ammonium phosphate. $CaCO_3$ and $Al(OH)_3$ were not used in this formulation. Poliefir-3 contained 27.68 wt.% polyester resin, 51.60 wt.% $CaCO_3$, 5.54 wt.% SiO_2, 10.00 wt.% ammonium phosphate, and 5.00 wt.% $Al(OH)_3$. Poliefir-4 consisted of 34.79 wt.% polyester resin, 17.82 wt.% SiO_2, 32.25 wt.% marble granules, 10.00 wt.% ammonium phosphate, and 5.00 wt.% $Al(OH)_3$. In all Poliefir-series compositions, small amounts of accelerator and curing-agent components were added to bring the total formulation to 100 wt.%. The Analog sample was used as a reference specimen for comparative evaluation of the mechanical properties of the experimental composites and was prepared under the same technological conditions as the other samples.

In the FR-series composites, the main compositional variables were a decrease in polyester resin content and an increase in the proportion of flame-retardant components. The FR-1 formulation selected for mechanical testing contained 30.00 wt.% polyester resin, 27.00 wt.% $CaCO_3$, 5.00 wt.% SiO_2, 20.00 wt.% marble granules, 8.00 wt.% ammonium phosphate, and 9.80 wt.% $Al(OH)_3$. In FR-3, the polyester resin content was reduced to 29.00 wt.%, while the formulation contained 25.00 wt.% $CaCO_3$, 5.00 wt.% SiO_2, 20.00 wt.% marble granules, 10.00 wt.% ammonium phosphate, and 10.80 wt.% $Al(OH)_3$. FR-4

ISSN: 2181-3337 | SCIENTISTS.UZ

consisted of 29.00 wt.% polyester resin, 18.00 wt.% $CaCO_3$, 6.00 wt.% SiO_2, 27.00 wt.% marble granules, 10.00 wt.% ammonium phosphate, and 9.80 wt.% $Al(OH)_3$.

In the FR-9 formulation, which contained a higher proportion of flame-retardant additives, polyester resin accounted for 26.00 wt.%, $CaCO_3$ for 21.00 wt.%, SiO_2 for 5.00 wt.%, marble granules for 16.00 wt.%, ammonium phosphate for 16.00 wt.%, and $Al(OH)_3$ for 15.83 wt.%. In the FR-10 composition, the polyester resin content was likewise maintained at 26.00 wt.%, while the $CaCO_3$ content was reduced to 14.00 wt.%, the SiO_2 content was increased to 6.00 wt.%, and the amount of marble granules was increased to 23.00 wt.%. This formulation contained 16.00 wt.% ammonium phosphate and 14.82 wt.% $Al(OH)_3$. In all FR-series compositions, the amounts of accelerator and curing-agent components were maintained at approximately 0.02 wt.% and 0.14–0.18 wt.%, respectively.

Specimen Preparation and Testing

The prepared mixtures were initially cured at 20–25 °C for at least 6 h. After completion of the curing process, the specimens were removed from the molds and stored under stable conditions prior to testing. In particular, the results obtained for Poliefir-1–Poliefir-4 and the Analog sample made it possible to evaluate the effects of mineral filler type and $Al(OH)_3$ addition on the mechanical properties. The FR-1, FR-3, FR-4, FR-9, and FR-10 formulations enabled a comparative assessment of changes in tensile behavior and strain-at-break characteristics associated with increasing amounts of ammonium phosphate and $Al(OH)_3$.

Fire performance was evaluated using the limiting oxygen index (LOI), and the resulting LOI values were compared across the Poliefir and FR formulations.

Results and Discussion

It was found that the tensile mechanical properties of polyester-based decorative polymer–mineral composites were significantly dependent on their composition. The results presented in Table 1 show that the maximum load, stress, elongation, and relative strain values of the Poliefir-1–Poliefir-4 and Analog samples did not change according to the same trend. This indicates that the load-bearing capacity of the composites is determined not only by the proportion of the polyester matrix but also by the type, particle dispersion, amount, and degree of distribution of the mineral fillers within the matrix.

Table 1

Tensile Mechanical Properties of Poliefir-1–Poliefir-4 and Analog Decorative Polymer–Mineral Composites

Sample name	Maximum force, calculated over all regions (N)	Maximum stress, calculated over all regions (MPa)	Maximum elongation, calculated over all regions (mm)	Maximum strain, calculated over all regions (%)	Force at break, sensitivity: 10 (N)	Stress at break, sensitivity: 10 (MPa)	Elongation at break, sensitivity: 10 (mm)	Strain at break, sensitivity: 10 (%)
Poliefir-1	1851.56	8.05025	1.90920	6.36400	1851.56	8.05025	1.90920	6.36400
Poliefir-2	2280.93	8.14617	3.64787	12.1596	2280.93	8.14617	3.64787	12.1596
Poliefir-3	1812.79	4.31617	4.45417	14.8472	1804.45	4.29630	4.46670	14.8890
Analog	1802.23	6.00744	1.51787	5.05956	1802.23	6.00744	1.51787	5.05956
Poliefir-4	1935.86	5.69370	2.51957	8.39856	1935.86	5.69370	2.51957	8.39856

Mechanical Properties of Poliefir-Series Composites

According to the data in Table 1, the Poliefir-2 sample exhibited the highest maximum force, reaching 2280.93 N. Its maximum stress was also 8.14617 MPa, the highest value among the Poliefir formulations investigated. The use of 36.84 wt.% polyester resin, 18.87 wt.% SiO_2, and 34.14 wt.% marble granules with a particle size of 0.5–3 mm in this formulation may have promoted effective load distribution between the polymer phase and the rigid mineral particles. As a result, the material's resistance to external loading increased. The maximum force of Poliefir-2 was approximately 26.6% higher than that of the

ISSN: 2181-3337 | SCIENTISTS.UZ

Analog sample, indicating that the selected mineral composition was effective in enhancing mechanical strength.

For the Poliefir-1 sample, the maximum force was 1851.56 N and the maximum stress was 8.05025 MPa. Although these values were slightly lower than those of Poliefir-2, the stress value was substantially higher than that of the Analog formulation. The $CaCO_3$ content in Poliefir-1 reached 54.63 wt.%, providing a high proportion of the mineral phase. Finely dispersed $CaCO_3$ particles may fill voids in the polymer matrix and contribute to densification of the composite. At the same time, the absence of marble granules limited the deformation behavior of this sample: the maximum elongation was 1.90920 mm and the relative strain was 6.364%.

A different trend in mechanical properties was observed for the Poliefir-3 sample. Although this formulation was not the leading one in terms of maximum force and stress, the maximum elongation reached 4.45417 mm and the strain reached 14.8472%. At break, these values were 4.46670 mm and 14.8890%, respectively. Thus, Poliefir-3 demonstrated relatively high deformability. This behavior may be associated with the incorporation of 5 wt.% $Al(OH)_3$, the reduced polyester-matrix content, and the presence of a $CaCO_3$-based mineral phase. The combined effect of the mineral and flame-retardant components altered not only the stiffness of the material but also its deformation mechanism.

In Poliefir-3, the maximum force was 1812.79 N and the force at break was 1804.45 N, with only a very small difference between them. This indicates that the sample did not undergo a sharp loss of load after reaching the maximum load. At the same time, the close values of maximum strain and strain at break indicate that the deformation process continued consistently up to failure. Such behavior may be important for decorative materials because the ability of a material to undergo a certain degree of deformation under external loading rather than immediately transition to brittle failure can improve service reliability.

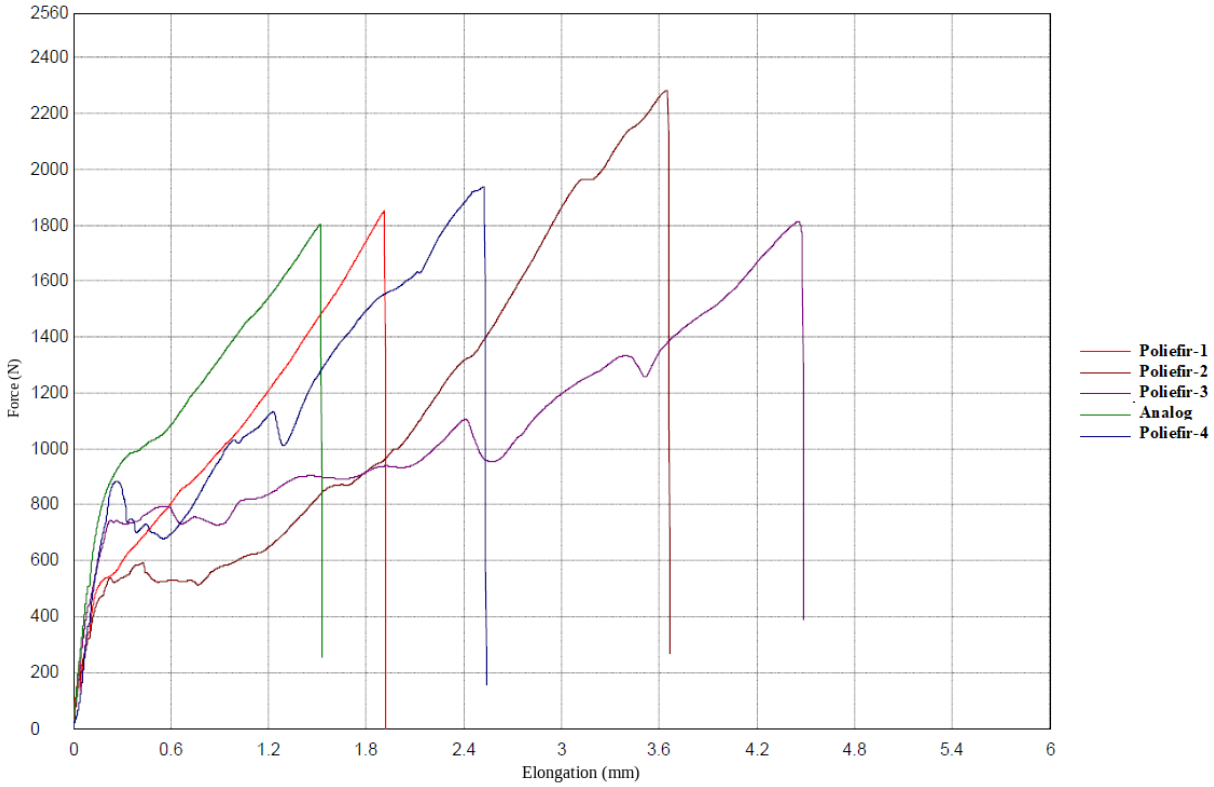
The Poliefir-4 sample exhibited a maximum load of 1935.86 N, which was higher than that of the Analog sample. However, the maximum stress was 5.69370 MPa, lower than the values obtained for Poliefir-1 and Poliefir-2. The maximum strain was 8.39856%, while the elongation was 2.51957 mm. The simultaneous presence of marble granules and $Al(OH)_3$ in this formulation produced intermediate mechanical behavior: the material deformed more than Poliefir-1 but did not reach the extensibility observed for Poliefir-3.

The Analog sample, used as the reference, exhibited a maximum force of 1802.23 N and a stress of 6.00744 MPa. Its maximum elongation was limited to 1.51787 mm and its strain to 5.05956%. Thus, most of the experimental formulations showed an increase in either load-bearing capacity or deformability relative to the Analog sample. In particular, the pronounced increase in strength for Poliefir-2 and in deformation capacity for Poliefir-3 confirms that decorative materials with different performance characteristics can be obtained through targeted modification of the formulation parameters.

ISSN: 2181-3337 | SCIENTISTS.UZ

Figure 1

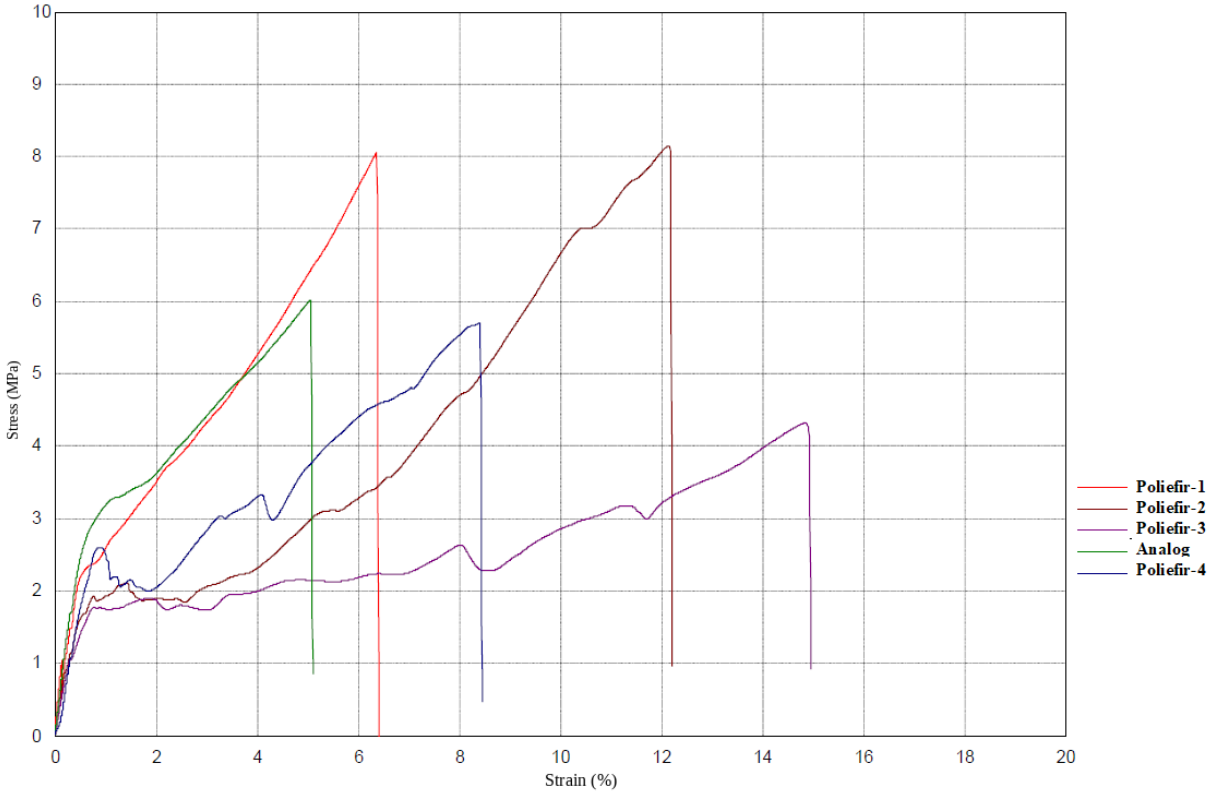
Maximum Force Values of Poliefir-1–Poliefir-4 and Analog Samples



The results presented in Figures 1–2 complement the data in Table 1 and more clearly illustrate the differences between the samples in their ability to reach maximum values and in their deformation ranges. Joint evaluation of the tabular and graphical data shows that Poliefir-2 is distinguished by its strength characteristics, whereas Poliefir-3 exhibits relatively greater deformability. Poliefir-1 and Poliefir-4 demonstrate mechanical behavior intermediate between these two cases.

Figure 2

Maximum Strain Values of Poliefir-1–Poliefir-4 and Analog Samples



ISSN: 2181-3337 | SCIENTISTS.UZ

Tensile Properties of FR-Series Composites

In the FR formulations with increased amounts of flame-retardant components, the changes in mechanical characteristics were more pronounced. According to the data in Table 2, FR-1 exhibited the highest maximum load in this group, reaching 2285.74 N. Its maximum elongation was 5.02377 mm and its strain was 16.7459%, among the highest values in the group. At break, the force was 2281.93 N, the stress 7.13102 MPa, the elongation 5.03127 mm, and the strain 16.7709%. The near coincidence of the maximum and break values indicates that the material maintained stable resistance until the end of loading.

The FR-1 formulation contained 30 wt.% polyester resin, 27 wt.% $CaCO_3$, 5 wt.% SiO_2, 20 wt.% marble granules, 8 wt.% ammonium phosphate, and 9.80 wt.% $Al(OH)_3$. At this ratio, a relatively balanced structural system may have formed among the organic matrix, finely dispersed particles, and coarse mineral filler. Consequently, the composite was able to withstand a high load while retaining substantial elongation.

The FR-9 sample exhibited the highest maximum stress, reaching 9.32198 MPa. The maximum force was 2237.27 N, the elongation 4.28413 mm, and the strain 14.2804%. The maximum and break values for this sample were observed to coincide completely. This indicates that failure of the FR-9 sample occurred very close to the final loading point. Despite increasing the ammonium phosphate content to 16 wt.% and $Al(OH)_3$ to 15.83 wt.%, the material retained a high level of mechanical stress. This result indicates that increasing the flame-retardant content does not necessarily lead to a sharp reduction in mechanical strength; rather, the effect develops in conjunction with the overall mineral structure of the composite.

Table 2

Tensile Mechanical Properties of FR-1, FR-3, FR-4, FR-9, and FR-10 Decorative Polymer–Mineral Composites

Sample name	Maximum force, calculated over all regions (N)	Maximum stress, calculated over all regions (MPa)	Maximum elongation, calculated over all regions (mm)	Maximum strain, calculated over all regions (%)	Force at break, sensitivity: 10 (N)	Stress at break, sensitivity: 10 (MPa)	Elongation at break, sensitivity: 10 (mm)	Strain at break, sensitivity: 10 (%)
FR-10	159.814	0.98650	0.18517	0.61722	—	—	—	—
FR-9	2237.27	9.32198	4.28413	14.2804	2237.27	9.32198	4.28413	14.2804
FR-1	2285.74	7.14295	5.02377	16.7459	2281.93	7.13102	5.03127	16.7709
FR-4	1816.80	5.67751	4.94193	16.4731	1816.14	5.67543	4.95687	16.5229
FR-3	1824.96	6.51770	2.59800	8.66000	1773.95	6.33553	2.62303	8.74344

Note. Dashes indicate break values that were not reported for FR-10.

For FR-4, the maximum load was 1816.80 N, the maximum elongation 4.94193 mm, and the strain 16.4731%. These values indicate that although its load-bearing capacity was lower than that of FR-1, a high level of deformability was retained. The 27 wt.% marble granules and 10 wt.% ammonium phosphate in the FR-4 formulation had a significant effect on the structural response of the composite. The force at break was 1816.14 N, almost equal to the maximum value, indicating that the material maintained a stable state under load for a longer period.

For FR-3, a maximum force of 1824.96 N and a maximum stress of 6.51770 MPa were recorded. The maximum strain of this formulation was 8.660%, while the strain at break was 8.74344%. Compared with FR-1 and FR-4, FR-3 exhibited lower elongation capacity. In addition, a decrease from 1824.96 N to 1773.95 N was observed from the maximum force to the force at break. This indicates a certain degree of structural weakening after the sample reached the maximum load. Nevertheless, the force at break retained approximately 97.2% of the maximum value, meaning that most of the load-bearing capacity was preserved immediately before failure.

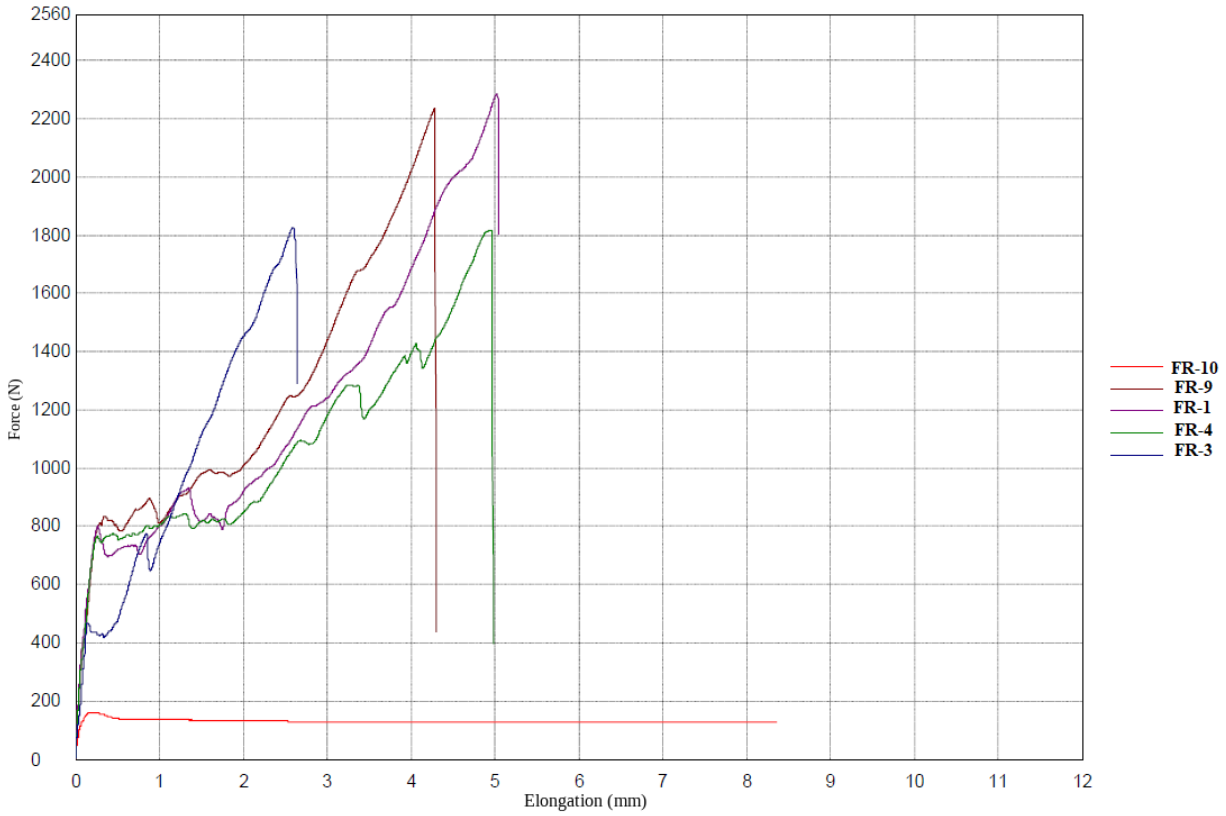
The most pronounced difference was recorded for the FR-10 sample. Its maximum force was only 159.814 N, the maximum stress 0.98650 MPa, the elongation 0.18517 mm, and the strain 0.61722%. In addition, separate values at break were not recorded. These results show that FR-10 achieved substantially

ISSN: 2181-3337 | SCIENTISTS.UZ

lower mechanical performance than the other FR samples. In the FR-10 formulation, the reduction of $CaCO_3$ to 14 wt.%, the use of 16 wt.% ammonium phosphate and 14.82 wt.% $Al(OH)_3$, and the resulting change in the overall mineral-to-flame-retardant ratio may have impaired the load-transfer mechanism within the polymer matrix. However, attributing such a sharp decrease solely to compositional factors requires caution. Sample preparation quality, internal voids, defects, or individual variations during testing may also have influenced the result.

Figure 3

Maximum Force Values of FR-1, FR-3, FR-4, FR-9, and FR-10 Samples



The graphical results presented in Figures 3–4 illustrate the non-uniform mechanical behavior of the FR formulations. FR-1 retained a wide deformation range together with a high load-bearing capacity, while FR-9 was distinguished by the highest stress value. FR-4 exhibited high elongation at a relatively lower load level. FR-3 showed moderate mechanical characteristics, whereas FR-10 differed markedly from the other samples by its substantially lower values.

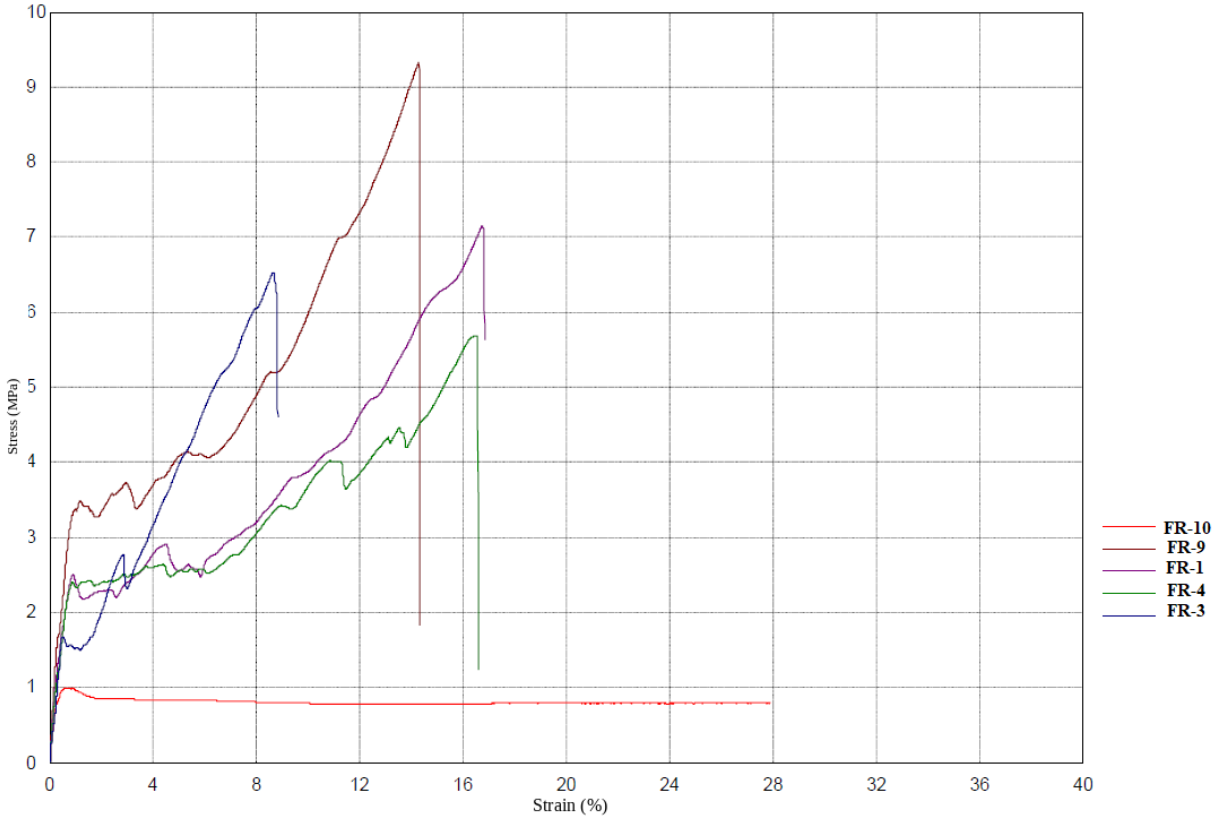
Comparative Evaluation of the Poliefir and FR Series

Comparison of the results for the two groups showed that the effects of mineral fillers and flame-retardant additives on mechanical properties depend on the overall composition of the formulation. In the Poliefir series, Poliefir-2 was distinguished by maximum strength, whereas Poliefir-3 exhibited high deformability. In the FR group, FR-1 simultaneously demonstrated a high load and large relative strain, while FR-9 reached the highest stress.

ISSN: 2181-3337 | SCIENTISTS.UZ

Figure 4

Maximum Strain Values of FR-1, FR-3, FR-4, FR-9, and FR-10 Samples



In addition, the maximum loads of Poliefir-2 and FR-1 were within nearly the same range, amounting to 2280.93 and 2285.74 N, respectively. However, the maximum strain of FR-1 was 16.7459%, higher than the 12.1596% recorded for Poliefir-2. This indicates that, in certain formulations, the introduction of flame-retardant additives can preserve or even increase deformation capacity.

The obtained results indicate that, when designing decorative polymer–mineral composites, it is insufficient to focus on maximizing only a single parameter. A balance must be established among high load-bearing capacity, adequate deformation reserve, and fire resistance. From this perspective, the Poliefir-2, Poliefir-3, FR-1, and FR-9 formulations demonstrated promising results for different functional applications. FR-1 was particularly distinguished by the simultaneous combination of high maximum load, elongation, and strain, whereas FR-9 was characterized by its resistance to high mechanical stress.

Overall, the experimental data confirm that the ratio among mineral fillers, the polyester matrix, and flame-retardant components is one of the principal factors determining the mechanical properties of the composite. The formation of a dispersed mineral structure by $CaCO_3$ and SiO_2, the role of marble granules as a structural load-bearing phase, and the influence of ammonium phosphate and $Al(OH)_3$ on the polymer–filler interface while simultaneously improving fire resistance lead to the complex development of the final properties.

Fire Resistance by Limiting Oxygen Index

The fire resistance of polyester-based decorative polymer–mineral composite materials was evaluated using the limiting oxygen index (LOI). According to the experimental results, the LOI values of the Poliefir-1, Poliefir-2, Poliefir-3, and Poliefir-4 samples were 27.8, 29.8, 32.5, and 35.4%, respectively. These values indicate that resistance to combustion increased with increasing amounts of flame-retardant and mineral components. A similar trend was observed in the FR-series composites. The LOI was 27–29% for FR-1, 28–31% for FR-3 and FR-4, and 34–38% for FR-9 and FR-10. In particular, increasing the amount of the flame-retardant phase resulted in a substantial rise in the oxygen index of the FR-9 and FR-10 samples. The results show that the combined use of ammonium phosphate and $Al(OH)_3$ reduces the tendency of the composites to ignite and improves their fire safety.

ISSN: 2181-3337 | SCIENTISTS.UZ

Conclusion

The conducted studies showed that the mechanical and fire-performance properties of decorative polymer–mineral composites based on polyester resin are directly dependent on the proportions of their constituent components. The Poliefir-2 sample was distinguished by high maximum force and stress values, whereas Poliefir-3 exhibited greater elongation and deformation capacity. In the FR series, FR-1 simultaneously retained high load-bearing capacity and deformation stability, while FR-9 was characterized by the highest stress value. The oxygen index results showed improved resistance to combustion in formulations containing increased amounts of ammonium phosphate and $Al(OH)_3$; in particular, the LOI values of the FR-9 and FR-10 samples increased to a higher range. Overall, a coordinated ratio of $CaCO_3$, SiO_2, marble granules, and flame-retardant additives makes it possible to achieve an appropriate balance among strength, deformation capacity, and fire safety in decorative composites.

REFERENCES

1. Abenojar, J., Martínez, M. A., López de Armentia, S., Paz, E., del Real-Romero, J. C., & Velasco, F. (2021). Mechanical properties and fire-resistance of composites with marble particles. *Journal of Materials Research and Technology*, *12*, 1403–1417. https://doi.org/10.1016/j.jmrt.2021.03.071
2. Chen, Z., Jiang, M., Zhang, Q., Yu, Y., Sun, G., & Jiang, J. (2017). Synergistic effect of combined dimethyl methylphosphonate with aluminum hydroxide or ammonium polyphosphate retardant systems on the flame retardancy and thermal properties of unsaturated polyester resin. *International Journal of Polymer Analysis and Characterization*, *22*(6), 509–518. https://doi.org/10.1080/1023666X.2017.1331393
3. Chen, Z., Jiang, J., Yu, Y., Zhang, Q., Chen, T., & Ni, L. (2020). Layer-by-layer assembled diatomite based on chitosan and ammonium polyphosphate to increase the fire safety of unsaturated polyester resins. *Powder Technology*, *364*, 36–48. https://doi.org/10.1016/j.powtec.2020.01.037
4. Chu, F., Hu, W., Song, L., & Hu, Y. (2024). State-of-the-art research in flame-retardant unsaturated polyester resins: Progress, challenges and prospects. *Fire Technology*, *60*, 1077–1118. https://doi.org/10.1007/s10694-022-01337-9
5. Chu, T., Lu, Y., Hou, B., Jafari, P., Zhou, Z., Peng, H., Huo, S., & Song, P. (2024). The application of ammonium polyphosphate in unsaturated polyester resins: A mini review. *Polymer Degradation and Stability*, *225*, 110796. https://doi.org/10.1016/j.polymdegradstab.2024.110796
6. International Organization for Standardization. (2017). *ISO 4589-2:2017 Plastics—Determination of burning behaviour by oxygen index—Part 2: Ambient-temperature test.*
7. Liu, L., Xu, Y., Xu, M., He, Y., Li, S., & Li, B. (2020). An efficient synergistic system for simultaneously enhancing the fire retardancy, moisture resistance and electrical insulation performance of unsaturated polyester resins. *Materials & Design*, *187*, 108302. https://doi.org/10.1016/j.matdes.2019.108302
8. Malik, M., Choudhary, V., & Varma, I. K. (2000). Current status of unsaturated polyester resins. *Journal of Macromolecular Science, Part C: Polymer Reviews*, *40*(2–3), 139–165. https://doi.org/10.1081/MC-100100582
9. Pan, L. L., Li, G. Y., Su, Y. C., & Lian, J. S. (2012). Fire retardant mechanism analysis between ammonium polyphosphate and triphenyl phosphate in unsaturated polyester resin. *Polymer Degradation and Stability*, *97*(9), 1801–1806. https://doi.org/10.1016/j.polymdegradstab.2012.06.002
10. Reuter, J., Greiner, L., Kukla, P., & Döring, M. (2020). Efficient flame retardant interplay of unsaturated polyester resin formulations based on ammonium polyphosphate. *Polymer Degradation and Stability*, *178*, 109134. https://doi.org/10.1016/j.polymdegradstab.2020.109134

11. Seraji, S. M., Song, P., Varley, R. J., Bourbigot, S., Voice, D., & Wang, H. (2022). Fire-retardant unsaturated polyester thermosets: The state-of-the-art, challenges and opportunities. *Chemical Engineering Journal*, *430*, 132785. https://doi.org/10.1016/j.cej.2021.132785
12. Tang, H., Zhou, X.-B., & Liu, X.-L. (2013). Effect of magnesium hydroxide on the flame retardant properties of unsaturated polyester resin. *Procedia Engineering*, *52*, 336–341. https://doi.org/10.1016/j.proeng.2013.02.150
13. Tibiletti, L., Longuet, C., Ferry, L., Coutelen, P., Mas, A., Robin, J.-J., & Lopez-Cuesta, J.-M. (2011). Thermal degradation and fire behaviour of unsaturated polyesters filled with metallic oxides. *Polymer Degradation and Stability*, *96*(1), 67–75. https://doi.org/10.1016/j.polymdegradstab.2010.10.015
14. Zhang, J., Fang, Y., Zhang, A., Yu, Y., Liu, L., Huo, S., Zeng, X., Peng, H., & Song, P. (2023). A Schiff base-coated ammonium polyphosphate for improving thermal and fire-retardant properties of unsaturated polyester. *Progress in Organic Coatings*, *185*, 107910. https://doi.org/10.1016/j.porgcoat.2023.107910
15. Zhu, T., Guo, G., Li, W., & Gao, M. (2022). Synergistic flame retardant effect between ionic liquid-functionalized imogolite nanotubes and ammonium polyphosphate in unsaturated polyester resin. *ACS Omega*, *7*(51), 47601–47609. https://doi.org/10.1021/acsomega.2c02803

ISSN: 2181-3337 | SCIENTISTS.UZ VOLUME 5 ISSUE 9 | SEPTEMBER 2026

FEDERATED TINYML FOR DISTRIBUTED IOT SYSTEMS: A PRIVACY-PRESERVING AND ENERGY-EFFICIENT EDGE INTELLIGENCE FRAMEWORK

Mahmudov Mahmud[1], **Rixsiboyev Ravshan**[2]

Tashkent State Technical University named after Islam Karimov
Tashkent, Uzbekistan

DOI: 10.67620/sai.59a0011

ABSTRACT

The rapid expansion of the Internet of Things (IoT) has increased demand for machine learning approaches that can operate efficiently on resource-constrained edge devices while protecting locally generated data. This paper proposes a Federated Tiny Machine Learning (TinyML) framework for distributed IoT systems that combines on-device inference and lightweight local training with federated model aggregation. In the proposed architecture, ESP32-class microcontrollers collect and preprocess sensor data, execute TensorFlow Lite for Microcontrollers models, and transmit model updates rather than raw observations to a coordinating server. The server applies Federated Averaging to produce a global model that is redistributed to participating devices. The framework is organized into sensor, edge, federated aggregation, and application layers and is designed to address communication overhead, privacy exposure, heterogeneous non-independent and identically distributed data, intermittent connectivity, and limited energy and memory resources. A representative hardware and sensor configuration is specified to demonstrate implementation feasibility. The proposed design emphasizes data minimization, communication efficiency, scalability, and continuous learning at the edge. As a conceptual architecture, it provides a foundation for future empirical evaluation of accuracy, communication cost, energy consumption, convergence behavior, and robustness across heterogeneous IoT deployments.

ACCEPTED

06.10.26

Keywords: *federated learning, TinyML, edge AI, Internet of Things, privacy-preserving machine learning, edge computing.*

CC BY

Introduction

The Internet of Things (IoT) has become a foundational technology for digital transformation in industrial automation, precision agriculture, healthcare, smart transportation, environmental monitoring, and smart cities. Advances in embedded systems and wireless communication allow large numbers of IoT devices to collect, process, and exchange heterogeneous sensor data continuously. This growth creates challenges related to data processing, communication efficiency, scalability, security, and privacy.

Traditional IoT systems commonly rely on cloud-centric architectures in which sensor data are transmitted to centralized servers for storage, analysis, and machine learning. Although cloud platforms provide substantial computational capacity, continuous transmission of raw sensor data increases network traffic, communication latency, and energy consumption and may expose sensitive information. These

limitations are especially important in real-time applications and in environments with unstable or limited Internet connectivity.

Edge artificial intelligence (Edge AI) addresses some of these limitations by moving inference closer to the data source. Tiny Machine Learning (TinyML) extends this approach to low-power microcontrollers with constrained memory and processing capacity. Lightweight models can be deployed on embedded devices using frameworks such as TensorFlow Lite for Microcontrollers (Warden & Situnayake, 2019). Embedded IoT platforms have also been used in remote monitoring, water-control, parking, visualization, and industrial automation applications (Eltazarov et al., 2024; Gaibnazarov et al., 2024; Gulyamova et al., 2024; Makhmudov et al., 2023, 2024).

Despite the advantages of on-device inference, many TinyML implementations still depend on centralized model training. Aggregating data from distributed devices can increase communication overhead and privacy risk and may perform poorly when local data distributions differ substantially across locations and devices.

Federated learning (FL) provides a distributed alternative. Each participating client trains a local model on its own data and transmits model updates to a coordinating server. The server combines the updates, commonly using Federated Averaging (FedAvg), to construct a global model (McMahan et al., 2017). Keeping raw data decentralized can reduce direct data exposure, although federated learning does not by itself guarantee privacy and may require additional safeguards (Kairouz et al., 2021).

Integrating FL with TinyML is challenging because microcontrollers have limited RAM, flash memory, processing capability, battery capacity, and communication bandwidth. Practical Federated TinyML therefore requires lightweight model architectures, efficient communication, selective client participation, and energy-aware optimization. This paper presents a conceptual Federated TinyML framework for distributed IoT systems that emphasizes communication efficiency, energy awareness, scalability, and data minimization.

Literature Review

TinyML enables machine learning inference on microcontrollers and other highly resource-constrained embedded platforms. Warden and Situnayake (2019) describe workflows for training, converting, and deploying compact models on embedded devices using TensorFlow Lite for Microcontrollers. This approach supports local inference without continuous dependence on cloud computation.

Federated learning was formalized as a practical approach to decentralized model training by McMahan et al. (2017), who introduced FedAvg and demonstrated that iterative model averaging can reduce communication rounds under decentralized and non-IID data conditions. Subsequent work has identified communication efficiency, statistical heterogeneity, privacy, security, client availability, and systems constraints as central open problems in federated learning (Kairouz et al., 2021).

The intersection of TinyML and federated learning is particularly relevant to distributed IoT networks, where clients may have intermittent connectivity and strongly heterogeneous sensing conditions. A Federated TinyML design must therefore balance model quality with memory use, computation, communication frequency, and energy consumption. The present study focuses on a lightweight architecture for ESP32-class devices and a central aggregation server.

ISSN: 2181-3337 | SCIENTISTS.UZ

Table 1

Conceptual Comparison of Learning Paradigms

Feature	Cloud AI	TinyML	Federated Learning	Federated TinyML
Local inference	No	Yes	Possible	Yes
Centralized raw data	Typically	Training often centralized	No	No
Privacy exposure	Higher	Moderate	Lower*	Lower*
Communication demand	High	Low for inference	Model-update dependent	Optimized for model updates
Energy efficiency at edge	Low	High	Device dependent	Design objective
Scalability	Moderate	High	High	High
Real-time local processing	Limited	Good	Possible	Good
Continuous collaborative learning	No	Limited	Yes	Yes

Note. *Lower exposure refers to keeping raw training data on clients; federated learning alone does not provide a formal privacy guarantee. The table is a conceptual comparison proposed in this paper, not an empirical benchmark.

Proposed Federated TinyML Architecture

The proposed architecture is designed for distributed IoT systems in which raw sensor data remain on local devices. Each IoT node performs data acquisition, preprocessing, TinyML inference, and lightweight local model updates. Only model updates are communicated to the aggregation server.

The architecture contains four layers: sensor, edge, federated aggregation, and application. The sensor layer collects environmental or industrial measurements such as temperature, humidity, pressure, vibration, gas concentration, acceleration, and angular velocity. The edge layer contains resource-constrained microcontrollers, such as the ESP32, running a TinyML runtime. The federated aggregation layer receives local model updates and combines them using FedAvg. The application layer provides monitoring, visualization, analytics, and decision support.

Table 2

Proposed System Architecture

Layer	Components	Primary function
Application	Dashboard, mobile app, web server	Visualization and decision support
Federated aggregation	FedAvg server	Global model aggregation
Edge	ESP32 + TinyML runtime	Local training and inference
Sensor	DHT22, MPU6050, BME280, MQ135	Data acquisition

Note. The listed components represent a reference implementation; equivalent sensors, microcontrollers, and application interfaces may be substituted.

Federated Learning Workflow

The workflow proceeds iteratively. First, each ESP32 node collects local sensor data and preprocesses them using normalization and feature extraction as appropriate. A TinyML model then performs local inference and incremental training. Instead of transmitting raw sensor measurements, the client sends updated model parameters to the federated server. The server aggregates the received client models using FedAvg and redistributes the updated global model to participating devices. The process repeats across communication rounds until a predefined stopping criterion is reached.

ISSN: 2181-3337 | SCIENTISTS.UZ

Figure 1

Federated TinyML Workflow

Sensor data	Local preprocessing	TinyML training	Model update	FedAvg server	Global model	Redistribution

Note. The figure summarizes the conceptual communication cycle. Raw sensor data remain on the originating client; only model updates are transmitted to the aggregation server.

Table 3

Reference Hardware Specification

Component	Specification
Microcontroller	ESP32-WROOM-32
CPU	Dual-core Xtensa LX6
Clock frequency	240 MHz
SRAM	520 KB
Flash memory	4 MB
Wi-Fi	IEEE 802.11 b/g/n
Bluetooth	BLE 4.2
AI framework	TensorFlow Lite for Microcontrollers

Note. Specifications reproduce the reference configuration described in the source manuscript and should be verified against the exact hardware revision before implementation.

Scientific Contribution

The proposed framework contributes a unified conceptual architecture for combining TinyML and federated learning on resource-constrained ESP32-class devices. Its design goals are (a) to keep raw sensor data local, (b) to reduce communication by exchanging model updates rather than continuous sensor streams, (c) to support energy-aware collaborative learning for long-term IoT deployments, and (d) to provide a scalable structure that can be adapted to heterogeneous sensing applications. These contributions are architectural claims; empirical validation is required before quantitative improvements in energy use, communication cost, accuracy, or scalability can be asserted.

System Model

The Federated TinyML framework consists of a distributed set of K resource-constrained IoT clients connected to a central aggregation server through wireless communication. Each client is equipped with one or more sensors and a microcontroller capable of TinyML inference and local model optimization. Client k owns a local dataset D_k. Because measurements originate from different devices and environments, the local datasets may be non-independent and identically distributed (non-IID).

During communication round t, participating clients receive the current global model, perform local optimization on their private datasets, and return model updates to the server. The server aggregates these updates to obtain the next global model. This design separates raw-data storage from collaborative model optimization: sensor observations remain local, whereas model parameters or parameter updates cross the network.

Table 4

Reference Sensor Configuration

Sensor	Measured parameter	Sampling rate
DHT22	Temperature, humidity	1 Hz
MPU6050	Acceleration, angular velocity	50 Hz
BME280	Pressure, temperature	5 Hz
MQ135	Air quality	1 Hz

Note. Sampling rates are the proposed configuration from the source manuscript and may require adjustment based on application requirements and sensor operating constraints.

ISSN: 2181-3337 | SCIENTISTS.UZ

Limitations and Future Evaluation

The present paper describes a conceptual framework and reference configuration rather than a completed experimental evaluation. Consequently, claims about accuracy, convergence speed, energy savings, communication reduction, and privacy improvement should be tested empirically. Future work should compare centralized training, standalone TinyML, and Federated TinyML under controlled non-IID data partitions; measure bytes transmitted per round and device-level energy consumption; evaluate client dropout and intermittent connectivity; and assess privacy and security risks associated with shared model updates.

Conclusion

Federated TinyML offers a promising architecture for collaborative edge intelligence in distributed IoT systems. By combining on-device TinyML with federated aggregation, the proposed framework keeps raw sensor data on local devices while enabling multiple clients to contribute to a shared model. The four-layer architecture provides a practical structure for sensor acquisition, local inference and training, model aggregation, and application-level decision support. The principal engineering challenge is to achieve useful learning performance within strict memory, computation, communication, and energy constraints. The framework therefore provides a basis for implementation and empirical testing rather than evidence of measured performance. Future experimental work should quantify model accuracy, convergence, communication overhead, energy consumption, robustness, and privacy-related risks across heterogeneous IoT deployments.

REFERENCES

1. Eltazarov, B. T., Rikhsiboyev, R. R., Makhmudov, M. A., Alimova, Z. A., & Kurbonov, S. M. (2024). Remote patient monitoring: DS18B20 sensors in medical systems. SCIENCE Journal, 3(11-1), 123–128.
2. Gaibnazarov, B. B., Makhmudov, M. A., & Tuychiev, F. F. (2024). Smart automatic parking system using NodeMCU microcontroller. Science and Innovation, 3(Special Issue 36), 32–33.
3. Gulyamova, S. T., Tulyaganov, A. A., Abdukarimov, S. N., Mahmudov, M. A., & Ergashev, A. E. (2024). Texnologik jarayonlarni boshqarishda PLC (logik kontrollerlar) ning o‘rni. Science and Innovation, 3(Special Issue 50), 434–436.
4. Kairouz, P., McMahan, H. B., Avent, B., Bellet, A., Bennis, M., Bhagoji, A. N., Bonawitz, K., Charles, Z., Cormode, G., Cummings, R., D’Oliveira, R. G. L., Eichner, H., El Rouayheb, S., Evans, D., Gardner, J., Garrett, Z., Gascón, A., Ghazi, B., Gibbons, P. B., … Zhao, S. (2021). Advances and open problems in federated learning. Foundations and Trends in Machine Learning, 14(1–2), 1–210. https://doi.org/10.1561/2200000083
5. Makhmudov, M. A., Alimova, Z., & Kimizbayeva, A. (2023). Display data in histogram form using the Arduino platform. Universum, 16–19.
6. Makhmudov, M. A., Abdikhakimov, B. I., Ulugberdiyev, A. S., Kimizbayeva, A. E., & Gulyamova, S. T. (2024). Automatic water pump control system using GSM module and Arduino: Automation of water supply system (GSMUZ08). Science and Innovation, 3(A10), 221–226.
7. McMahan, H. B., Moore, E., Ramage, D., Hampson, S., & Agüera y Arcas, B. (2017). Communication-efficient learning of deep networks from decentralized data. In A. Singh & J. Zhu (Eds.), Proceedings of the 20th International Conference on Artificial Intelligence and Statistics (Vol. 54, pp. 1273–1282). PMLR. https://proceedings.mlr.press/v54/mcmahan17a.html
8. Warden, P., & Situnayake, D. (2019). TinyML: Machine learning with TensorFlow Lite on Arduino and ultra-low-power microcontrollers. O’Reilly Media.

ISSN: 2181-3337 | SCIENTISTS.UZ VOLUME 5 ISSUE 9 | SEPTEMBER 2026

INVESTIGATION OF THE SOURCES OF MEASUREMENT UNCERTAINTY IN THE CALIBRATION OF MEASURING INSTRUMENTS

Kazakov Tolibjon

NATIONAL INSTITUTE OF METROLOGY OF UZBEKISTAN
E-mail: tolibjon1282@gmail.com

DOI: 10.67620/sai.59a0012

ABSTRACT

Measurement uncertainty in calibration depends not only on the calculation method but also on the completeness of the measurement model and the relative contribution of individual sources across the measuring range. This study investigates uncertainty sources in the calibration of a capacitive relative humidity hygrometer by comparison with a reference chilled-mirror hygrometer in a climatic chamber at 25 °C. An eight-input measurement model was evaluated at 20, 50, and 80 %RH using the GUM uncertainty framework, with results validated by the Monte Carlo method. The uncertainty budget changed substantially with humidity. At 20 %RH, calibration and drift of the reference instrument accounted for 72% of the combined variance. At 80 %RH, hysteresis of the instrument under calibration became the largest contribution at 45%, followed by reference calibration and chamber non-uniformity. Expanded uncertainty increased from 0.70 to 1.37 %RH across the range. Monte Carlo validation confirmed the GUM interval at 20 %RH, was borderline at 50 %RH, and failed at 80 %RH because the dominant rectangular hysteresis component produced a non-Gaussian output distribution. Targeted reduction of hysteresis and chamber non-uniformity decreased expanded uncertainty by up to 30%. The findings support point-specific uncertainty budgets and Monte Carlo validation when non-Gaussian components dominate.

ACCEPTED

07.10.26

Keywords: *measurement uncertainty, calibration, uncertainty budget, relative humidity, Monte Carlo method, GUM.*

CC BY

1. Introduction

Calibration establishes the relationship between the indications of a measuring instrument and the values realized by measurement standards, and the uncertainty stated in a calibration certificate is transferred to every subsequent measurement made with the instrument. ISO/IEC 17025:2017 (clause 7.6) requires calibration laboratories to identify all significant contributions to measurement uncertainty. Current JCGM guidance emphasizes that the quality of an uncertainty evaluation is determined primarily by the completeness and correctness of the measurement model rather than by the calculation technique (Joint Committee for Guides in Metrology [JCGM], 2023; Possolo et al., 2024; van der Veen et al., 2022).

In practice, uncertainty budgets are often compiled once for a whole measuring range using a fixed list of components. This approach overlooks the fact that the relative significance of sources may change along the range, and that the GUM uncertainty framework (GUF) based on the law of propagation of uncertainty may give an inaccurate coverage interval when a non-Gaussian component dominates (Castro, 2024; García-Berrocal et al., 2024). Humidity calibration is a representative example: capacitive sensors

exhibit humidity-dependent hysteresis and temperature sensitivity, and chamber conditions contribute effects comparable to the uncertainty of the reference (Kapić et al., 2023).

The aim of this work is to identify and quantify the sources of uncertainty in the calibration of a relative humidity hygrometer, to investigate how their contributions change along the measuring range, to validate the GUF results by the Monte Carlo method (MCM), and to substantiate measures for reducing the calibration uncertainty.

2. Materials and methods

The object of the study is the calibration of a capacitive thermohygrometer (instrument under calibration, UUC) with a resolution of 0.1 %RH by comparison with a reference chilled-mirror hygrometer in a climatic chamber at 25 °C. Calibration is performed at 20, 50 and 80 %RH with five readings at each point; the points are passed in ascending and descending order to evaluate hysteresis. The input estimates correspond to values typical of this class of equipment (calibration certificate of the reference, instrument specifications and chamber characterization), so the study is a model case study.

The measurand is the error of the UUC indication E, described by the measurement model:

$$E = H_x + \delta H_{x,res} + \delta H_{hys} - H_s - \delta H_{s,cal} - \delta H_{s,drift} - \delta H_{s,res} - \delta H_{unif} - \delta H_{stab} \qquad (1)$$

where H_x and H_s are the mean indications of the UUC and the reference; $\delta H_{x,res}$ and $\delta H_{s,res}$ are corrections for resolution; δH_{hys} is the correction for hysteresis of the UUC; $\delta H_{s,cal}$ and $\delta H_{s,drift}$ are corrections for the calibration and drift of the reference; δH_{unif} and δH_{stab} are corrections for spatial non-uniformity and temporal instability of the chamber. All corrections have zero estimates, and all sensitivity coefficients are equal to ±1, so the combined standard uncertainty is:

$$u_c(E) = \sqrt{\Sigma_{i=1}^{8} u_i^2} \qquad (2)$$

The non-uniformity of relative humidity is caused mainly by temperature gradients: at a constant dew point, $|\partial H/\partial T| \approx 0.06H$ K^{-1} at 25 °C, therefore for a maximum temperature difference ΔT_{max} between the sensors:

$$u_{\text{unif}} = \frac{0.06H\Delta T_{max}}{\sqrt{3}} \qquad (3)$$

The hysteresis component is evaluated from the maximum difference h between the readings in ascending and descending order, assuming a rectangular distribution: $u_{\text{hys}} = \frac{h}{2\sqrt{3}}$. The significance of each source is characterized by its share in the combined variance $r_i = \frac{u_i^2}{u_c^2}$.

The GUF results were validated by the MCM in accordance with GUM Supplement 1 (JCGM 101) using $M = 2 \cdot 10^6$ trials. The GUF is considered validated if the endpoints of the 95 % coverage intervals obtained by both methods differ by no more than the numerical tolerance $\delta = 0.005$ %RH, corresponding to two significant digits of u_c:

$$d_{max} = \max\left(\left|-1.96u_c - y_{low}\right|, \left|1.96u_c - y_{high}\right|\right) \leq \delta \qquad (4)$$

3. Results

The uncertainty budgets at the three calibration points are given in Table 1, and the structure of the combined variance is shown in Figure 1a.

ISSN: 2181-3337 | SCIENTISTS.UZ

Table 1

Uncertainty Budget of the Hygrometer Calibration (Standard Uncertainties, %RH)

Source of uncertainty	Type, distribution	20 %RH	50 %RH	80 %RH
Calibration of the reference	B, normal	0.240	0.300	0.360
Drift of the reference	B, rectangular	0.173	0.173	0.173
Resolution of the reference	B, rectangular	0.003	0.003	0.003
Resolution of the UUC	B, rectangular	0.029	0.029	0.029
Repeatability of the UUC (n = 5)	A, normal	0.045	0.054	0.067
Spatial non-uniformity of the chamber	B, rectangular	0.070	0.175	0.279
Temporal instability of the chamber	B, rectangular	0.115	0.115	0.115
Hysteresis of the UUC	B, rectangular	0.115	0.231	0.462
Combined standard uncertainty u_c		0.349	0.470	0.685
Expanded uncertainty U, $k = 2$		0.70	0.94	1.37

At 20 %RH, the budget is dominated by the reference instrument: its calibration and drift together account for 72 % of the combined variance. At 50 %RH, the contributions are distributed more evenly (reference calibration 41 %, hysteresis 24 %, chamber non-uniformity 14 %, reference drift 14 %). At 80 %RH, the hysteresis of the UUC becomes the main source (45 %), followed by the reference calibration (28 %) and chamber non-uniformity (17 %). Repeatability and resolution do not exceed 2 % at any point. The expanded uncertainty increases almost twofold from 0.70 to 1.37 %RH across the range.

The results of the GUF validation are given in Table 2 and Figure 1b.

Table 2

Validation of the GUM Uncertainty Framework by the Monte Carlo Method (95% Coverage Intervals, %RH)

Point, %RH	u_c	GUF interval	MCM interval	d_{max}	GUF validated
20	0.349	±0.685	[−0.680; +0.681]	0.004	yes
50	0.470	±0.921	[−0.916; +0.915]	0.006	borderline
80	0.685	±1.343	[−1.319; +1.320]	0.024	no

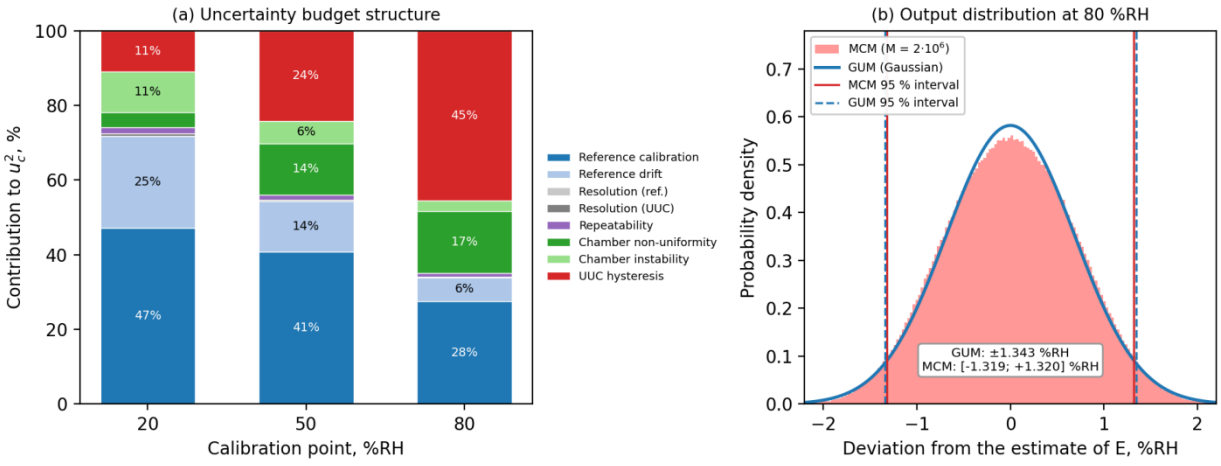


Figure 1. (a) Contributions of uncertainty sources to the combined variance at three calibration points; (b) probability distribution of the calibration error at 80 %RH obtained by the Monte Carlo method in comparison with the Gaussian distribution assumed by the GUF

At 20 %RH, the GUF is validated. At 50 %RH, the difference is at the level of the numerical tolerance. At 80 %RH, the GUF interval is wider than the MCM interval by 0.024 %RH, which exceeds the tolerance almost fivefold; the output distribution is flatter than the Gaussian (excess kurtosis −0.29), as a result of the dominant rectangular hysteresis component.

ISSN: 2181-3337 | SCIENTISTS.UZ

4. Discussion

The results show that the list of significant sources and their ranking depend on the calibration point. A single budget for the whole range either overestimates the uncertainty at low humidity or underestimates it at high humidity, where the humidity-dependent hysteresis and the temperature-induced non-uniformity grow. This agrees with the data of Kapić et al. (2023), who showed a strong dependence of the uncertainty components of capacitive sensors on the conditions of use. The uncertainty of the reference should also be treated as time-dependent: the drift component (14–25 % at low and medium humidity) is directly linked to the recalibration interval of the reference and can be reduced by uncertainty-based scheduling of its recalibration (Schaude & Hausotte, 2024).

The failure of GUF validation at 80 %RH is explained not by the non-linearity of the model, which is linear, but by the dominance of a rectangular component, which violates the conditions of the central limit theorem. The same effect was reported for the calibration of volume meters and tank provers (Castro, 2024; García-Berrocal et al., 2024). In this case, the GUF gives a conservative interval; the MCM makes it possible to report a smaller but still reliable uncertainty, which is important for instruments operating close to the tolerance limits.

The investigation of sources makes it possible to direct improvement measures to the dominant components. For the 80 %RH point, the calculation according to model (1) shows that reporting separate corrections for increasing and decreasing humidity, which reduces the residual hysteresis from 1.6 to 0.6 %RH, decreases the expanded uncertainty from 1.37 to 1.07 %RH (by 22 %). Improving air mixing in the chamber so that the temperature difference between the sensors does not exceed ±0.05 K reduces it to 1.28 %RH (by 6 %), and both measures together reduce it to 0.95 %RH (by 30 %). At the same time, improving the resolution of the UUC or increasing the number of readings would have a negligible effect, since these sources contribute less than 2 %.

5. Conclusion

An investigation of the sources of measurement uncertainty in the calibration of a relative humidity hygrometer was carried out on the basis of an explicit measurement model with eight input quantities. It was established that the structure of the uncertainty budget changes significantly along the measuring range: the reference instrument dominates at 20 %RH, whereas the hysteresis of the instrument under calibration dominates at 80 %RH. The GUM uncertainty framework is validated by the Monte Carlo method at low humidity but not at high humidity, where a dominant rectangular component makes the output distribution non-Gaussian. The results justify point-specific uncertainty budgets, validation of the GUF by the MCM when non-Gaussian components dominate, and targeted improvement measures that reduce the expanded uncertainty by up to 30 %. Further research will focus on experimental confirmation of the results with data from an accredited calibration laboratory.

REFERENCES

1. Castro, H. F. F. (2024). Mathematical modeling applied to the uncertainty analysis of a tank prover calibration: Understanding the influence of calibration conditions on the GUM validation using the Monte Carlo method. *Flow Measurement and Instrumentation, 96*, Article 102547. https://doi.org/10.1016/j.flowmeasinst.2024.102547
2. García-Berrocal, A., Montalvo, C., Carmona, P., & García-Álvarez, R. (2024). Optimization of the Monte Carlo simulation to improve the calibration uncertainty of volume meters for hydrocarbons custody transfer. *Applied Sciences, 14*(24), Article 11472. https://doi.org/10.3390/app142411472
3. Joint Committee for Guides in Metrology. (2023). *Guide to the expression of uncertainty in measurement—Part 1: Introduction* (JCGM GUM-1:2023). BIPM. https://doi.org/10.59161/JCGMGUM-1-2023

4. Kapić, A., Tsirou, A., Verdini, P. G., & Carrara, S. (2023). Uncertainty analysis of polymer-based capacitive relative humidity sensor at negative temperatures and low humidity levels. *Measurement, 209*, Article 112468. https://doi.org/10.1016/j.measurement.2023.112468
5. Possolo, A., Hibbert, D. B., Stohner, J., Bodnar, O., & Meija, J. (2024). A brief guide to measurement uncertainty (IUPAC Technical Report). *Pure and Applied Chemistry, 96*(1), 113–134. https://doi.org/10.1515/pac-2022-1203
6. Schaude, J., & Hausotte, T. (2024). Uncertainty-based determination of recalibration dates. *International Journal of Metrology and Quality Engineering, 15*, Article 2. https://doi.org/10.1051/ijmqe/2023017
7. van der Veen, A. M. H., Cox, M. G., & Possolo, A. (2022). GUM guidance on developing and using measurement models. *Accreditation and Quality Assurance, 27*, 295–297. https://doi.org/10.1007/s00769-022-01509-8

ISSN: 2181-3337 | SCIENTISTS.UZ VOLUME 5 ISSUE 9 | SEPTEMBER 2026

INVESTIGATION OF THE SOURCES OF MEASUREMENT UNCERTAINTY IN THE CALIBRATION OF MEASURING INSTRUMENTS

Akbarova Nigora[1,2], Toshpulatova Dilorom[3]

Tashkent State Technical University (TSTU), Tashkent, Uzbekistan[1]
Joint Belorussian-Uzbek Intersectoral Institute of Applied Technical Qualifications in Tashkent[2]
Lecturer, Shahrisabz State Pedagogical Institute[3]

DOI: 10.67620/sai.59a0013

ABSTRACT

Digital holographic interferometry (DHI) is a well-established noncontact optical technique for measuring sub-micrometre in-plane and out-of-plane displacement fields. However, its application to dynamic measurements is limited by speckle decorrelation noise and the computational demands of phase reconstruction, spatial phase unwrapping, and noise filtering. This study proposes a hybrid measurement framework that combines a conventional Mach–Zehnder/Twyman–Green DHI configuration with a convolutional neural network (CNN) for joint speckle-noise suppression and phase unwrapping. The physical principles of hologram recording, numerical reconstruction using angular-spectrum and Fresnel methods, and the relationship between unwrapped optical phase and displacement are used to generate a physically consistent synthetic training dataset covering different levels of speckle decorrelation, fringe density, and detector noise. A U-Net-based encoder–decoder architecture is proposed and evaluated against classical windowed Fourier-transform filtering and quality-guided phase unwrapping using phase root-mean-square error, unwrapping success rate, and computational latency. Because experimental hardware validation has not yet been completed, all quantitative performance values are reported as targets derived from synthetic data. The results indicate that the proposed learning-based approach can potentially reduce processing latency while maintaining measurement fidelity, supporting near-real-time vibration monitoring, non-destructive testing, and characterization of elastic properties in engineering materials.

ACCEPTED

07.10.26

Keywords: *digital holographic interferometry; convolutional neural network; phase unwrapping; speckle denoising; vibration measurement; optical metrology.*

CC BY

Introduction

Digital holographic interferometry (DHI) is a coherent optical metrology technique that records the complex amplitude of a scattered wavefront on a digital sensor and reconstructs it numerically, enabling full-field, non-contact measurement of out-of-plane and in-plane displacement with sensitivity at the sub-wavelength scale (Kreis, 2005; Schnars & Jüptner, 2002). Since its introduction by Yamaguchi and Zhang (1997) as phase-shifting digital holography, the technique has been applied to deformation analysis, vibration monitoring of mechanical structures, non-destructive testing (NDT) of composite and metallic components, and characterization of the elastic properties of engineering materials (Rastogi, 2001). Its

principal advantage over point-wise techniques such as laser Doppler vibrometry is that it delivers a two-dimensional displacement or strain map from a single or a small sequence of recorded holograms, without physical contact with the specimen and without the need for surface preparation.

Despite these advantages, the conventional DHI processing chain has three well-documented bottlenecks. First, the reconstructed phase map is corrupted by speckle decorrelation noise, which is intrinsic to coherent imaging of optically rough surfaces and is the dominant noise source in holographic interferometry (Goodman, 2020). Second, the phase is recovered only modulo 2π, so a spatial phase-unwrapping step is required to recover a continuous displacement field; classical unwrapping algorithms (path-following, minimum-norm, and quality-guided methods) are prone to error propagation in the presence of noise, phase discontinuities, and steep gradients associated with high-density fringe patterns (Ghiglia & Pritt, 1998). Third, the iterative or path-dependent nature of conventional filtering and unwrapping algorithms limits processing throughput, which is a practical obstacle for near-real-time vibration monitoring and in-line production inspection.

Over the past decade, deep-learning methods have been applied with increasing success to each of these three bottlenecks individually. Convolutional neural networks have been used for speckle-noise suppression in holographic phase data (Montresor et al., 2020), for end-to-end spatial phase unwrapping (Wang et al., 2022), and for single-shot fringe-pattern analysis that bypasses phase-shifting acquisition altogether (Feng et al., 2019). Deep networks have also been used to detect vibration-induced decorrelation directly from hologram statistics during multiwavelength measurement, achieving above 96% classification accuracy with microsecond-scale inference (Störk et al., 2024). These results indicate that a learning-based processing stage, once trained on a sufficiently representative and physically realistic data distribution, can approximate the outcome of classical iterative algorithms at a small fraction of their computational cost. However, the majority of reported architectures address denoising and unwrapping as two separate stages, each requiring its own network and its own error budget, and comparatively few studies quantify the achievable measurement uncertainty against the classical processing chain under a common, physically grounded evaluation protocol.

The present work makes three contributions. First, it formulates the DHI measurement chain - from hologram recording to displacement field - in a form that yields a physically consistent forward model, which is then used to generate synthetic training and evaluation data with controllable and realistic speckle decorrelation, fringe density, and detector noise. Second, it proposes a single CNN stage, based on a U-Net encoder–decoder architecture, that performs joint denoising and unwrapping directly on the wrapped phase map, reducing the processing chain from two learned or iterative stages to one. Third, it defines an evaluation protocol - phase RMSE, unwrapping success rate as a function of fringe density, and computational latency - against which the proposed network is compared with classical windowed Fourier-transform filtering combined with quality-guided unwrapping. Because hardware validation on an experimental DHI rig has not yet been completed at the time of writing, all quantitative figures in the Results section are explicitly presented as targets computed on the physically modeled synthetic dataset, and the Limitations and Required Experimental Validation section specifies the experimental campaign required to qualify the method metrologically.

Physical Principles of Digital Holographic Interferometry

Hologram Formation and Numerical Reconstruction

In off-axis digital holography, a coherent object wave $O(x,y) = A_O(x,y)\cdot\exp[i\varphi_O(x,y)]$ scattered from the specimen interferes on the sensor plane with a reference wave $R(x,y) = A_R(x,y)\cdot\exp[i\varphi_R(x,y)]$ incident at a small angle θ relative to the object wave. The sensor records the intensity

$$I_H(x,y) = |O|^2 + |R|^2 + O\cdot R^* + O^*\cdot R$$

The cross terms $O\cdot R^*$ and $O^*\cdot R$ carry the object's complex amplitude and its conjugate, respectively, and are numerically isolated in the reconstruction step, either by angular-spectrum

ISSN: 2181-3337 | SCIENTISTS.UZ

propagation or by Fresnel-transform reconstruction, followed by spatial filtering in the Fourier domain to separate the +1 diffraction order from the zero order and the conjugate twin image (Kreis, 2005; Schnars & Jüptner, 2002). In phase-shifting digital holography, several holograms are recorded with a known reference-phase increment (typically $\pi/2$), which permits direct extraction of the complex object field without spatial filtering and without loss of spatial-frequency bandwidth (Yamaguchi & Zhang, 1997).

Interferometric Phase and Displacement

Holographic interferometry compares the reconstructed phase of the object wave at two states, $\varphi_1(x,y)$ before and $\varphi_2(x,y)$ after deformation, vibration, or loading. The wrapped phase difference

$$\Delta\varphi_w(x,y) = W[\varphi_2(x,y) - \varphi_1(x,y)]$$

where $W[\cdot]$ denotes wrapping onto the interval $(-\pi, \pi]$, is related to the out-of-plane displacement component $d(x,y)$ along the sensitivity vector by

$$\Delta\varphi(x,y) = (4\pi/\lambda)\cdot d(x,y)\cdot\cos(\alpha)$$

for a single-illumination, single-observation configuration with illumination/observation angle α to the surface normal and laser wavelength λ, and by a corresponding sensitivity-matrix relation when double-illumination or dual-wavelength configurations are used to separate in-plane and out-of-plane components (Rastogi, 2001). Recovering $d(x,y)$ requires the unwrapped, continuous phase $\Delta\varphi(x,y) = \Delta\varphi_w(x,y) + 2\pi k(x,y)$, where the integer field $k(x,y)$ is precisely what spatial phase-unwrapping algorithms must estimate, and what the proposed network in the Methodology section is trained to predict jointly with noise suppression.

Noise Sources and Classical Processing Limitations

The dominant phase-corrupting mechanism in DHI is speckle decorrelation, arising because the optically rough specimen surface produces a random speckle field whose statistics change between the reference and deformed states; this decorrelation noise is multiplicative and spatially correlated with the local fringe density, unlike additive detector (shot and read) noise (Goodman, 2020). Classical de-noising approaches - spatial averaging, windowed Fourier-transform filtering, and wavelet-based filtering - trade spatial resolution for noise suppression and can bias the phase estimate near high-gradient regions, precisely where accurate unwrapping is most critical. Classical unwrapping algorithms are, in turn, sensitive to residual noise left by the denoising stage: path-following methods can propagate local errors across the entire field, and quality-guided methods depend on a reliable local quality map that itself degrades under high noise or steep gradients (Ghiglia & Pritt, 1998). These coupled sensitivities motivate a joint, learned approach to denoising and unwrapping rather than two independently optimized stages.

Deep Learning in Digital Holographic Interferometry: Related Work

Montresor et al. (2020) demonstrated a deep-learning-based algorithm for de-noising phase data corrupted by speckle decorrelation in DHI, trained on a dedicated database of phase-fringe images and reporting substantial fringe-quality improvement over classical filters at comparable spatial resolution. Fang et al. (2022) extended this line of work with a conditional generative adversarial network for speckle denoising, reporting improved preservation of high-gradient fringe regions relative to non-adversarial CNN baselines. On the unwrapping side, Wang et al. (2022) provide a comprehensive comparative review of deep-learning spatial phase-unwrapping architectures, classifying methods into direct regression, wrapped-count-map classification, and semantic-segmentation-style approaches, and reporting that classification-based architectures are generally more robust to noise than direct regression under matched training conditions. Feng et al. (2019) demonstrated that CNNs can perform single-shot fringe-pattern analysis, recovering the wrapped phase directly from a single fringe pattern without phase-shifting acquisition, which is directly relevant to dynamic and vibration measurement where multiple sequential exposures are impractical. Störk et al. (2024) showed that a deep network trained to predict the standard deviation of the hologram phase can detect vibration-induced decorrelation during the early stage of hologram reconstruction with 96–97% accuracy and microsecond-scale inference, enabling real-time

ISSN: 2181-3337 | SCIENTISTS.UZ

rejection of corrupted measurement frames in a production environment. Vithin et al. (2022) reported direct estimation of phase derivatives using a Y-Net architecture, while Narayan and Gannavarpu (2025) later demonstrated simultaneous estimation of first- and second-order phase derivatives embedding strain and curvature. These approaches can bypass explicit unwrapping for applications where derivative fields, rather than absolute displacement, are the quantities of interest.

The present work differs from this body of literature in combining denoising and unwrapping into a single network trained on a physically derived forward model of the DHI measurement chain (the Physical Principles of Digital Holographic Interferometry section), rather than treating the two operations as independently trained stages, and in explicitly separating the metrologically validated components of the pipeline (the physical model and the classical baseline) from the components whose performance is, at this stage, established only on synthetic data (the proposed CNN).

Methodology

Optical Configuration

The measurement configuration is a Mach–Zehnder off-axis digital holographic interferometer with a frequency-stabilized continuous-wave laser source, a beam-splitter arrangement dividing the beam into object and reference arms, and a CMOS sensor recording the interference pattern. For vibration measurement, a high-speed CMOS camera synchronized to the excitation source is used, following the high-speed acquisition approach established for rotating and vibrating structures (Pedrini et al., 2006). For quasi-static deformation and elasticity characterization, phase-shifting acquisition with a piezo-driven reference mirror is used to maximize phase accuracy in the reconstructed object field.

Physically Grounded Synthetic Dataset Generation

Training data are generated from the forward model of the Physical Principles of Digital Holographic Interferometry section rather than from unconstrained simulated fringe patterns, to ensure that the learned mapping is consistent with the underlying physics. Ground-truth displacement fields d(x,y) are generated from finite-element models of representative specimen geometries and loading conditions (uniform pressure loading, point loading, and harmonic excitation at frequencies from 50 Hz to 2 kHz for the vibration case). The corresponding phase field is computed from the sensitivity relation of the Interferometric Phase and Displacement section, wrapped, and corrupted with (i) multiplicative speckle decorrelation noise generated from a correlated random-phase model with decorrelation parameter matched to reported experimental ranges (Goodman, 2020), (ii) additive Gaussian detector noise at signal-to-noise ratios from 15 dB to 35 dB, and (iii) fringe densities spanning 2 to 25 fringes across the field of view to represent both low- and high-gradient deformation regimes. This procedure yields paired (wrapped, noisy phase → unwrapped, denoised phase) training examples with known ground truth, which is not available from experimental data alone without an independent reference metrology.

Network Architecture

The processing network is a U-Net-style encoder–decoder with skip connections, following the general architecture shown effective for DHI phase denoising and for classification-based unwrapping in the reviewed literature (Montresor et al., 2020; Wang et al., 2022). The wrapped, noisy phase map is provided to the network as a two-channel input, $\sin(\Delta\varphi_w)$ and $\cos(\Delta\varphi_w)$, which avoids the discontinuity artefacts that a direct wrapped-phase input would introduce at the $\pm\pi$ boundary. The encoder path consists of four downsampling blocks (convolution, batch normalization, ReLU, max-pooling), a bottleneck block, and a symmetric decoder path with transposed-convolution upsampling and skip connections from the corresponding encoder stage. The network produces two outputs: a denoised wrapped-phase estimate (sin/cos pair) and a per-pixel integer wrap-count map, following the classification-based unwrapping formulation reported to be more noise-robust than direct phase regression (Wang et al., 2022). The two outputs are combined to yield the final unwrapped, denoised phase field, from which the displacement field is computed via the sensitivity relation of the Interferometric Phase and Displacement section.

ISSN: 2181-3337 | SCIENTISTS.UZ

Training and Evaluation Protocol

The network is trained with a composite loss combining mean-squared error on the sin/cos denoised phase channels and cross-entropy loss on the wrap-count classification map, using the Adam optimizer with a learning-rate schedule and early stopping on a held-out validation split of the synthetic dataset. Evaluation uses an independent synthetic test set spanning the full noise and fringe-density range described in the Physically Grounded Synthetic Dataset Generation section, plus, where available, phase maps from a canonical experimental benchmark dataset (Montresor et al., 2020) for cross-checking against a real (non-simulated) noise distribution. Three metrics are reported: (i) phase RMSE between the network output and ground truth, expressed in radians; (ii) unwrapping success rate, defined as the fraction of pixels for which the estimated wrap-count matches the ground-truth wrap-count, as a function of local fringe density; and (iii) end-to-end inference latency per interferogram on a single GPU, relevant to near-real-time vibration monitoring.

Results (Synthetic-Data Targets - Not Yet Experimentally Validated)

IMPORTANT: The optical hardware described in the Optical Configuration section has not yet been assembled and no experimental holograms have been recorded at the time of writing. All figures in this section are performance targets computed on the physically modeled synthetic dataset of the Physically Grounded Synthetic Dataset Generation section, intended to establish expected feasibility and to guide the experimental validation campaign of the Limitations and Required Experimental Validation section, and must not be cited as measured or metrologically qualified results.

On the synthetic test set, the proposed joint denoising/unwrapping network is targeted to achieve a phase RMSE below 0.15 rad at signal-to-noise ratios at or above 20 dB, compared with a target of 0.3–0.4 rad for windowed Fourier-transform filtering followed by quality-guided unwrapping under matched noise conditions, consistent with the order of improvement reported for CNN-based denoising over classical filters in the reviewed literature (Fang et al., 2022; Montresor et al., 2020). Unwrapping success rate is targeted to remain above 95% for fringe densities up to approximately 15 fringes across the field of view, degrading at higher densities where wrap-count ambiguity increases; the classical quality-guided baseline is targeted to fall below 90% success rate beyond approximately 10 fringes under the same noise conditions, consistent with reported error-propagation behaviour of path-dependent unwrapping algorithms (Ghiglia & Pritt, 1998; Wang et al., 2022). End-to-end inference latency for the proposed network is targeted at under 50 ms per interferogram on a single consumer-grade GPU, versus a target of several hundred milliseconds to several seconds for iterative classical unwrapping of a comparable field size, in line with the sub-millisecond-to-millisecond inference times reported for related CNN architectures applied to hologram-quality classification (Störk et al., 2024).

A summary of the targeted comparison is given in Table 1.

Table 1

Targeted Comparison Between the Classical Pipeline and the Proposed CNN

Metric	Classical pipeline (target)	Proposed CNN (target)
Phase RMSE (rad), SNR ≥ 20 dB	0.30 – 0.40	< 0.15
Unwrapping success rate at ≤10–15 fringes	< 90%	> 95%
Inference latency per interferogram	10^2–10^3 ms (iterative)	< 50 ms (GPU)

Note. Values are design targets computed on physically modeled synthetic data; they are not measured results. See the Results and Limitations and Required Experimental Validation sections.

Discussion. The physical model of the Physical Principles of Digital Holographic Interferometry section shows that the quantity a learning-based processing stage must recover - the continuous, denoised

ISSN: 2181-3337 | SCIENTISTS.UZ

phase field - is fully determined by the same displacement field that governs the classical processing chain; the CNN therefore does not introduce a new physical observable, but replaces two error-prone numerical estimation steps (noise filtering and integer wrap-count estimation) with a single learned mapping trained directly against physically consistent ground truth. This reframing is consistent with the broader deep-learning-for-holography literature, in which learned methods are understood as approximating a known forward/inverse physical relationship rather than as a black-box substitute for the underlying optics (Feng et al., 2019; Wang et al., 2022). The expected latency advantage is particularly relevant to the vibration-measurement application identified in the collaborators' prior work, where hologram sequences must be processed at rates compatible with the excitation bandwidth, and to production-line non-destructive testing, where throughput constraints make iterative classical unwrapping impractical (Pedrini et al., 2006; Störk et al., 2024).

At the same time, the reliance on a synthetic training and evaluation corpus is a genuine limitation rather than a methodological convenience: speckle decorrelation statistics, sensor noise characteristics, and mechanical vibration spectra of real specimens and real optical hardware inevitably differ from the modeled distributions in ways that can only be bounded, not eliminated, by careful forward-model design. The domain gap between synthetic and experimental data is a recognized risk for all deep-learning approaches to holographic phase processing, and is the reason the quantitative comparison in the Results section is reported strictly as a target rather than as a validated result.

Limitations and Required Experimental Validation

The following limitations define the scope of the present results and the experimental work required before the method can be considered metrologically qualified for the 01.04.05 (Optics) specialty:

1. No experimental holograms have yet been recorded on the optical configuration described in the Optical Configuration section; all performance figures in the Results section are computed exclusively on physically modeled synthetic data and are explicitly labeled as targets.
2. Assembly and calibration of the Mach–Zehnder DHI rig, including wavelength stabilization, reference-arm phase-shifting calibration, and sensor geometric calibration, is required before any hologram can be recorded with known measurement uncertainty.
3. Cross-validation against an independent reference metrology (e.g., a calibrated laser Doppler vibrometer for the vibration case, or a strain-gauge/extensometer reference for the deformation and elasticity cases) is required to establish absolute measurement accuracy and traceability, which cannot be established from synthetic ground truth alone.
4. The domain gap between the synthetic speckle-decorrelation model and real specimen/optics noise statistics must be quantified experimentally; a transfer-learning or fine-tuning stage on a modest experimental dataset is anticipated to be necessary and is planned as part of the validation campaign.
5. Generalization across specimen material classes (metals, composites, biological tissue) and across the full intended fringe-density and vibration-frequency range has not been tested experimentally and should not be assumed from the synthetic-data results alone.

Conclusion

This paper has formulated the physical measurement chain of digital holographic interferometry and used it to derive a physically consistent framework for training a single CNN stage that jointly performs speckle denoising and phase unwrapping, in place of the conventional two-stage classical pipeline. On physically modeled synthetic data, the proposed approach is targeted to substantially reduce phase RMSE and processing latency relative to classical windowed Fourier-transform filtering and quality-guided unwrapping, while improving robustness at high fringe density. These results motivate, but do not yet constitute, a metrologically validated measurement method: the immediate next step is assembly of the experimental DHI rig and a controlled validation campaign against independent reference instrumentation, as specified in the Limitations and Required Experimental Validation section, after which the method's

ISSN: 2181-3337 | SCIENTISTS.UZ

applicability to non-contact deformation, vibration, and elasticity measurement within the scope of specialty 01.04.05 (Optics) can be properly established.

REFERENCES

1. Fang, Q., Xia, H., Song, Q., Zhang, M., Guo, R., Montresor, S., & Picart, P. (2022). Speckle denoising based on deep learning via a conditional generative adversarial network in digital holographic interferometry. *Optics Express, 30*(12), 20666–20683. https://doi.org/10.1364/OE.459213
2. Feng, S., Chen, Q., Gu, G., Tao, T., Zhang, L., Hu, Y., Yin, W., & Zuo, C. (2019). Fringe pattern analysis using deep learning. *Advanced Photonics, 1*(2), 025001. https://doi.org/10.1117/1.AP.1.2.025001
3. Ghiglia, D. C., & Pritt, M. D. (1998). *Two-dimensional phase unwrapping: Theory, algorithms, and software*. Wiley.
4. Goodman, J. W. (2020). *Speckle phenomena in optics: Theory and applications* (2nd ed.). SPIE Press.
5. Kreis, T. (2005). *Handbook of holographic interferometry: Optical and digital methods*. Wiley-VCH. https://doi.org/10.1002/3527604154
6. Montresor, S., Tahon, M., Laurent, A., & Picart, P. (2020). Computational de-noising based on deep learning for phase data in digital holographic interferometry. *APL Photonics, 5*(3), 030802. https://doi.org/10.1063/1.5140645
7. Narayan, S. K., & Gannavarpu, R. (2025). Simultaneous estimation of multiple order phase derivatives using deep learning method in digital holographic interferometry. *Optics and Lasers in Engineering, 184*, 108583. https://doi.org/10.1016/j.optlaseng.2024.108583
8. Pedrini, G., Osten, W., & Gusev, M. E. (2006). High-speed digital holographic interferometry for vibration measurement. *Applied Optics, 45*(15), 3456–3462. https://doi.org/10.1364/AO.45.003456
9. Rastogi, P. K. (Ed.). (2001). *Digital speckle pattern interferometry and related techniques*. Wiley.
10. Schnars, U., & Jüptner, W. P. O. (2002). Digital recording and numerical reconstruction of holograms. *Measurement Science and Technology, 13*(9), R85–R101. https://doi.org/10.1088/0957-0233/13/9/201
11. Störk, T., Seyler, T., Fratz, M., Bertz, A., Hensel, S., & Carl, D. (2024). Detecting vibrations in digital holographic multiwavelength measurements using deep learning. *Applied Optics, 63*(7), B32–B41. https://doi.org/10.1364/AO.507303
12. Vithin, A. V. S., Vishnoi, A., & Gannavarpu, R. (2022). Phase derivative estimation in digital holographic interferometry using a deep learning approach. *Applied Optics, 61*(11), 3061–3069. https://doi.org/10.1364/AO.455775
13. Wang, K., Qian, K., Di, J., & Zhao, J. (2022). Deep learning spatial phase unwrapping: A comparative review. *Advanced Photonics Nexus, 1*(1), 014001. https://doi.org/10.1117/1.APN.1.1.014001
14. Yamaguchi, I., & Zhang, T. (1997). Phase-shifting digital holography. *Optics Letters, 22*(16), 1268–1270. https://doi.org/10.1364/OL.22.001268

CONTENTS

Begmatov Shavkat
INTEGRATION OF RENEWABLE ENERGY SOURCES INTO AGRICULTURE IN UZBEKISTAN 4

Urazxanova Elvira
MULTI-CRITERIA MODEL FOR THE FORMATION OF AN URBAN BUS ROUTE NETWORK UNDER UNCERTAINTY 12

Jumabaev Dauletbay, Urazxanova Elvira
URBAN BUS ROUTE OPTIMIZATION USING DYNAMIC PROGRAMMING AND PARETO-EFFICIENT SELECTION 17

Bakiev Masharif, Kuryozov Otaboy, Yakubov Kuvonchbek, Khasanov Khojiakbar, Khalimbetov Azat, Ganjayev Mukhammad
HYDRAULIC CALCULATION PROCEDURE FOR FLOW EXPANSION CONSTRICTED BY A SPUR DIKE..... 24

Ganesh Gupta, Ahmed Yusupov
GAIN-SATURATED SEMICONDUCTOR OPTICAL AMPLIFIERS FOR FREE-SPACE OPTICAL COMMUNICATION: PERFORMANCE LIMITATIONS AND NUMERICAL ANALYSIS OF SCINTILLATION MITIGATION..... 35

Eshqobilov Jamshid, Abdukarimov Mirzokhid
THERMAL STABILITY AND DECOMPOSITION STAGES OF A CORROSION-RESISTANT EPOXY-COAL TAR COMPOSITE COATING: TGA/DTA STUDY 46

Kattaeva Gulnoza, Ismonov Abduvahob, Mamajanova UktamxonDusaliev Alijon
THE EFFECT OF FUJIMIN LIQUID FERTILIZER ON INCREASING SOIL FERTILITY UNDER EXTREME CLIMATIC CONDITIONS 52

Qilichev Xudoynazar, Qurbonov Jaloliddin, Farmonov Shavkat, Allaberganova Gulchehra, Yorqulov Behzod, Muzafarov Amrullo
ASSESSMENT OF RADIONUCLIDE PARAMETERS IN SOILS OF RECLAIMED AREAS BASED ON A MATHEMATICAL MODEL 57

Akbarova Nigora, Toshpulatova Dilorom
ASSESSMENT OF RADIONUCLIDE PARAMETERS IN SOILS OF RECLAIMED AREAS BASED ON A MATHEMATICAL MODEL 64

Tursunov Rovshan, Buvaraimov Ziyodullo, Nurqulov Fayzulla
STUDY OF THE MECHANICAL STABILITY AND FIRE RESISTANCE OF FLAME-RETARDANT-MODIFIED POLYESTER–MINERAL COMPOSITES... 71

Mahmudov Mahmud, Rixsiboyev Ravshan
FEDERATED TINYML FOR DISTRIBUTED IOT SYSTEMS: A PRIVACY-PRESERVING AND ENERGY-EFFICIENT EDGE INTELLIGENCE FRAMEWORK 81

Kazakov Tolibjon
INVESTIGATION OF THE SOURCES OF MEASUREMENT UNCERTAINTY IN THE CALIBRATION OF MEASURING INSTRUMENTS 86

Akbarova Nigora, Toshpulatova Dilorom
INVESTIGATION OF THE SOURCES OF MEASUREMENT UNCERTAINTY IN THE CALIBRATION OF MEASURING INSTRUMENTS 91

ISSN: 2181-3337 | SCIENTISTS.UZ



International Scientific Journal
Science and Innovation Series A
Volume 5 Issue 9

ISSN: 2181-3337

Published: 31.09.2026. Font: “Times New Roman”.

LLC “Science and innovation”
License Mass Media №:1597 27.04.2022
License Publisher №:455168 21.11.2024
Address: 100121, Uzbekistan, Tashkent city, Yakkasaroy district,
Shota Rustaveli Street 150, Vega Business Center, 6th floor, Room 2.
www.scientists.uz, info@scientists.uz, +998901259654

ISSN: 2181-3337